

Search for neutral Higgs boson in $\tau\tau \rightarrow \mu + \tau_{jet}$ final state in the CMS experiment

Tomasz Früboes
National Centre for Nuclear Research

A thesis submitted in partial fulfillment of requirements for the degree of
Doctor of Philosophy in Physics written under the supervision of
prof. H. Białkowska and dr M. Konecki

Warsaw, February 2013

Acknowledgements

I would like to thank to my PhD advisors, prof. Helena Białkowska and dr Marcin Konecki, for help and guidance they provided during my studies in last years.

I will forever be thankful to my colleagues, dr Artur Kalinowski and dr Michał Bluj. Without their helpful, kind and often motivating words this thesis would never have been completed. I also thank dr Piotr Zalewski for very useful discussions. I also thank all present and former members of CMS Warsaw Group for creating a stimulating work environment.

This study was supported by polish National Science Centre, decision DEC-2011 / 01 / N / ST2 / 00407. I would like to thank for provided support. This research was supported in part by PL-Grid Infrastructure.

During all of the years I have spent studying physics my family was extremely supportive. Without your help I wouldn't be able to finish this long journey.

Agacie

Abstract

This thesis is devoted to search for the Standard Model Higgs Particle in $\tau\tau \rightarrow \mu + \tau_{jet}$ final state in the CMS experiment. Drell-Yan (DY) $\tau\tau$ process is the main irreducible background for this search. A new data driven method for estimation of this background is presented. It is called the embedding method. The method involves embedding of simulated τ decays in DY $\mu\mu$ events recorded by the CMS experiment.

A procedure using the embedding method to obtain a proper shape and normalization of the DY $\tau\tau$ background in searches with two τ leptons in the final state is described. Detailed studies on the embedding method systematic uncertainties are presented. The embedding method is used in the search of the Higgs particle in $\tau\tau \rightarrow \mu + \tau_{jet}$ final state with 5 fb^{-1} of data at $\sqrt{s} = 7 \text{ TeV}$.

In this thesis two additional studies are presented - one on determination of hadronic τ tag efficiency using $Z \rightarrow \tau\tau \rightarrow \mu\tau_{had}$ to $Z \rightarrow \mu\mu$ events ratio and one on possibility of using measurements done with a GEM (Gas Electron Multipliers) detectors in the Level-1 RPC (Resistive Plate Chamber) Trigger.

Streszczenie

Praca ta poświęcona jest poszukiwaniu bozonu Higgsa w Modelu Standardowym w kanale $\tau\tau \rightarrow \mu + \tau_{jet}$. Proces Drella-Yana (DY) w $\tau\tau$ jest głównym i nieredukowalnym procesem tła dla tej analizy. Zaprezentowana została nowa metoda szacowania tego tła, tzw. metoda osadzania. W metodzie tej wykorzystywane są zarejestrowane przez eksperyment CMS zdarzenia DY $\mu\mu$, w których miony zastępowane są symulowanymi rozpadami leptonów τ .

W pracy tej opisana została procedura szacowania tła DY $\tau\tau$ przy użyciu metody osadzania wraz z dokładną analizą niepewności systemycznych metody. Procedura ta została zastosowana w poszukiwaniu bozonu Higgsa w Modelu Standardowym w kanale $\tau\tau \rightarrow \mu + \tau_{jet}$ przeprowadzonym dla 5 fb^{-1} danych zebranych przy energii $\sqrt{s} = 7 \text{ TeV}$.

W pracy załączono dodatkowo analizę nad efektywnością oznaczania hadronowych rozpadów τ przy wykorzystaniu stosunku liczby zdarzeń DY $\tau\tau \rightarrow \mu\tau_{had}$ do DY $\mu\mu$ oraz analizę nad możliwością wykorzystania sygnałów z komór typu GEM (Gas Electron Multipliers) w trygerze pierwszego stopnia w oparciu o komory RPC (Resistive Plate Chamber).

Contents

Introduction	3
Author's contribution to the Compact Muon Solenoid experiment	6
1. Higgs particle in the Standard Model	7
1.1. Standard Model - an overview	7
1.2. Higgs boson production and decay in the Standard Model	9
1.3. Background processes in the $H \rightarrow \tau\tau \rightarrow \mu + \tau_{\text{jet}}$ search	12
2. Compact Muon Solenoid Experiment at Large Hadron Collider	15
2.1. Superconducting magnet	17
2.2. Tracking detectors	17
2.3. Electromagnetic calorimeter	19
2.4. Hadron calorimeter	19
2.5. Muon detectors	20
2.5.1. Cathode Strip Chambers	20
2.5.2. Drift Tubes	20
2.5.3. Resistive Plate Chambers	21
2.6. Trigger and data acquisition	22
2.7. Event reconstruction	25
2.7.1. Track reconstruction	25
2.7.2. Muon reconstruction	25
2.7.3. Electron and photon reconstruction	26
2.7.4. Particle Flow	28
2.7.5. Missing transverse energy	29
2.7.6. Jets	31
2.7.7. Hadronic τ decays identification	32
3. Determination of Drell-Yan $\tau\tau$ background using embedding of simulated τ decays in Drell-Yan $\mu\mu$ events	35
3.1. Possible approaches to τ embedding	36

3.2. Particle Flow embedding procedure	37
3.2.1. DY $\mu\mu$ event selection	37
3.2.2. Creation and simulation of $\tau\tau$ event	40
3.2.3. Cleaning and mixing	41
3.2.4. Method discussion	41
3.2.5. Systematic uncertainties of the embedding method	42
3.2.6. Method validation	45
4. $H \rightarrow \tau\tau \rightarrow \mu\tau_{had}$ search in the CMS experiment	53
4.1. Event selection	54
4.1.1. Online selection	54
4.1.2. Offline selection	54
4.2. Event yield estimation	57
4.2.1. Summary of DATA to MC corrections	57
4.2.2. Estimation of DY $\tau\tau$ background	57
4.2.3. Estimation of the QCD background	60
4.2.4. Estimation of the W+Jets background	61
4.2.5. Estimation of other background sources	61
4.2.6. Signal estimation	61
4.3. Results	62
Summary	71
A. The Standard Model of particle physics	73
A.1. Quantum electrodynamics as an example of gauge theory	73
A.1.1. Gauge theories with massive interaction carriers	74
A.2. The Standard Model of electroweak interactions	76
B. Estimation of hadronic τ tag efficiency using $Z \rightarrow \tau\tau \rightarrow \mu\tau_{had}$ to $Z \rightarrow \mu\mu$ events ratio	83
C. RPC trigger of the CMS experiment	87
C.1. RPC trigger - principle of operation	87
C.2. RPC trigger segmentation	89
C.3. PAC algorithms	93
C.3.1. Baseline algorithm	93
C.3.2. Economic algorithm	93
C.4. Ghostbusting	95

C.5. Muon triggering with GEM detectors in the high- η region	98
C.5.1. Trigger emulation	98
C.5.2. GEM geometry	99
C.5.3. Simulated chamber properties	100
C.5.4. Results	101
Bibliography	111

Introduction

The Standard Model of particle physics is a theory describing precisely three out of four known elementary interactions - electromagnetic, weak and strong [1]. Tests of the Standard Model during last 30 years show no deviations from its predictions.

Despite its perfect agreement with experimental data, the Standard Model leaves number of questions open:

Interactions unification - in 1979 Salam [2], Glashow [3] and Weinberg [4] found a method to describe electromagnetic and weak interactions as a manifestation of a single interaction, called electroweak interaction.

Strong interactions in the Standard Model are described by quantum chromodynamics, which is not related to electroweak interaction. It is still a subject of theoretical studies whether a theory consistent with Nature unifying electroweak and strong interactions can be developed.

Electroweak symmetry breaking mechanism - in electroweak theory so called Higgs mechanism is used in order to give weak interaction carriers their mass, while keeping the photon massless [5]. The Higgs mechanism, while currently most likely, remains yet not fully proven.

Neutrino masses - in 1998 the Super-Kamiokande collaboration announced first experimental evidence of non-zero neutrino mass [6]. Prior to this date neutrinos were assumed massless in the Standard Model. Only limits on neutrino masses are currently known, indicating the heaviest neutrino mass being at least six orders of magnitude smaller than the electron mass. It is unclear what mechanism leads to such big difference in mass scales.

Matter over antimatter dominance - astronomical observations show, that the Universe is made mainly from matter; antimatter exists in trace amounts. Mechanisms present in the Standard Model are not strong enough to account for observed matter to antimatter ratio.

Matter energy balance - several astronomical observations indicate, that observable matter constitutes only 4.6% [7] of matter and energy in the Universe, while rest consists of hypothetical Dark Matter (matter of which interactions are very weak, therefore hard to detect directly) and Dark Energy. There are no candidate particles present in the Standard Model that could form Dark Matter.

The examples given above lead to a common conviction among physicists, that the Standard Model is not a final theory and new phenomena should occur for interaction energies higher than tested up to now. This conviction is one of the main reasons for building the Large Hadron Collider.

The Large Hadron Collider (LHC) is a circular collider built in the CERN laboratory (European Organization for Nuclear Research) near Geneva in Switzerland. Collider is placed in the 27-kilometer long underground tunnel originally built for and used by LEP (Large Electron Positron Collider).

During 2010 and 2011 the LHC was running mostly in proton-proton mode¹, colliding two opposite beams with an energy of 3.5 TeV each² every 50 ns³. Achieving such high energy and the frequency of collisions is a huge challenge, both technical and financial. To cope with this challenge, in construction and operation of the LHC (and its accompanying experiments) approximately 10000 people from 111 nations took part.

The main task of the LHC is to broaden the knowledge on the structure of matter. This is possible thanks to high frequency and high energy of collisions along with high beams intensity, since new phenomena are expected to occur rarely and to require a large energy exchange.

LHC research areas include:

Search for Higgs boson - before the LHC era, LEP data analyses have shown, that mass of Higgs boson in the Standard Model is greater than $114.4 \text{ GeV}/c^2$ at 95% confidence level [8]. Fits to precision electroweak measurements (not including direct LEP limit) [9] indicate that Higgs boson should be a relatively light particle with most probable mass of $89_{-26}^{+35} \text{ GeV}/c^2$.

¹The LHC also allows collision of lead ions. Such collisions were performed for short periods at the end of 2010, the end of 2011 and in 2013.

²Original LHC design assumed 7 TeV per beam energy. Due to problems with superconducting magnets this value was temporarily lowered for safety purposes. The LHC was running with 3.5 TeV per beam energy in 2011 and 4 TeV per beam energy in 2012. Both values refer to proton-proton runs.

³LHC construction allows collisions every 25 ns, collisions in this mode were performed only for test purposes.

Search for supersymmetric particles - in supersymmetric theories all of currently known elementary particles are accompanied by so called superpartners - new particles with spin differing by value $\frac{1}{2}$.

One of the ways of finding supersymmetry is search for presence of so called Lightest Supersymmetric Particle (LSP). In some supersymmetric models this particle is stable and very weakly interacting with matter. Its production may be indicated by excess of events with missing transverse energy (taken out from detector by LSP particle).

Precision tests of Standard Model - high collision energy along with high luminosity provided by the LHC will allow comprehensive verification of the Standard Model. This supplements direct searches of new physics (e.g. searches for new elementary particles), since even small deviations from the Standard Model predictions may point new research directions. Most important areas include tests of quantum chromodynamics, heavy flavor physics, electroweak interactions and top quark physics.

Searches for “exotic” physics - LHC program includes direct searches for a new physics phenomena such as new vector bosons, extra dimensions or new fermions. One of the large number of such searches performed by the LHC experiments is a search for gravitons predicted by Randall-Sundrum model [10]. Gravitons are expected to decay to two photons, therefore search is performed by looking for an excess at high invariant mass in observed di-photon mass spectrum.

High luminosity leads to certain challenges and requirements for experiments measuring products of LHC collisions. One of the consequences is a necessity to cope with pile-up, a presence of overlaid several different proton-proton collisions during a single bunch crossing. During 2011 on average 9 interactions occurred in every bunch crossing.⁴ Even more important requirement for LHC experiments is the ability to select most interesting events online, using dedicated algorithms executed in a time of event processing.

Products of collisions in LHC are measured by six experiments - two general purpose experiments designed to study both particle physics and heavy ion physics - ATLAS (A Toroidal LHC Apparatus) and CMS (Compact Muon Solenoid) experiment; ALICE (A Large Ion Collider Experiment), dedicated to heavy ion physics; LHCb experiment (Large Hadron Collider beauty), dealing with the physics of quark b and two small experiments - LHCf (Large Hadron Collider forward), studying cascades from high energy particles in order to better understand high energetic components of cosmic rays and TOTEM (Total Cross Section, elastic scattering and diffraction dissociation at the LHC), which focuses

⁴For a beam of protons, as recorded by a CMS experiment.

on the study of diffractive processes and measuring the elastic scattering cross sections of elementary interactions.

This work is structured in a following way - a short introduction to the Standard Model, including description of the Higgs mechanism, is presented in Chapter 1; description of the CMS experiment, its detector, trigger and reconstruction algorithms is described in Chapter 2; τ embedding method is explained in Chapter 3; search of Higgs boson decaying to τ pairs (in μ +jet final state) is presented in Chapter 4. Appendix A contains a more detailed introduction to the Standard Model. In Appendix B determination of hadronic τ identification efficiency using DY $\tau\tau \rightarrow \mu\tau_{\text{had}}$ to DY $\mu\mu$ events ratio is presented. Appendix C contains detailed description of RPC trigger, including study of possible RPC trigger upgrade using Gas Electron Multiplier type detectors.

Author's contribution to the Compact Muon Solenoid experiment

The author of this thesis is a member of the CMS collaboration. He took active part in Resistive Plate Chamber (RPC) trigger construction and commissioning. He has participated in data taking runs (both cosmic and LHC) during which he was responsible for proper operation of RPC trigger and for the data analysis. Author was also responsible for the RPC trigger related offline software (including the RPC trigger emulator and the RPC trigger monitoring package in the CMS reconstruction software), RPC trigger patterns lists development and RPC trigger firmware building. His contribution also includes study of possible RPC trigger upgrade using Gas Electron Multiplier detectors.

Author has developed a method involving embedding of simulated τ decays in DY $\mu\mu$ events. It is included in standard CMS analyses. This method is used in the CMS Higgs searches for data driven estimation of DY $\tau\tau$ background. Author has performed detailed studies on the embedding method systematic uncertainties and proposed a new procedure to obtain a proper normalization of the DY $\tau\tau$ background in searches with two τ leptons in the final state. Author's contribution to Higgs searches includes also a study of hadronic τ identification efficiency using DY $\tau\tau \rightarrow \mu\tau_{\text{had}}$ to DY $\mu\mu$ events ratio.

Chapter 1.

Higgs particle in the Standard Model

1.1. Standard Model - an overview

The Standard Model (SM) is a theory describing electromagnetic, weak and strong interactions of elementary particles. Quantum Field Theory is a framework in which the Standard Model is built. After identification of the fermionic particles content of the SM (consisting of 6 types of quarks and 6 types of leptons) an underlying symmetry group is chosen, describing interactions present in the SM:

$$U_Y(1) \times SU_L(2) \times SU_C(3)$$

$SU_C(3)$ group is related to the strong (color) interactions, while the remaining part is responsible for the electroweak interactions.

Interaction properties are derived by requirement of the Lagrangian describing dynamics of the free (noninteracting) fermions to be invariant under the local (position dependent) transformations:

$$\Psi \rightarrow e^{-i\omega(x)}\Psi$$

(Ψ is a fermion field). In order to meet this requirement extra fields coupled to fermions are introduced (so called gauge or interaction fields).

Gauge fields are required to be massless. Introduction of a mass term in the Lagrangian density of a gauge field (in a form of $M_A^2 A_\mu A^\mu$) breaks a gauge invariance due to appearance of

$$\frac{2M_A^2}{e} A^\mu \partial_\mu \omega$$

term after the gauge transformation.

Weak interactions occur only for left handed fermions. Mass term for a fermion field:

$$m\bar{\Psi}\Psi = m(\bar{\Psi}_L\Psi_R + \bar{\Psi}_R\Psi_L)$$

"mixes" left (L) and right (R) handed states. Such terms are forbidden in the Lagrangian density, since they break the gauge invariance - $SU_L(2)$ gauge transformation acts only on left handed component. Therefore at this point fermions are also required to be massless.

In order to grant masses to the fundamental fermions and selected interaction carriers (which correspond to the gauge fields) an extra field Φ (so called Higgs field) is introduced to the Lagrangian:

$$\mathcal{L}_{Higgs} = (D_\mu\Phi)^\dagger(D^\mu\Phi) - V(\Phi)$$

$$V(\Phi) = -\mu^2\Phi^\dagger\Phi + \lambda(\Phi^\dagger\Phi)^2$$

The \mathcal{L}_{Higgs} term contains a coupling between the Higgs field and massless gauge fields W^μ and B^μ corresponding to $U_Y(1) \times SU_L(2)$ symmetry group, since:

$$D_\mu = \partial_\mu - ig_2\frac{\sigma_a}{2}W_\mu^a + i\frac{g_1}{2}B_\mu$$

Higgs field can be written around the ground state v ($v = \frac{\mu}{\sqrt{\lambda}}$) of the potential $V(\Phi)$

$$\Phi = \frac{1}{\sqrt{2}} \begin{pmatrix} 0 \\ v + H \end{pmatrix}$$

leading to

$$V(\Psi) = \mu^2H^2 + \lambda vH^3 + \frac{\lambda}{4}H^4$$

From the above equation mass of the Higgs boson (related to field H) can be read:

$$M_H = \mu\sqrt{2}$$

Use of the same expression for expanded Higgs field inside the kinetic term $(D_\mu\Phi)^\dagger(D^\mu\Phi)$ allows one to identify quadratic terms in fields W^μ and B^μ . These are interpreted as mass terms for those fields. Fields W^μ and B^μ can then be rewritten using physical fields corresponding to photons, W and Z bosons. Masses of the W and Z bosons are proportional to their coupling strength to the Higgs field

$$M_W = \frac{1}{2}g_2v, \quad M_Z = \frac{1}{2}\sqrt{g_1^2 + g_2^2}v$$

while photon is found to be massless.

Choice of a specific ground state v of the theory breaks the underlying Lagrangian symmetry $U_Y(1) \times SU_L(2) \times SU_C(3)$ to $U_Q(1) \times SU_C(3)$ symmetry (mass terms appear for weak interaction bosons). This is usually called Spontaneous Symmetry Breaking.

As it was shown above, Lagrangian density cannot include mass terms for fermion fields, since they break the gauge invariance. To give fermion masses the Higgs field is once again used. Fermion fields are coupled to the Higgs field via Yukawa type interaction.

Appendix A contains a more detailed introduction to the Standard Model of Particle Physics.

1.2. Higgs boson production and decay in the Standard Model

After expanding the \mathcal{L}_{Higgs} lagrangian part, the following terms can be found:

$$\begin{aligned}\mathcal{L}_{H_{self}} &= -\frac{M_H^2}{2v} H^3 - \frac{M_H^2}{8v^2} H^4 \\ \mathcal{L}_{H_V} &= M_W^2 W_\mu^\dagger W^\mu \left(\frac{2H}{v} + \frac{H^2}{v^2}\right) + \frac{1}{2} M_Z^2 Z_\mu Z^\mu \left(\frac{2H}{v} + \frac{H^2}{v^2}\right) \\ \mathcal{L}_{H_f} &= \frac{H}{v} \sum_f m_f \bar{f} f\end{aligned}$$

(in last term summation occurs for all fermions). Above terms describe Higgs boson interactions with SM particles. It is worth noting, that the interaction strength is proportional to the mass of the particle involved in given interaction.

Higgs boson does not couple directly to gluons or to photons - these particles are massless. Such couplings are possible via a fermion or W boson loop (in case of photon coupling; Figures 1.1a, 1.1b) or by a quark loop (in case of gluon coupling; Figure 1.1c). Since the coupling is not direct its strength is small when compared to the (direct) fermion or boson one.

Decay of the Higgs boson depends on the coupling strengths described above as well as on its mass (which determines the phase space available for the decay). The Higgs boson branching ratios [11] as a function of its mass are shown in Figure 1.2. For masses up to

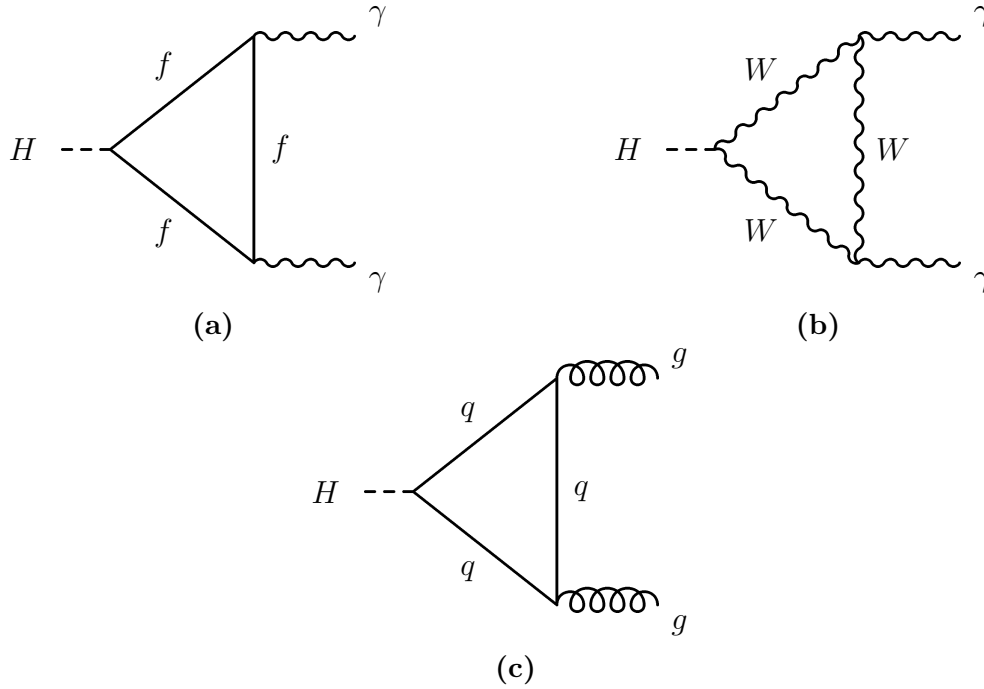


Figure 1.1.: Coupling of the SM Higgs boson to a photon pair via fermion loop (a), to a photon pair via W boson loop (b) and to a gluon pair via quark loop (c).

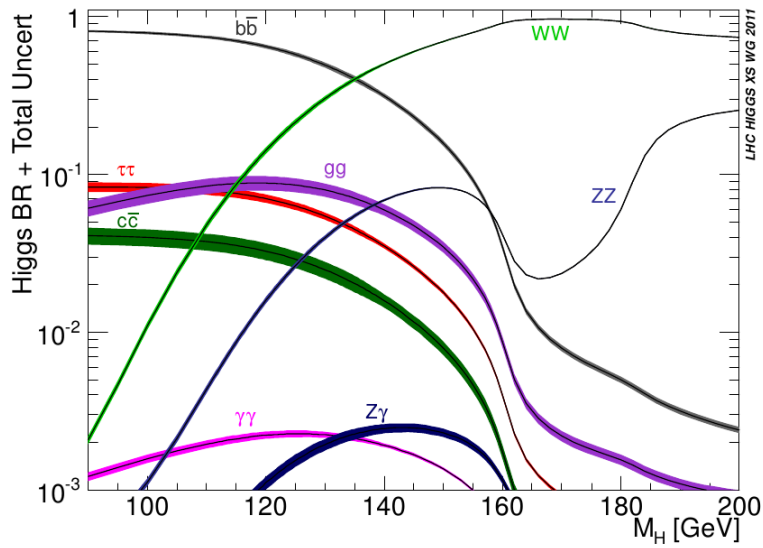


Figure 1.2.: Standard Model Higgs boson decay modes

135 GeV/ c^2 dominant mode is decay to $b\bar{b}$ quark pair (since the b quark is the heaviest particle to which decay is allowed due to the Higgs mass).

Since $b\bar{b}$ decay mode requires two jets in the final state, a search in this channel is difficult (due to large QCD background, which is hard to suppress). Therefore in a low mass range a final state with two τ leptons is a promising search channel. It has relatively

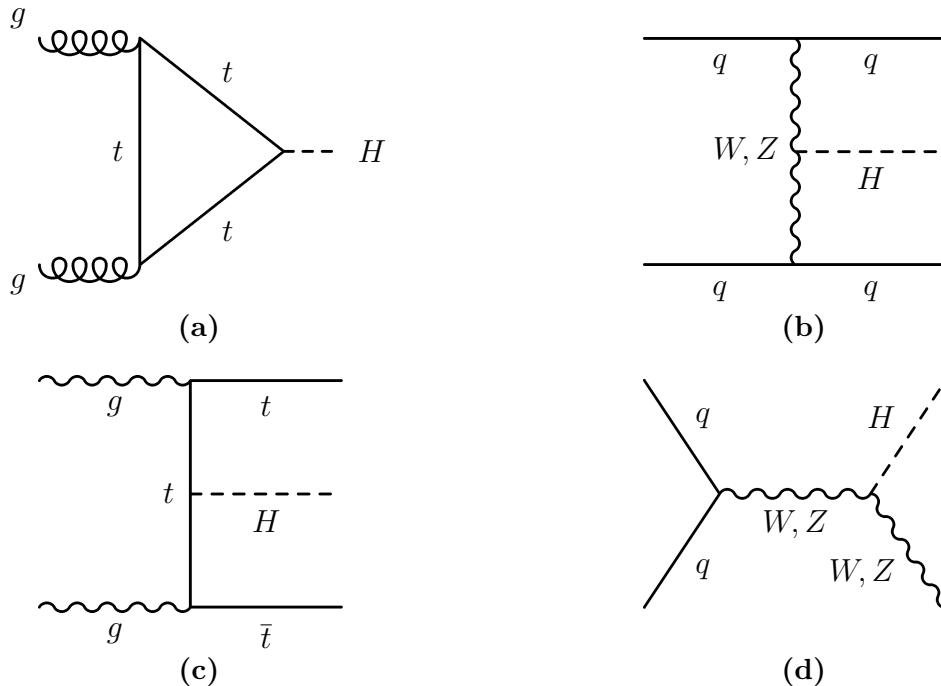


Figure 1.3.: Main processes of Higgs production at the LHC - Gluon Fusion (a), Vector Boson Fusion (b), Associated Production with Heavy Quarks (c), Associated Production with Vector Boson (d).

high branching ratio and background can be suppressed by exploiting final state properties (by requiring presence of lepton coming from τ decay and/or using τ decay properties to tag its hadronic final state).

For all Higgs boson masses from the range unconstrained by LEP (higher than $114.4 \text{ GeV}/c^2$) Higgs boson decay to a WW boson pair followed by a subsequent decay to leptons (muons or electrons) and neutrinos form a sensitive channel to search. The less frequent decays occur to a ZZ boson pair. Despite lower branching ratio Higgs boson searches in ZZ channel with 4 leptons in the final state are of primary importance due to very distinct signature and excellent mass resolution.

For low Higgs boson masses (up to $145 \text{ GeV}/c^2$) another promising final state is the one with two photons. Despite very low branching ratio ($O(10^{-3})$) this mode can lead to a Higgs boson discovery thanks to excellent mass reconstruction resolution.

Main processes leading to the Higgs boson production in LHC are shown in Figure 1.3. The dominant process is the Gluon Fusion, although Higgs to gluons coupling is not direct. Second most dominant process is Vector Boson Fusion (VBF). Its cross section is suppressed due to the low strength of weak interactions (when compared to Gluon Fusion). Nevertheless this production mode provides very clean environment for the search (Higgs

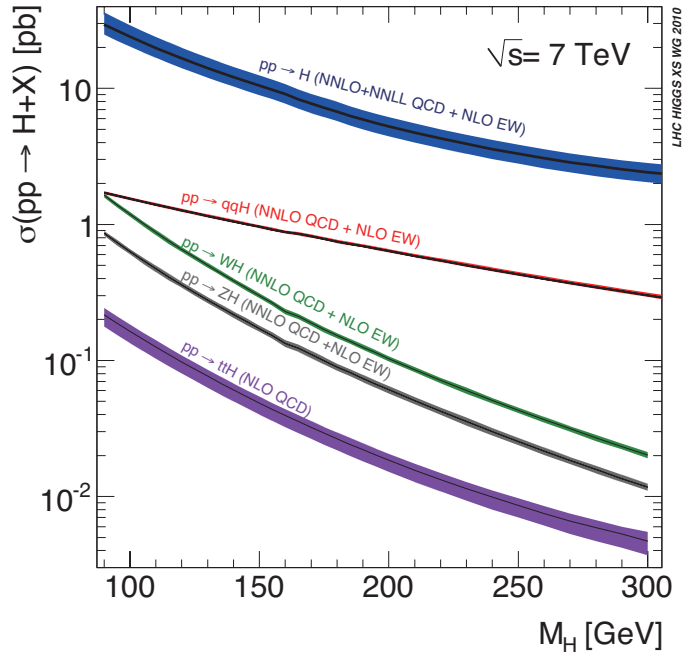


Figure 1.4.: Standard Model Higgs boson production cross sections for $\sqrt{s} = 7$ TeV.

decay products present along with two forward jets; very low activity in between the two jets) when compared to the Gluon Fusion.

Remaining processes include Associated Production with Vector Boson and Associated Production with Heavy Quarks.

The Standard Model Higgs boson production cross sections for $\sqrt{s} = 7$ TeV for all considered processes [12] are shown in Figure 1.4.

1.3. Background processes in the $H \rightarrow \tau\tau \rightarrow \mu + \tau_{\text{jet}}$ search

In the analysis presented in this dissertation data are selected by requiring a muon and reconstructed hadronic tau decay (τ_{had}) signature. Both muon and τ_{had} are required to have high transverse momenta. Apart of the Higgs boson decay there are other processes in the Standard Model leading to a presence of a muon and reconstructed hadronic τ decay.

The Drell-Yan (DY) process involves annihilation of two quarks into a Z boson (or a virtual photon) decaying to a pair of oppositely charged leptons of the same type. Creation

of a $\tau\tau$ pair via a DY process is the main irreducible background process in presented analysis. The $\tau\tau$ pair production in the DY process involves a decay of a Z boson (or a virtual photon) produced by annihilation of two quarks. Tau pairs produced in the DY process are difficult to distinguish from the ones produced from Higgs boson. Those two production modes are expected to differ in invariant mass of the muon- τ_{had} pair.

Second biggest source of background is a W boson production along with one or more jets. In such events a W boson decay leads to a muon production while one of the jets present in the event can be misidentified as hadronic tau decay. Such events are characterized by a high missing energy due to neutrino presence in the W boson decay. This background can be discriminated by exploiting the topology of the muon momentum and missing energy direction.

Production of top quark pairs is another important background process in this analysis. A top quark predominantly decays to a b quark and a W boson.

Another process contributing to the background is QCD multijet production along with the muon. In a similar way as for W boson background in QCD events one of the jets can be misidentified as the hadronic τ decay. Such events can be discriminated by requiring no detector activity around reconstructed muon and hadronic τ decay.

Remaining background processes include production of single top quark, DY $\mu\mu$ production (in such events one of the muons or an extra jet may be misidentified as hadronic τ) and production of the diboson pairs (WW , WZ or ZZ).

Chapter 2.

Compact Muon Solenoid Experiment at Large Hadron Collider

The CMS experiment is a general purpose experiment. It is suitable to study a wide range of physical phenomena, that could occur at LHC energies. CMS physics program includes:

- Higgs boson searches
- Precise measurements of the Standard Model parameters
- Searches for beyond Standard Model phenomena, such as extra dimensions, supersymmetry, new interaction bosons
- Studies of heavy ion collisions, e.g. searches of quark-gluon plasma

In order to take full advantage of LHC power, CMS detector was designed and built with following goals defined [13]:

1. A robust and redundant muon system
2. The best possible electromagnetic calorimeter
3. A high quality central tracking supporting 1) and 2)
4. Detector has to be financially affordable

Additionally the detector takes advantage of hadronic calorimeter with wide η coverage.

A schematic view of the CMS experiment is shown on Figure 2.1. The detector consists of a central region called barrel and two endcaps at both ends of barrel.

CMS detector uses three types of muon detectors - Drift Tubes (DT) in barrel region, Cathode Strip Chambers (CSC) in endcaps region and Resistive Plate Chambers

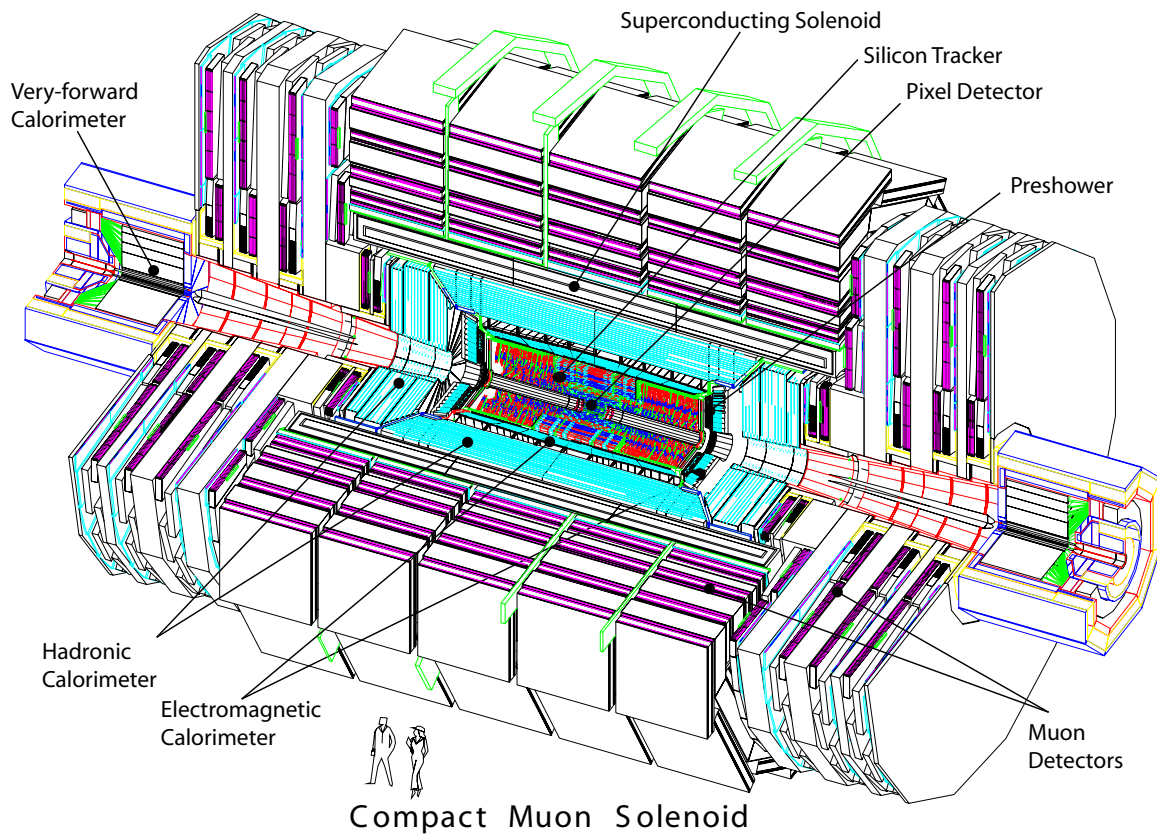


Figure 2.1.: The CMS detector

(RPC) both in barrel and endcaps region. Muon chambers are placed outside of the superconducting solenoid.

Inside of the solenoid a hadronic calorimeter (HCAL) is placed consisting of brass and steel sandwiched with a plastic scintillator. Closer to the beam electromagnetic calorimeter (ECAL) is located, built of dense PbWO_4 crystals in order to detect and precisely measure photons and electrons.

Closest to the beam a silicon tracker is placed. Measurements are done using strip tracker in region farther to the beam and pixel tracker in volume closest to the beam.

Detailed description of all subsystems of CMS experiment can be found in following sections.

Field inside coil	3.8 T
Length	12.9 m
Inner diameter	5.9 m
Electric current	19.5 kA

Table 2.1.: Parameters of magnet of the CMS experiment

2.1. Superconducting magnet

One of the most important elements of CMS detector is its superconducting magnet. Bending power of magnetic field allows to measure transverse momenta of charged particles. Proper selection of magnet characteristic has a huge impact on achievable transverse momentum resolution.

The CMS experiment uses solenoid superconducting magnet, its parameters are shown in Table 2.1. In the second half of year 2006 the CMS magnet was switched on and tested successfully, design goal of 4 T was reached during tests [14]. During normal operation magnet functions with field of 3.8 T.

Choice of solenoid magnet was justified by two main factors:

- Bending of charged particles tracks is done in the plane transverse to the beam axis. At the same time small size of the beamspot (volume, where p-p interactions occur) determines the position of primary interaction vertex (in transverse plane) with accuracy of about $50 \mu\text{m}$ [15]. This feature facilitates tasks of trigger subsystems performing measurements of transverse momenta of produced particles (e.g. muons).
- Use of superconducting solenoid with return yoke allows compact design of the detector.¹

2.2. Tracking detectors

Tracking detectors used in the CMS experiment surround the interaction point. Measurements done by tracker are used to determine exact position of vertices and to measure

¹ATLAS experiment uses two types of magnets - small solenoid one with 2 T field, and a larger toroidal one with field of about 4 T. Use of toroidal magnet results with bigger size of ATLAS detector (diameter of 25 m, 46 m of length) when compared to CMS detector (16 m and 21 m respectively)

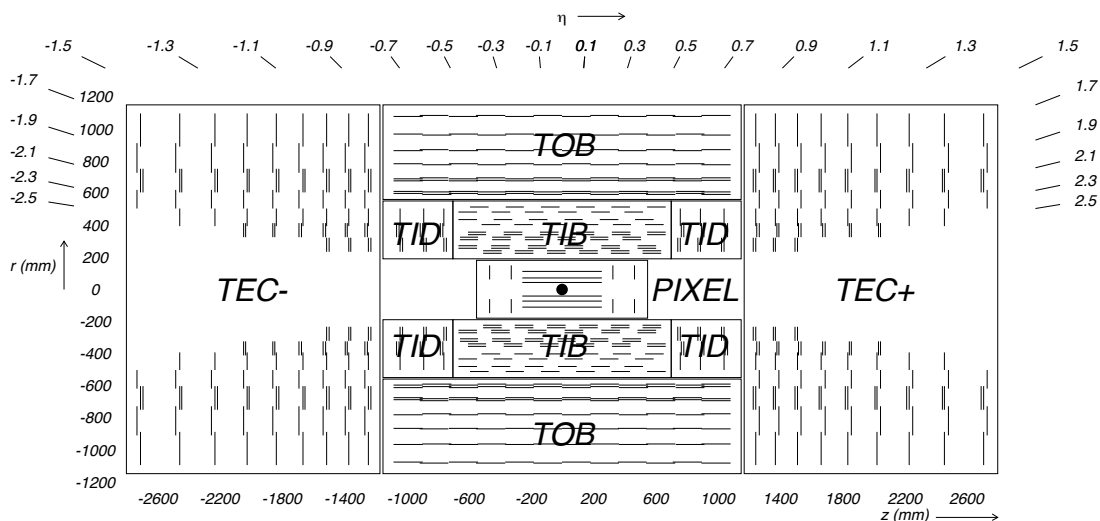


Figure 2.2.: Transverse view of CMS tracking detectors.

trajectories (tracks) of charged particles produced in collisions. Reconstructed tracks allow precise determination of particle momenta and their charge.

In Figure 2.2 a transverse view of the CMS tracking detectors is shown. Two types of tracking detectors are used - silicon pixel and silicon strip based[16]. Usage of given type of detector is dictated by intensity (flux) of passing particles (decreasing with distance from beam):

- In region closest to the beam (from 4 to 15 cm in radius) pixel detector is placed, consisting of three cylindrical layers, supplemented with two disks at both sides of interaction point. The CMS pixel detector has about 66 million readout channels and provides coverage in region $|\eta| < 2.5$
- In further region from the beam (from 25 to 116 cm in radius) a silicon strip detector is placed, consisting of three main subsystems. Central, closest to the beam part (Tracker Inner Barrel and Disks; TIB/TID) is composed of four barrel layers accompanied by three disks at both sides of interaction point. TIB/TID is contained in Tracker Outer Barrel (TOB), which spans to 116 cm in radius. TOB is composed of 6 layers. The last subsystem (Tracker EndCaps; TEC) is placed at both sides of interaction point and consists of 9 disks (on every side). The CMS silicon strip detector has about 9.3 million readout channels and provides coverage in region $|\eta| < 2.4$

It is worth noting, that two inner layers of the TIB and TOB, two inner rings of TID and TEC and outermost ring of TEC allow measurement of all three coordinates of passing particle thanks to non parallel orientation of the strips.

A charged particle passing through the tracker volume produces 15 tracker hits on average with spatial resolution from about $20\ \mu\text{m}$ to $50\ \mu\text{m}$ [17] (depending on distance to the beam). Reconstructed tracks momentum resolution (relative to track momentum) is typically 0.7% in central part of the detector and 3% near the tracker η boundaries [18].

Low occupancy of silicon tracker is needed for efficient reconstruction of particles tracks. For heavy ion collisions occupancy increases to 1% for pixel tracker and up to 20% for strip tracker. Nonetheless correct track reconstruction is still possible due to large number of measurement points for a given track.

Tracker of CMS experiment consists of $210\ \text{m}^2$ of silicon. It is the biggest device of this kind.

2.3. Electromagnetic calorimeter

Electromagnetic calorimeter (ECAL) used in CMS detector is constructed out of about 80000 lead tungstate (PbWO_4) crystals and is used for precise measurements of electrons and photons produced in collisions. ECAL is placed next to the silicon tracker with respect to the beam axis, covering pseudorapidity range $|\eta| < 3$.

A photon (or an electron) crossing crystals produces a cascade consisting of photons, electrons and positrons. Constituents of cascade cause scintillating light to appear in crystals, which is then measured by avalanche photodiodes. Lead tungstate crystals are optically isolated and supported by carbon fibre.

2.4. Hadron calorimeter

Hadron calorimeter is a set of the furthestmost detectors from the beam axis placed near the superconducting solenoid. It measures particles interacting via strong interaction.

Hadron calorimeter consists of four subsystems - Hadron Barrel Calorimeter (HB, covering range $|\eta| < 1.4$), Hadron Endcap Calorimeter (HE, $1.4 < |\eta| < 3$), Hadron Forward Calorimeter (HF, $3 < |\eta| < 5$) and placed outside the superconducting solenoid Outer Hadron Calorimeter (HO, $|\eta| < 1.25$).

2.5. Muon detectors

Muon system consists of four muon stations, each of cylindrical shape placed symmetrically around the beam axis, in the barrel region, and four muon stations in both of endcaps, each of a disk shape perpendicular to the beam axis [19].

Measurement of muon momenta and charge in CMS detector is done by combining information from silicon tracker with measurements from three different detectors placed outside of the solenoid - Drift Tubes (DT) covering barrel region ($|\eta| < 1.3$), Cathode Strips Chambers (CSC) in endcaps region ($0.9 < |\eta| < 2.4$) and Resistive Plate Chambers both in barrel and endcaps region ($|\eta| < 1.6$)².

2.5.1. Cathode Strip Chambers

Cathode Strip Chambers (CSC) are muon gas detectors placed in both endcaps, capable of functioning in high particle rate conditions. They consist of strips (radial to the beam axis) and closely placed thin wires, perpendicular to the strips. Both strips and wires are placed in a gas volume. Electrical potential difference between strips and wires leads to a multiplication of electrons left by ionization of passing charged particle (e.g. a muon). Use of strips and wires perpendicular to them allows measurement of all coordinates of passing charged particle. CSC are characterized by a good spatial resolution (from 100 to 200 μm , [20]) and relatively short reaction time (of about 4 ns).

2.5.2. Drift Tubes

Drift Tubes (DT) are muon gas detectors placed in the barrel region. Each Drift Tube contains a 2.5 m long wire, placed centrally in 4 cm wide, 1.5 cm thick gas volume of about same length. Measurement of trajectory of passing charged particle is performed by measuring drift time of electron cascade following muon passage. Each muon station consists of 12 layers of Drift Tubes organized in 3 Super Layers (SL). The innermost and outermost SL inside the muon station are placed parallel to beam axis, measuring R and ϕ coordinates of particle trajectory. The third (middle) SL is perpendicular to the beam axis, allowing measurement of η coordinate of passing muon³.

²RPC subsystem was designed to cover up to $|\eta| < 2.1$. Due to financial and technical reasons RPC chambers were installed up to $|\eta| < 1.6$. Increase of coverage in η is considered during one of forthcoming long breaks in LHC operation.

³DT chambers in the outermost muon station consist of 2 SL, measuring only R and ϕ track coordinates.

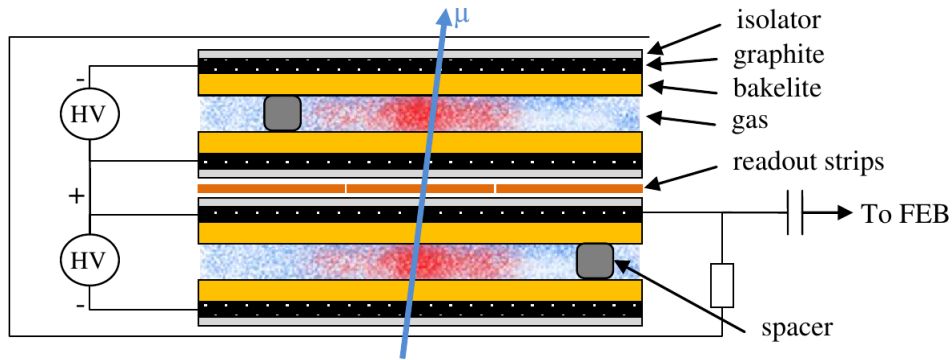


Figure 2.3.: Schematic view of the RPC chamber.

2.5.3. Resistive Plate Chambers

Resistive Plate Chambers (RPC) are reviewed in this section in greater detail than the CSC and DT ones in order to give a better background for content of Appendix C.

Resistive Plate Chambers are muon gas detectors placed both in barrel and endcaps regions. Schematic view of RPC chamber is shown on Figure 2.3. Chamber consists of two thin bakelite sheets separated by 2 mm wide gas gap. On outside of one of bakelite sheets readout strips (parallel to beam axis) are placed. Electron cascade caused by a passing charged particle is amplified by an electric field of about 9 kV. Current induced in the readout strips by moving cascade allows us to determine position of a passing particle.

In the CMS detector double gap RPC chambers are used - a second pair of bakelite sheets (also separated with 2 mm wide gas gap) is placed symmetrically with respect to the readout strips.

The RPC system used for data taking consists of three layers of chambers installed in endcaps region and up to 6 layers of chambers in barrel region.

RPC chambers are characterized by very good time resolution (of about 1.5 ns), allowing unambiguous bunch crossing assignment. Spatial resolution is limited by strip width and depends on detector conditions (which determine average cluster size, during the data taking average cluster size was of about 2 strips [21]). In barrel region RPC strip width is smallest for stations closest to the beam line (down to 2.3 cm), width increases for stations being farther from beam axis (up to 3.8 cm, strips have an approximately constant size in ϕ of about $\frac{5}{16}$ degrees). For endcaps region strips have a trapezoidal shape, allowing same constant size in ϕ as for barrel. Strip width varies from 1.5 cm (for innermost installed chamber of disk 1) up to 3.7 cm.

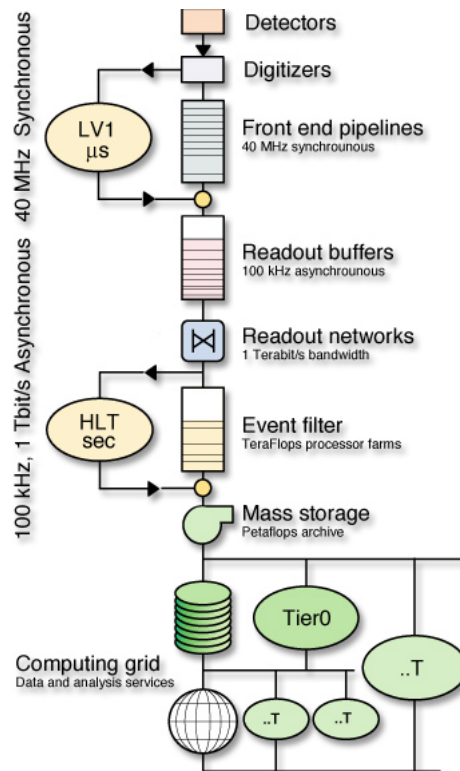


Figure 2.4.: Triggering, data acquisition and distribution in the CMS experiment.

2.6. Trigger and data acquisition

Construction of Large Hadron Collider allows collisions to occur every 25 ns (40 MHz)⁴. Size of data from single bunch crossing is up to 1.5 MB [22], therefore recording all events would require 40 TB/s of bandwidth available, which is beyond current technical possibilities. CMS experiment records data from about 200 bunch crossings in every second, hence the data stream needs to be reduced by 5 orders of magnitude. In order to fully take advantage of physics possibilities given by LHC it is crucial to effectively select interesting events on real time basis. This task is done by the trigger system of CMS experiment.

A schematic view of triggering, data acquisition and distribution in the CMS experiment is shown in Figure 2.4. Triggering is performed in two stages. In first stage 40 MHz frequency of collisions is reduced to a maximum rate of 100 kHz by Level-1 Trigger (L1). A decision (acceptance or rejection) must be taken for each event (every 25 ns) in very short time, limited by the length of the readout buffers. Due to the short decision time required L1 was implemented in dedicated electronics, using reconfigurable devices (such as Field-Programmable Gate Array; FPGA).

⁴During data taking in 2010, 2011 and 2012 collisions were separated by 50 ns.

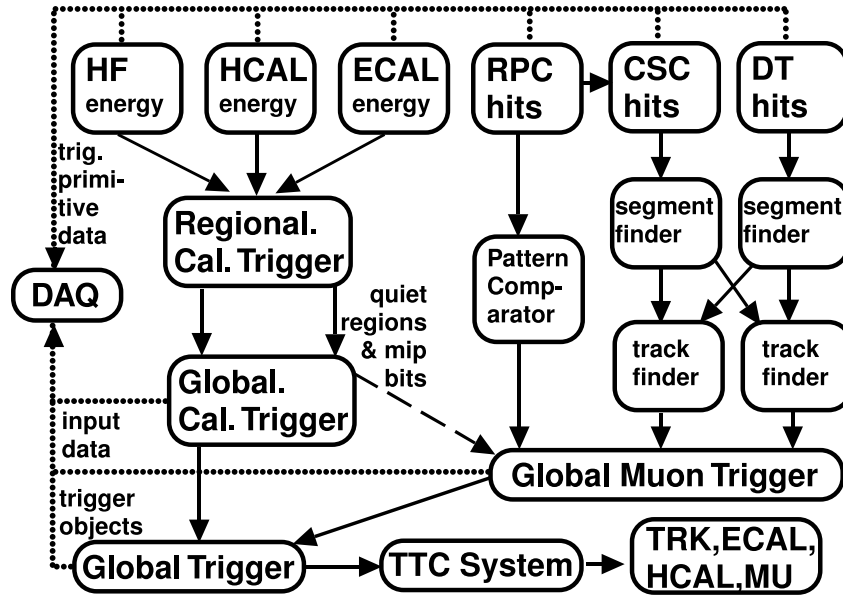


Figure 2.5.: Schematic view of Level-1 trigger

The CMS Global Trigger is a part of L1. Its decision is based on input from 2 subsystems - the L1 calorimeter trigger and L1 muon trigger (Figure 2.5, [23]). Due to vast volume of data and short reaction time required signals from the silicon tracker are not used for L1 decision.

L1 calorimeter trigger is subdivided into Regional Calorimeter Trigger (RCT) and Global Calorimeter Trigger (GCT). Aim of RCT is to find electron, photon, tau and jet candidates using data received from ECAL and HCAL detectors and send them to GCT (information on activity in calorimeter detectors is also sent from RCT to L1 muon trigger, which allows to calculate isolation of muon candidates). GCT selects four best candidates of each type and sends them to L1 Global Trigger. Missing transverse energy (MET) and total transverse energy are also calculated at GCT and transmitted to L1 Global Trigger.

L1 muon trigger consists of three independent muon candidate finders, corresponding to RPC, CSC and DT subsystems. Muon candidates are matched, based on their charge and position inside the detector by Global Muon Trigger (GMT). GMT selects up to eight best muon candidates (4 for barrel and 4 for endcaps regions) which are sent to L1 Global Trigger.

Candidates provided by GMT and GCT are used to develop L1 decision (accept or reject given event) by Global Trigger (GT). The L1 decision is transmitted via Trigger Timing and Control (TTC) system to all subdetectors. All trigger objects used to make the L1 decision (e.g. muon candidates from GMT) are recorded along with detector data.

Events accepted by L1 are then processed by High Level Trigger (HLT). On this stage data collected by all detectors of CMS (including silicon tracker) are used to determine trigger decision. HLT is realized on a farm of 792 computers with 9210 cores⁵ [24], on which dedicated software is run implemented inside the CMSSW application framework [25]. High Level Trigger reduces event rate to about 200 Hz [26]. Events accepted by the trigger system are saved to a persistent storage system, reconstructed and then distributed along several computing centers for analysis.

Computing resources of the CMS experiment are organized hierarchically in order to handle data stream coming from the detector [26]:

Tier-0 is a single and central computing center placed at CERN. Main task of Tier-0 center is to retrieve data recorded by the CMS detector, archive it, perform full reconstruction of events and distribute them along Tier-1 centers.

Tier-1 is a set of large computing centers placed around the world, having a fast data link with Tier-0 center. Tier-1 centers are required to re-reconstruct received events (if updated calibration constants are available), archive the data and to distribute the data among Tier-2 centers.

Tier-2 centers are usually smaller when compared to Tier-1 centers, however they are much more numerous than Tier-1 centers⁶. Their task is to receive data from Tier-1 centers and to provide sufficient bandwidth, computing power and data storage for data analyses. Tier-2 centers are also used for a production of Monte Carlo samples.

Tier-3 centers provide computing power and efficient access to the experiment data.

User analyses are run on Tier-2 and Tier-3 centers. Hierarchical structure and distributed system character allows efficient access to data, therefore helps data analysis.

Data analysis presented in this work was to a large extent computed in Warsaw Tier-2 centre, hosted by a Interdisciplinary Centre for Mathematical and Computational Modelling, University of Warsaw.

⁵As of May 2011

⁶In December 2011 CMS collaboration used 8 Tier-1 centers and about 50 Tier-2 centers.

2.7. Event reconstruction

Event reconstruction algorithms are implemented inside the CMSSW application framework (along with HLT algorithms, code for Monte Carlo simulations, Data Quality Monitoring and other) [25].

2.7.1. Track reconstruction

Track finding in the CMS experiment applies an iterative approach [27]. In first iterations tracks are found using very tight seeding and quality criteria. After each iteration all hits unambiguously assigned to reconstructed tracks are removed (and not used in next iterations). In every subsequent iteration seeding and quality criteria are lowered, allowing high reconstruction efficiency, while keeping rate of fake tracks low.

During 2010 and 2011 data taking track reconstruction consisted of 6 iterations. First three aimed at reconstructing tracks originating from the primary vertices (therefore a beamspot constraint was applied), while final three allowed reconstruction of secondary tracks (e.g coming from B decays or interactions with tracker material). Reconstructed tracks are clustered using Deterministic Annealing algorithm [28], which allows efficient and precise vertex determination.

In Figure 2.6 the CMS track reconstruction momentum resolution is shown [18]. Resolution measurement was done using J/ψ resonance decaying to μ pairs. Since muons momentum coming from J/ψ is of the order of several GeV/c, momentum determination is done basing on tracker measurements.

2.7.2. Muon reconstruction

Muon reconstruction in the CMS experiment depends on a good track reconstruction performed in the CMS tracker [29]. An independent track reconstruction is also performed using measurements only from the muon system (standalone-muon reconstruction). Two tracks (tracker and standalone) may be combined using following algorithms:

Global Muon reconstruction - every standalone-muon track is matched to a tracker track using distance at a common surface after extrapolating both tracks. A global fit is then performed using hits assigned both to the tracker track and the standalone-muon track, forming a so called global-muon track.

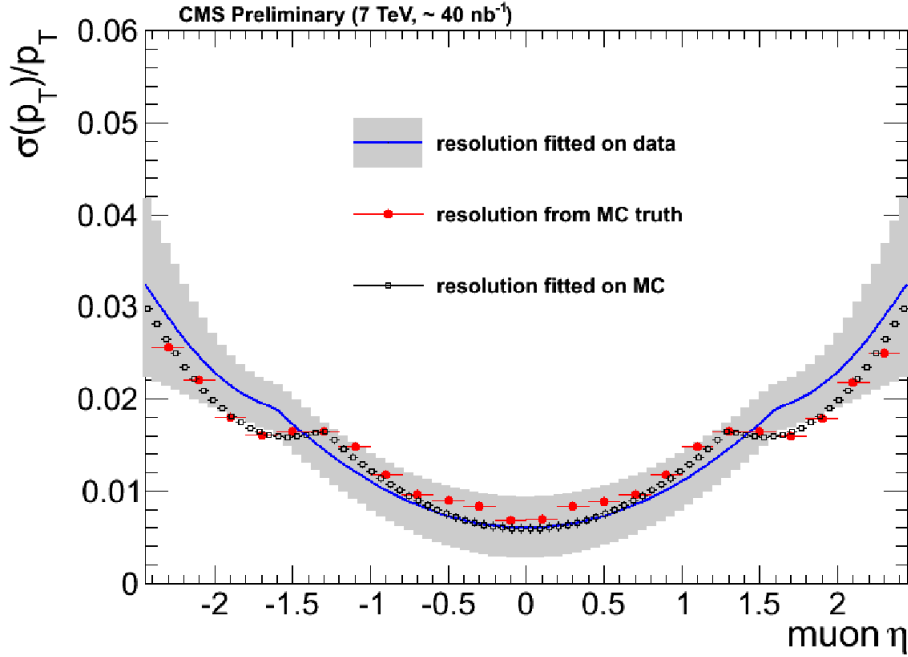


Figure 2.6.: Resolution of the CMS track reconstruction determined for data and Monte Carlo simulations [18].

Tracker Muon reconstruction - for each tracker track with momentum high enough ($p_T > 0.5 \text{ GeV}/c$ and $p > 2.5 \text{ GeV}/c$) a matching is performed to hits found in a muon system. Matching takes into account average energy losses and multiple scattering. A tracker track will be considered a Tracker Muon if at least one match is found to so called muon segment (a short track reconstructed inside a single muon chamber). Tracker Muon reconstruction allows good reconstruction efficiency for muons with very low momenta ($p \lesssim 5 \text{ GeV}/c$).

A comparison of momentum resolution of the CMS muon reconstruction is shown on Figure 2.7, separately for muon system only measurement, tracker only measurement and combined measurement [30]. The use of measurements from the silicon tracker and muon chambers leads to an improvement in momentum resolution for muons with large transverse momentum ($p_T \gtrsim 200 \text{ GeV}/c$) when compared to tracker only resolution.

2.7.3. Electron and photon reconstruction

Electron identification and reconstruction in the CMS experiment starts with electron preidentification, which is done by two algorithms - ECAL and tracker driven [31]. In ECAL driven algorithm so called ECAL superclusters are found. A supercluster is created for one or more ECAL clusters, forming a region narrow in η and wide in ϕ . Characteristic

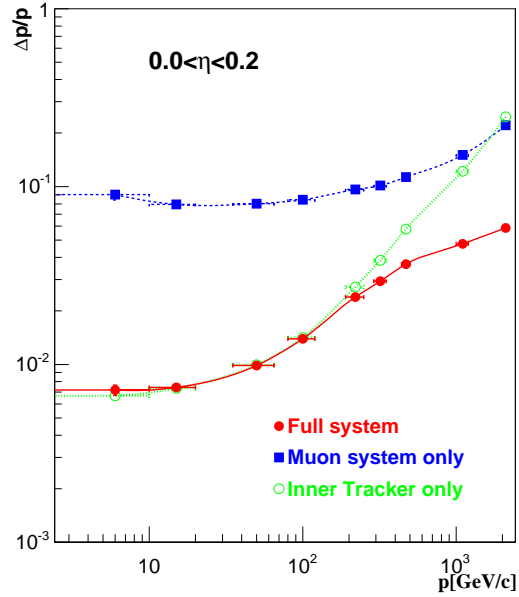


Figure 2.7.: Momentum resolution of the CMS muon reconstruction for tracker only, muon system only and combined (full) muon reconstruction [30] (study based on simulation).

shape of the supercluster is due to radiation coming from the electron, while it propagates through the tracker material in the magnetic field.

ECAL driven algorithm is complemented by tracker driven algorithm, in which reconstructed tracks are matched to ECAL clusters. After matching is performed a Multivariate Analysis (MVA) based preselection is applied, based on track and ECAL hit quantities [32].

Preidentified electron candidates are matched to track seeds, consisting of pairs or triplets of pixel hits. Electron tracks are then reconstructed using a Gaussian Sum Filter (GSF) [33], which models for electron energy losses.

In Figure 2.8 relative electron reconstructed energy resolution obtained for superclusters is shown [34]. The resolution calculated using $Z \rightarrow ee$ events for 2011 data, varies from 1% to 4% for barrel region (depending on η) and is about 5% for endcap region. For the endcap region compatibility between the expected (simulated) and observed resolutions is slightly worse when compared to the barrel region. Electron energy measurement is dominated by the supercluster resolution for electron energies higher than 25 GeV. Below that value electron energy measurement benefits from measurements performed with tracker.

Superclusters are also used as seeds to a photon finding algorithm [35]. Since photon is likely to convert to an electron pair before reaching ECAL (due to relatively large amount of material before ECAL), use of superclusters, whose shape is wide in ϕ and narrow in η ,

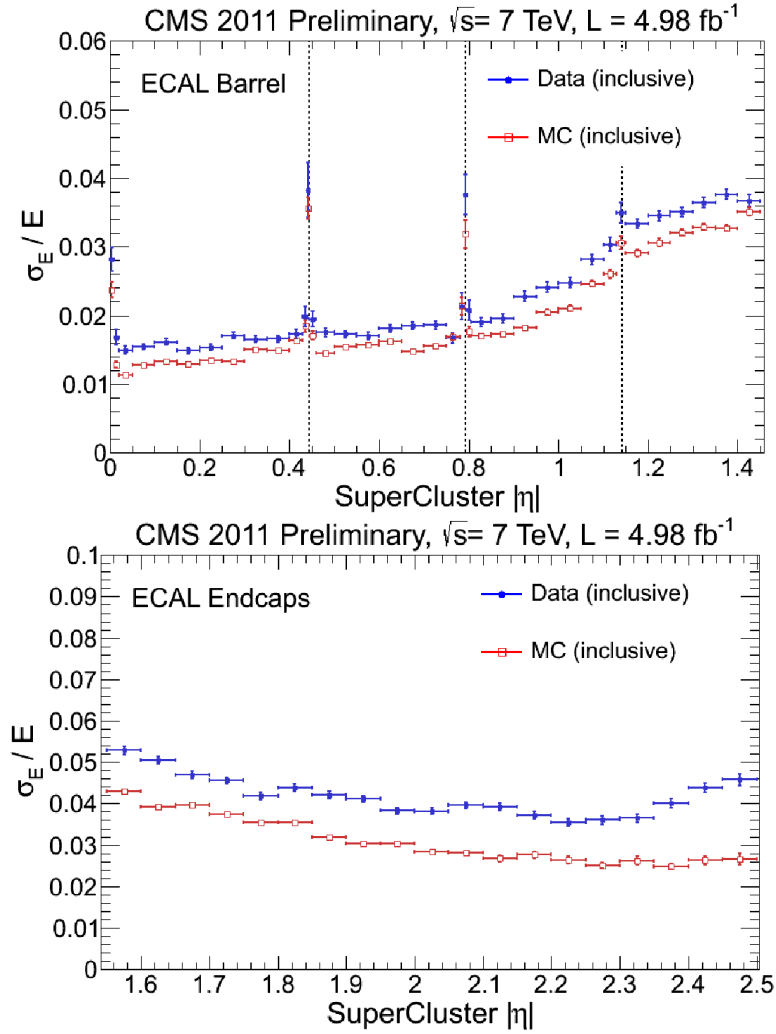


Figure 2.8.: Relative electron reconstructed energy resolution obtained for superclusters for barrel and endcap regions for recorded data and simulation.

allows photon reconstruction for converted photons. In such cases supercluster is used as a seed for track reconstruction of electrons coming from conversion, reconstructed photon is marked as converted and linked to a conversion data.

In cases, where no conversion was found, photons are identified basing on requirements of energy ratio between HCAL and ECAL deposits below specific threshold, particular supercluster shape and supercluster isolation, calculated independently using tracker tracks, ECAL and HCAL deposits.

2.7.4. Particle Flow

The Particle Flow (PF) event reconstruction algorithm provides unique description of every event by unfolding detector response into list of particles present in the event[36].

Algorithm starts with tracks reconstructed in the tracker and clusters found separately in each of calorimetry sub-detectors (e.g. endcap ECAL or barrel HCAL). Every track is linked to all clusters that are close enough in (η, ϕ) plane to the track extrapolation. Maximum allowed distance is of the order of granularity of given calorimeter. A link can be also established between two calorimeter clusters (e.g. between ECAL and HCAL clusters), also depending on (η, ϕ) distance.

Tracks found in silicon tracker and in the muon system can also be linked. Matching is performed by a global fit between the two tracks (muon and tracker one). Link is established if χ^2 value of the fit is acceptable.

Set of linked elements form a block. Every block is characterized basing on predefined criteria, e.g. a block consisting only of ECAL and HCAL clusters will be identified as a photon or as a neutral hadron, depending on energy deposits ratio in two calorimeters.

After particle identification a cluster calibration is performed. Since calorimeter response may be different for different particles, corrections are applied depending on the particle type. Particle energy is then determined by combining calorimeter and tracker measurements (if available).

As a result of above algorithm a list of so called PF candidates (list of reconstructed particles) is obtained for every event. This list is then used by further reconstruction algorithms, e.g. jet finding or identification of hadronic decays of τ leptons.

2.7.5. Missing transverse energy

Missing transverse energy (MET) is a probe for neutral particles, that do not produce deposits in the detector (such as neutrinos). Presence of such particles usually leads to an imbalance of the total momentum, visible in plane transverse to the beam line. In the CMS experiment three main algorithms are present to reconstruct MET:

Calorimetric MET algorithm sums all calorimeter deposits (up to $|\eta| < 5$) above the noise threshold [37]. Since muons deposit very small fraction of their energy, calculated MET is corrected using muons momenta measured in tracker and muon system. In addition corrections are applied to reconstructed jets in order to compensate for nonlinear response of the calorimeters

Track-corrected MET algorithm uses MET value reconstructed by Calorimetric MET algorithm as a starting point [38]. Tracks identified as muons (since already corrected by Calorimetric MET algorithm) or electrons (as expected to be properly

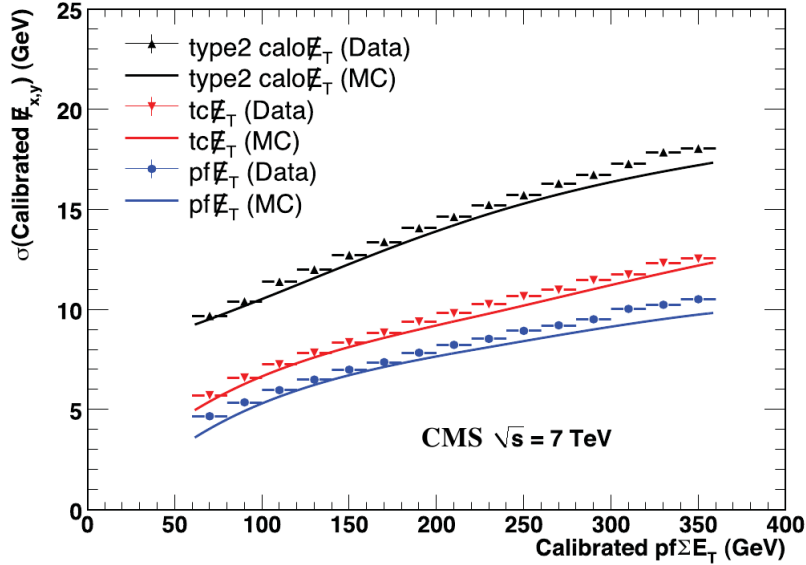


Figure 2.9.: Resolution of different CMS MET reconstruction algorithms for 2010 data and Monte Carlo simulations. Type2 $\text{calo}\cancel{E}_T$ corresponds to calorimetric MET algorithm (corrected for pile-up presence and with calorimeter energy calibration constants applied), $\text{tc}\cancel{E}_T$ to track-corrected MET, $\text{pf}\cancel{E}_T$ to Particle Flow MET.

measured by ECAL) are not used for corrections. All remaining reconstructed tracks are interpreted as coming from pions. For every track an expected deposit is calculated for calorimeter detectors (using a parametrization depending on tracks ϕ , η and momentum) and then subtracted from calorimeter response. At the same time track momentum at the vertex is added to the MET value. Tracks with $p_T > 100$ GeV/c (as expected to be properly measured by the calorimeters) are not used for corrections calculation. MET value is also corrected using reconstructed tracks with very low momenta ($p_T < 2$ GeV/c), that don't produce deposits in the calorimeters (due to bending in the magnetic field)

Particle Flow MET algorithm calculates MET by summing all transverse momenta of the particles earlier reconstructed by the Particle Flow algorithm. Since energy corrections are already applied for PF candidates, calculated MET doesn't need further corrections

Resolution of different MET reconstruction algorithms can be estimated from events, in which two jets are present. In such events MET value is expected to be equal to zero. Therefore the MET algorithms performance can be probed by measuring the MET distribution width for such events. In Figure 2.9 results of such study [39] are shown for described algorithms. MET reconstructed using the Particle Flow algorithm has the best resolution, while results obtained for the Calorimetric MET algorithm are the worst.

2.7.6. Jets

In standard CMS reconstruction three jet finding algorithms are used - SISCone [40], k_t [41] and anti- k_t [42]. Later one is used by default by most of analyses.

Jet finding starts with a list of four momenta of objects present in the event (e.g. calorimeter hits). For every object i a distance d_{iB} from the beam (B) is introduced and for pairs of objects i and j a distance d_{ij} is defined in a following way:

$$d_{ij} = \min(k_{ti}^{-2}, k_{tj}^{-2}) \frac{\Delta_{ij}^2}{R^2}$$

$$d_{iB} = k_{ti}^{-2}$$

In above equations $\Delta_{ij}^2 = (\eta_i - \eta_j)^2 + (\phi_i - \phi_j)^2$, k_{Ti} is the transverse momentum of given object, R is an adjustable radius parameter (typically $R = 0.5$ is used in majority of analyses).

After computing above values objects with the smallest distances d_{ij} are merged. If for a given object distance from the beam d_{iB} is smaller than any other distance d_{ij} (the distance to any other object), the object is considered final and removed from the list. Procedure is repeated till no objects are left.

Anti- k_t algorithm is used to reconstruct jets using different data for algorithm input:

Calorimeter jets are reconstructed by using only deposits coming from HCAL and ECAL calorimeters. Deposits that are below noise threshold (defined separately for every detector) are not used for jet finding.

Jet-Plus-Tracks algorithm jets are reconstructed basing on idea similar to the one used in Track-corrected MET algorithm. Algorithm starts with jets found by a calorimeter jets algorithm. For tracks matched by extrapolation to a given jet, expected calorimeter deposit is calculated and removed from the jet energy. At the same time jet energy is increased by a track momentum.

Particle Flow Jets are reconstructed using candidates provided by the Particle Flow reconstruction algorithm.

In Figure 2.10 momentum resolution of reconstructed jets for above algorithms is shown. The resolution was measured directly from data by exploiting the momentum conservation for events with two jets present [43]. The resolution is the best for Particle Flow based algorithm.

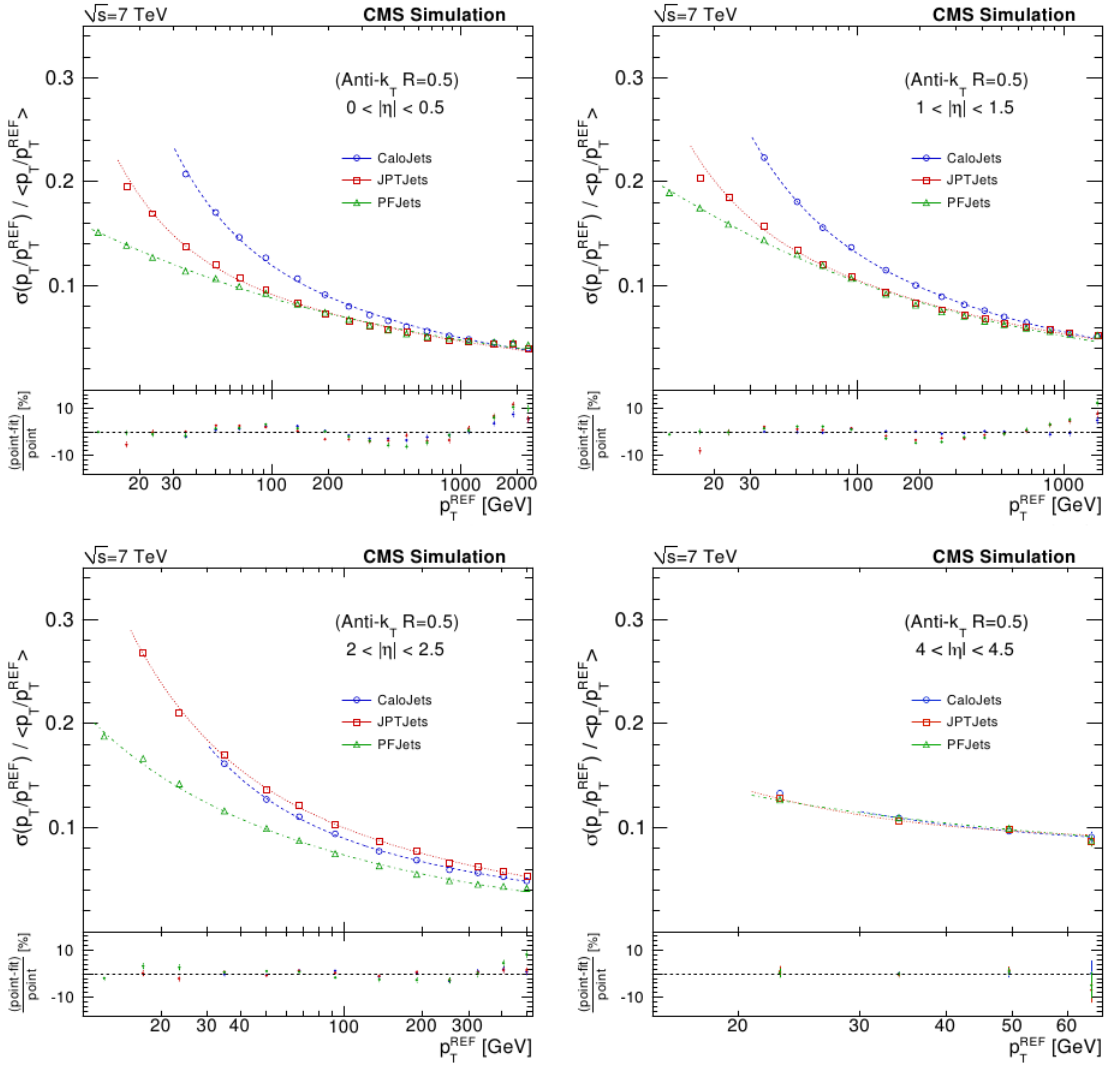


Figure 2.10.: Jet transverse momentum resolution.

2.7.7. Hadronic τ decays identification

Hadronic τ decays are reconstructed using Hadron Plus Strips Algorithm [44]. Starting point of the reconstruction is a Particle Flow jet, in which all possible τ decays are found using PF charged hadrons and close to them PF photons and PF electrons. Reconstruction is performed for all PF jets present in given event. Photons and electrons are clustered topologically into so called strips with size not bigger than $\Delta\eta \times \Delta\phi = 0.05 \times 0.20$. Goal of the strip forming is to handle cases in which one or both photons (coming from π^0 particle produced by τ decay) convert into electrons. Calculated invariant mass of the strip is required to be consistent with π^0 mass.

A PF jet will be reconstructed as Particle Flow hadronic τ if it falls into one of following categories:

Single Hadron - aimed for reconstructing $\tau \rightarrow h\nu$ or $\tau \rightarrow h\pi^0\nu$ decay modes (later one in cases, where π^0 has very small energy)

Hadron Plus Strip - for reconstructing $\tau \rightarrow h\pi^0\nu$ decay mode. Invariant mass of a hadron and strip system is required to be equal to the mass of ρ resonance (770Mev)

Hadron Plus Two Strips - for reconstructing $\tau \rightarrow h\pi^0\pi^0\nu$ decay mode. Invariant mass of a hadron and strip system is required to be equal to the mass of a_1 resonance (1260Mev)

Three Hadrons - for reconstructing three prong tau decays. It is required, that reconstructed charge of a system is equal to $\pm e$

Considered hadronic decay modes cover 95% percent of all possible hadronic τ decay modes [45].

To further discriminate against backgrounds faking hadronic τ decays (e.g. QCD) isolation criteria may be applied, requiring that activity (corrected for τ constituents) in cone $\Delta R < 0.5$ around given τ direction is not bigger then a certain threshold.

To discriminate against cases in which muon is misidentified as hadronic τ , matching criteria between leading τ track and hits in the muon system may be applied. To further discriminate against muons, a (MIP)-veto can be applied in which ratio of HCAL energy deposited by leading charged hadron to its momentum is greater than a certain value.

For anti electron discrimination a Boosted Decision Tree (BDT, [46]) method is used. Hadronic τ candidates are classified depending on their decay mode, detector region (barrel or endcaps) and whether a GSF (electron like) track is assigned to τ leading charged candidate. According to assigned class, a different variable set is used for BDT input, including:

- Ratio of HCAL energy deposit of leading charged candidate and its momentum
- Number of neutral constituents of the τ
- τ candidate momentum
- Fraction of τ candidate momentum carried by its neutral decay products

Chapter 3.

Determination of Drell-Yan $\tau\tau$ background using embedding of simulated τ decays in Drell-Yan $\mu\mu$ events

As described in Chapter 1 a creation of a $\tau\tau$ pair via a Drell-Yan (DY) process is the main irreducible background process in the analysis presented in this dissertation. The DY process involves annihilation of two quarks into a Z boson (or a virtual photon) decaying to a pair of oppositely charged leptons of the same type (Figure 3.1). For high invariant mass of produced leptons DY process occurs with the same cross section not depending on lepton type in the final state.

In order to estimate the DY $\tau\tau$ background it is possible to exploit DY $\mu\mu$ and DY $\tau\tau$ production similarities. Events, in which a muon pair is produced (with properties consistent with properties of the DY $\mu\mu$ event), can be transformed into a DY $\tau\tau$ like event. The detector response to selected muons is replaced with simulated decays of two τ leptons. Momenta of the simulated τ leptons are determined from the momenta of replaced muons. Such mixed events (with data partially registered by the detector and partially coming from the simulation) can then be used to estimate DY $\tau\tau$ background contribution by applying an exactly same set of selections as used for a given search (e.g. search of the Higgs boson decaying to τ pairs). In order to properly estimate the event yield a correction is necessary to account for the underlying DY $\mu\mu$ selection efficiency. Technique of replacing muons with simulated τ decays is often called τ embedding.

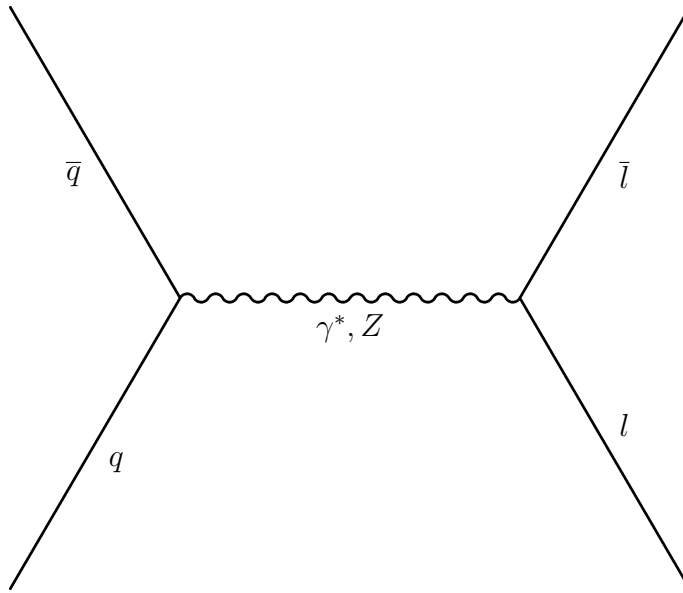


Figure 3.1.: Drell-Yan process. Two quarks annihilate into a Z boson (or a virtual photon) decaying to a pair of oppositely charged leptons of the same type.

3.1. Possible approaches to τ embedding

There are several approaches to implement the embedding technique:

Raw embedding - muon response is replaced by the one coming from simulated τ decay on level of raw detector data (e.g. mixing of recorded and simulated event parts for ECAL is done by adding the response signals of avalanche photodiodes - the one coming from the detector and the one obtained from simulation). This approach is currently impossible due to the differences in tracker geometry description present in CMSSW and the real detector geometry¹.

Particle Flow embedding - embedding is performed during Particle Flow event reconstruction [48]. PF candidates list originating from the DY $\mu\mu$ event is modified by removing selected muons and adding reconstructed products of simulated τ decays. On such mixed PF candidates list remaining part of PF reconstruction algorithms (e.g. hadronic τ decays reconstruction) is run. Such approach allows to avoid problems due to differences in the geometry description present in CMSSW.

¹Geant4 toolkit [47] is used in CMSSW to simulate particles passage through the matter. Tracker detector geometry used for this simulation is approximate, not accounting for small shifts in real detector position with respect to the design one. Effects of misalignment are taken into account on later level - by shifting the position of reconstructed tracker hits into position consistent with the real (detector) one.

Reconstructed hit embedding - is an intermediate approach, in which reconstructed hits (for calorimetry and muon detectors) and reconstructed tracks (for silicon tracker) are mixed. Reconstructed tracks of the selected muons are removed from the reconstructed tracks list. Reconstructed hits in the calorimeters and in the muon system are also removed. Such approach allow us to avoid problems caused by differences in tracker geometry description while keeping reconstruction sensitive to pileup effects in the other detectors.

In this dissertation Particle Flow embedding method is described and used. Reconstructed hit embedding method is currently in preparation and is not discussed here.

3.2. Particle Flow embedding procedure

3.2.1. DY $\mu\mu$ event selection

Events in which a μ pair is produced in DY process can be selected with very high efficiency by selecting events with two reconstructed and isolated muons present with high transverse momentum coming from same interaction vertex. At the same time background rate is kept on very low level. To select DY $\mu\mu$ events following selection criteria are applied:

- Event should pass a double muon trigger path. On the trigger level no muon isolation criteria are applied. Exact thresholds on the transverse muon momenta were changing with the growing LHC instantaneous luminosity. For the first runs recorded in 2011 threshold was 6 GeV/c (symmetrically for both muons). For 2011 runs with the highest luminosity trigger thresholds were 17 GeV/c for leading and 13 GeV/c for subleading muon.
- Two reconstructed muons must be present with $|\eta| < 2.4$
- Transverse momentum of leading muon must be higher than 20 GeV/c
- Transverse momentum of subleading muon must be higher than 15 GeV/c
- Both muons must pass track quality criteria:
 - Each of muons must be reconstructed both as a global and as a tracker muon
 - At least 11 valid tracker hits should be assigned to the track, with at least one recorded in the pixel detector
 - Normalized χ^2 of the track fit should be smaller than 10

- Number of good hits in the muon system should be greater than 0 for global muon
- Number of matched hits in muon system should be greater than 1 for tracker muon
- Both muons must originate from the same interaction vertex
- Muons must be of the opposite charge

Both muons are required to be isolated. Isolation value is calculated by summing transverse momenta of charged particles reconstructed by the Particle Flow algorithm present in a $\Delta R < 0.4$ cone around the muon direction. Particles used for calculating of the isolation value are required to originate from the same interaction vertex as muon. Relative muon isolation variable is defined as

$$\text{Iso}_{\text{emb}}(\mu) = \frac{\sum p_{\text{T}}^{\text{charged}, \Delta R < 0.4}}{p_{\text{T}}^{\mu}}$$

In Figure 3.2 a distribution of the muon isolation variable is shown for leading and subleading muons. Muon isolation requirement in DY $\mu\mu$ selection present in the embedding must be chosen carefully. Too tight DY $\mu\mu$ isolation requirement may lead to a bias in a number of DY $\tau\tau$ events estimated with the embedding method (number of events will be underestimated).

Isolation requirements present in $H \rightarrow \tau\tau$ analysis are stronger than muon isolation requirement defined above. Muon (μ_{τ}) produced in a given τ decay is always softer than a muon (μ_{src}) from which given τ momentum was determined. Therefore the isolation value of μ_{τ} will be always higher than the isolation value of μ_{src} ².

When selecting hadronic τ decays candidates absolute isolation is used (a sum of particles momenta present in the cone is not divided by the transverse momentum of τ_{had}). The isolation value is calculated in wider cone ($\Delta R < 0.5$) when compared to the muon one (see Section 2.7.7). The τ_{had} isolation criteria is predominantly stronger than muon isolation requirement defined above. In order to verify this, a τ_{had} -like isolation criteria was applied to muons produced in the DY $\mu\mu$ process with transverse momenta greater than 15 GeV/c. To all passing events a selection $\text{Iso}_{\text{emb}} < 0.1$ was applied. Only negligible fraction of events (order of 10^{-3}) failed the second selection. Therefore in conclusion $\text{Iso}_{\text{emb}} < 0.1$ DY $\mu\mu$ selection is loose enough to not to bias the number of events obtained with the embedding method.

²Moreover neutral particles contribute to isolation of μ_{τ} , enlarging the calculated value.

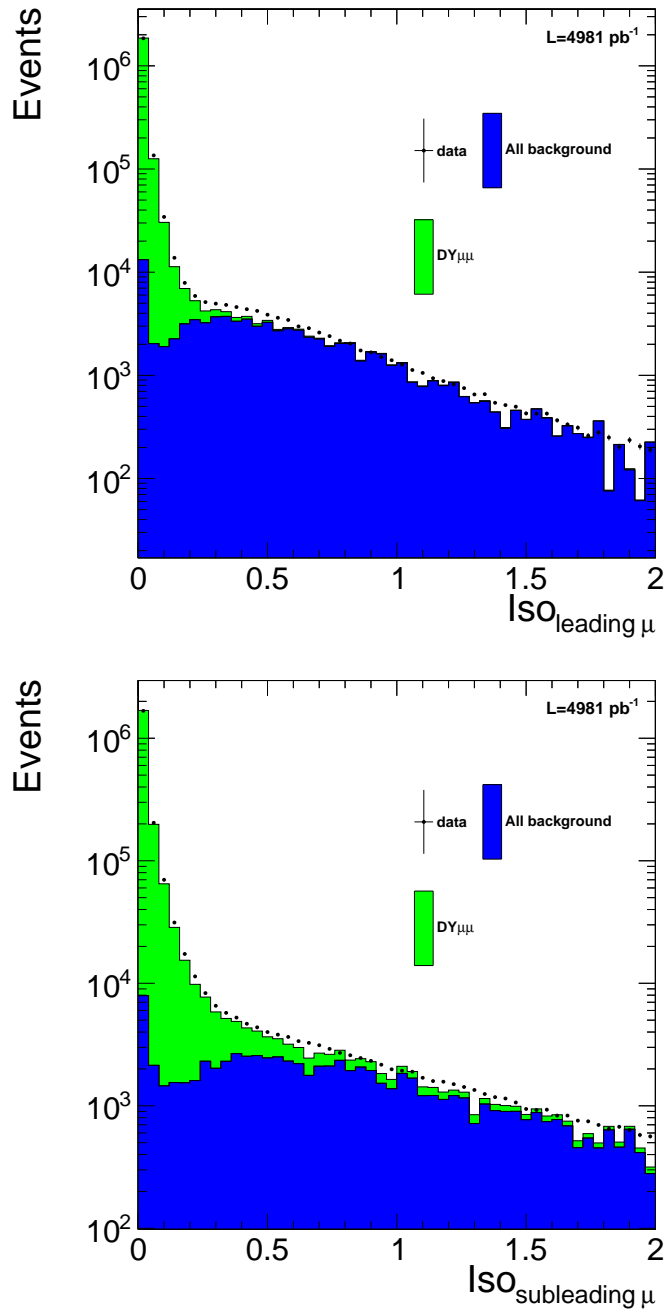


Figure 3.2.: Distribution of the isolation variable for leading (top) and sub-leading (bottom) muons. Both muon are required to have isolation variable smaller than 0.1.

Muon isolation requirement should not be too loose, since it may unnecessarily increase the background contribution. In Figure 3.3 spectrum of inverse mass of two muon system is shown for DY $\mu\mu$ and background processes after applying all selection criteria. Expected background contribution is of order of 0.3%.

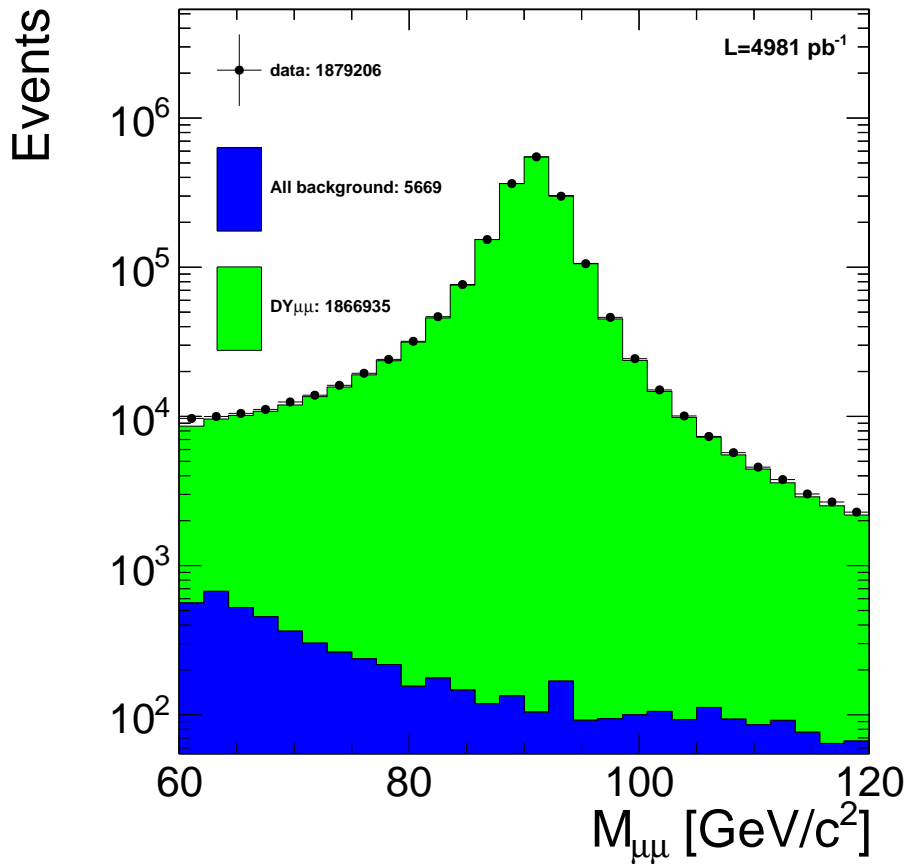


Figure 3.3.: Invariant mass spectrum of the selected muon pairs with observed and expected event yields.

3.2.2. Creation and simulation of $\tau\tau$ event

An event description in HepMC [49] format is created for every selected DY $\mu\mu$ event. Two interaction vertices (with position taken from the muon interaction vertex) are created. In first interaction vertex a Z boson is produced. In the second one two τ leptons of opposite charge are produced from Z boson decay. Momenta of the τ leptons are determined using momenta of DY $\mu\mu$ pair. While setting the momenta a correction for higher τ lepton mass is applied.

The τ leptons present in the event are decayed using the TAUOLA toolkit [50]. After the decay is performed so called visible transverse momentum is calculated. Transverse momenta of τ decay products are summed, excluding the momenta of neutrinos. In order to more efficiently use available event statistics, visible transverse momentum of each τ lepton is required to be greater than a certain threshold. The decay of $\tau\tau$ event is repeated 1000 times. First decay products fulfilling the visible momentum criterion is then used for

simulation. In order to avoid biasing the momentum spectra, an event weight is calculated based on number of successful (fulfilling the visible momentum requirement) decays.

Event simulation and reconstruction is then performed using standard workflow inside CMSSW until the PF candidates list is obtained.

3.2.3. Cleaning and mixing

List of the PF candidates obtained for simulated $\tau\tau$ event is added to the list of PF candidates from the original DY $\mu\mu$ event. From the later list DY muon pair is removed. The resulting list is then used for remaining part of the PF reconstruction (e.g. MET determination or identification of hadronic τ decays).

Resulting hybrid event partially comes from the detector data and partially comes from the simulation. It can be processed by user analysis code after minor code modifications. Required modifications come mainly from necessity of applying weights on the event by event basis.

3.2.4. Method discussion

The Particle Flow embedding method for estimation of DY $\tau\tau$ background process is a data driven method. It has several advantages over the use of fully simulated DY $\tau\tau$ samples:

Reduced dependence on Monte Carlo - embedded events partially come from the simulation and partially from the data. Therefore several sources of systematic uncertainties are avoided, e.g. uncertainty of the parton density functions or of simulation of the underlying event.

Correct experiment conditions - when simulated Monte Carlo samples are used weights must be often applied in order to correct for differences between simulation and collected data. For embedded samples applying of some weights is unnecessary, e.g. the distribution of number of reconstructed vertices in the event for the embedded samples is always correct.

Luminosity measurement independence - embedding method allow us to obtain correct normalization of the DY $\tau\tau$ background without the use of the luminosity measurement.

Since the Particle Flow embedding is performed on relatively late level of the event reconstruction, described method has several limitations:

Not all reconstructed objects are available - since embedding is performed during the Particle Flow reconstruction, only objects reconstructed by the Particle Flow algorithm may be used in the analysis (e.g. use of calorimeter only isolation will give unsatisfactory results). This is not a limitation for $H \rightarrow \tau\tau$ analyses in which objects obtained from the Particle Flow reconstruction are only used.

Trigger response must be modeled - the trigger simulation in CMSSW (both for L1 and HLT) requires raw detector data, which is not available for the hybrid event. Therefore trigger decision is not available and event weighting is necessary in order to account for trigger efficiencies.

Pileup effects may not be present - since mixing is performed after reconstruction of the Particle Flow candidates, reconstruction of τ decay products occurs always in very clean environment, i.e. without interference due to presence of other proton-proton interactions in the same bunch crossing. Particle Flow reconstruction itself is to a good extent immune to pileup effects thanks to very good detector granularity. Therefore Particle Flow based embedding is expected not to include bias due to missing pileup effects. For 2011 data the only observed effect in samples obtained with Particle Flow embedding method was higher than expected reconstruction efficiency for endcap electrons in events with more than 15 vertices [51].

Events obtained with the embedding technique may be used to estimate contribution from DY $\tau\tau$ background process in the analyses involving τ leptons in the final state. Description of such procedure can be found in Chapter 4.

3.2.5. Systematic uncertainties of the embedding method

DY $\mu\mu$ selection efficiency

In order to obtain event yield from the Particle Flow embedded samples a correction factor is applied for the underlying DY $\mu\mu$ selection efficiency. Correction is determined using DY $\mu\mu$ simulated sample. Two sources of the uncertainty are considered - muon momentum scale resolution uncertainty and uncertainty of Parton Density Functions used to generate simulated sample.

Uncertainty due to muon momentum scale was determined by reevaluating the DY $\mu\mu$ selection efficiency after varying the measured muons momentum by 0.2% up and down. Change in the selection efficiency was negligible.

Error estimate due to the PDF uncertainty was calculated. The DY $\mu\mu$ selection efficiency was determined separately for each of 41 PDF sets (central value set and 40 error sets) provided in the CTEQ66 library. Half of difference between the smallest and the biggest of calculated values was taken as the PDF uncertainty. Obtained uncertainty was 0.9% ³.

Muon Radiation

Muons are much lighter particles than τ leptons, therefore radiate more often. Occurrence of an extra photon can lead to a different efficiency for τ_{had} isolation requirement. In order to measure this effect all selection criteria present in the $H \rightarrow \tau\tau \rightarrow \mu\tau_{\text{had}}$ search were applied to real DY and MC embedded samples, with the τ_{had} isolation requirement modified - only charged candidates assigned to the same interaction vertex as reconstructed τ_{had} were used to calculate the isolation. Events selected in such way are then required to pass a full τ_{had} isolation criterion (including photons and neutral particles). Obtained efficiency of such selection was 0.8295 ± 0.0046 for real DY sample and 0.8359 ± 0.0043 for MC embedded sample. Obtained efficiencies are consistent, therefore the effect of higher muon radiation on τ_{had} isolation can be neglected.

Distribution of difference of muon transverse momenta before and after photon radiation relative to muon transverse momentum before the radiation is shown in Figure 3.4. Higher probability of radiation for muons (when compared to the radiation probability for τ leptons) can also lead to differences in the momentum distribution of τ leptons simulated in the embedding procedure. Therefore an 0.6% (conservatively average value of 0.55% from Figure 3.4 was rounded up) is added to the scale uncertainty of reconstructed hadronic tau decays and muons produced in τ lepton decays.

Di-muon Background

Expected background contribution to the DY $\mu\mu$ spectrum after applying all selection criteria described in Section 3.2.1 is 0.3% (Figure 3.1). Conservatively double of this value will be added in quadrature to the uncertainty of DY $\tau\tau$ event yield estimation obtained using the Particle Flow embedding method.

³PDF uncertainty was obtained during the τ_{had} reconstruction study, see Appendix B.

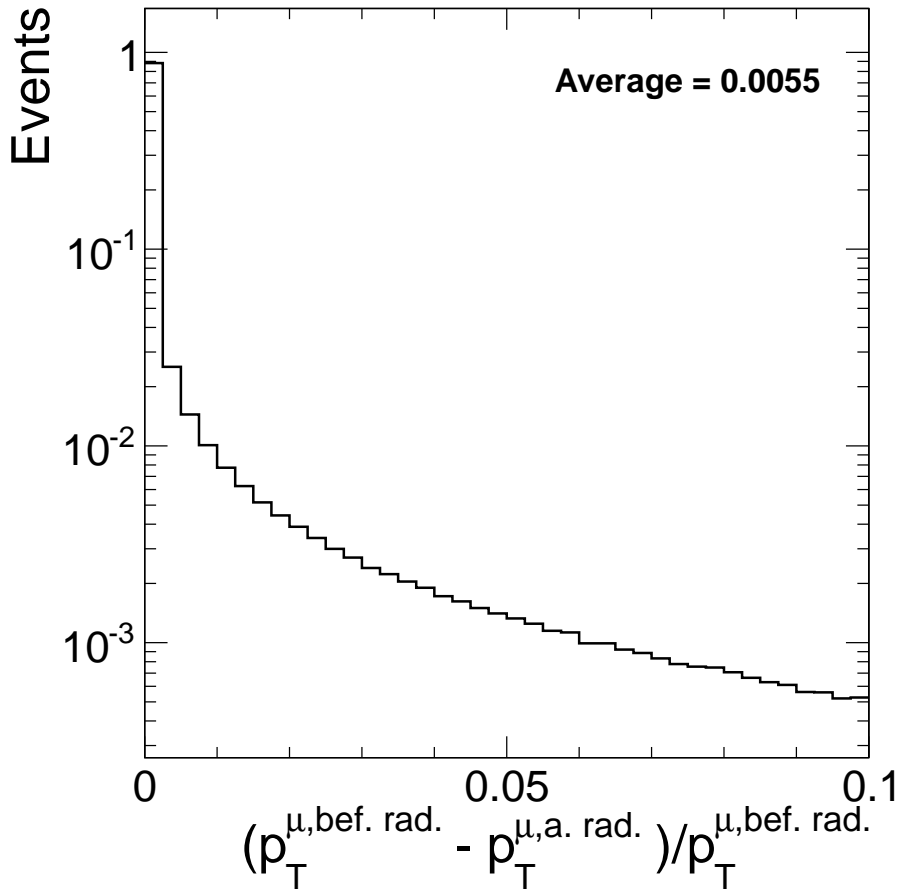


Figure 3.4.: Distribution of difference of muon transverse momenta before ($p_T^{\mu, \text{bef. rad.}}$) and after ($p_T^{\mu, \text{a. rad.}}$) photon radiation relative to muon transverse momenta before the radiation.

Muon Momentum Measurement

Muon momenta are measured with some finite precision. The effect can be illustrated by comparing the distribution of invariant mass of muon pairs obtained using uncalibrated and corrected muon momenta⁴ (Figures 3.5, 3.6). Since momenta of τ pairs simulated in the embedding technique are determined using momenta of the selected muons, precision of muon momentum measurement affects the momentum scale of simulated τ leptons. Therefore an extra 0.5% due to muon momentum scale uncertainty⁵ is added to scale uncertainties of muons (coming from τ decays) and reconstructed hadronic τ decays.

⁴Muon momentum corrections from SIDRA fit were applied for simulated samples [52].

⁵Muon transverse momentum scale varies with amplitude about 0.5% as a function of phi [53], [54].

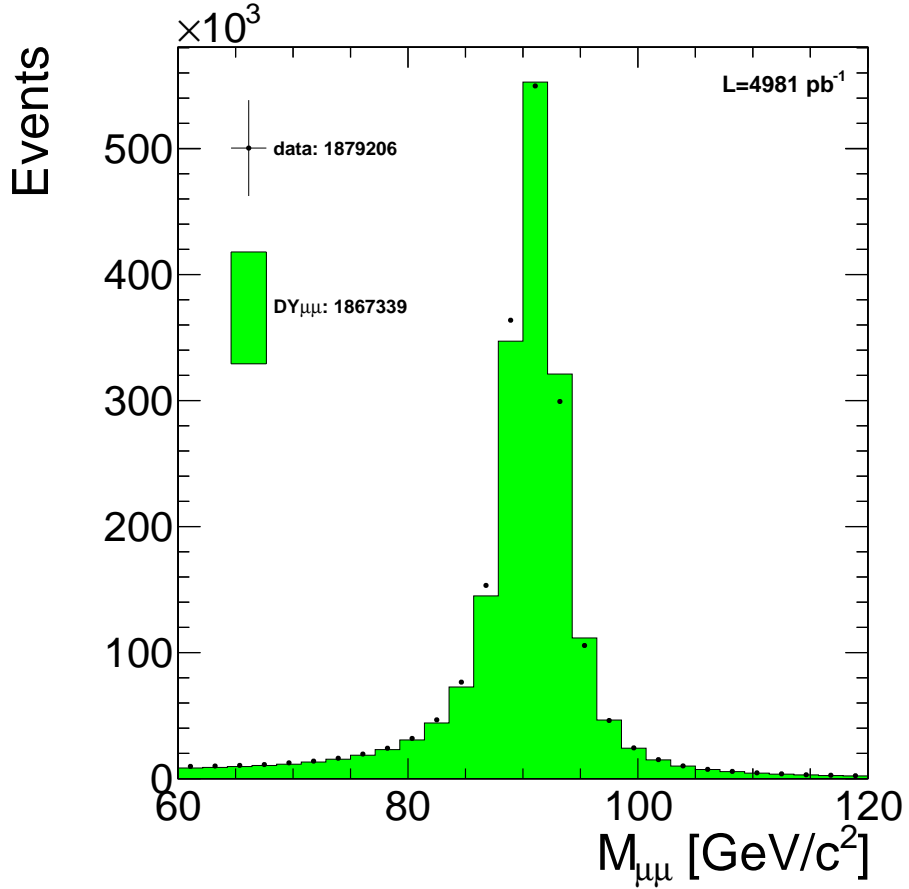


Figure 3.5.: Distribution of the invariant mass of muon pairs before the muon momentum calibration. The background contribution is not visible on the plot.

3.2.6. Method validation

In order to validate the Particle Flow embedding method a closure test was performed - event yields obtained with a DY $\tau\tau$ simulated sample and a Particle Flow embedding technique (applied to DY $\mu\mu$ simulated sample) were compared. To both samples all selection criteria present in the $H \rightarrow \tau\tau \rightarrow \mu\tau_{\text{had}}$ search (see Chapter 4) were applied.

Every event from the embedded on MC sample passing the $H \rightarrow \tau\tau \rightarrow \mu\tau_{\text{had}}$ selection criteria is weighted in order to account for the underlying DY $\mu\mu$ selection efficiency and $\mu\tau_{\text{had}}$ trigger efficiency. Trigger related weight is calculated depending on η and p_T of τ_{had} and muon pair. Trigger efficiency curves were obtained separately for τ and muon trigger parts [55]. Correction $w_{\mu\mu}$ for DY $\mu\mu$ was calculated using following formula:

$$w_{\mu\mu} = \frac{1}{\text{eff}_{\mu\mu}}$$

$$\text{eff}_{\mu\mu}(p_T^{\text{lead}}, \eta^{\text{lead}}, p_T^{\text{sublead}}, \eta^{\text{sublead}}) = \text{eff}^{\text{lead}}(p_T^{\text{lead}}, \eta^{\text{lead}}) \cdot \text{eff}^{\text{sublead}}(p_T^{\text{sublead}}, \eta^{\text{sublead}})$$

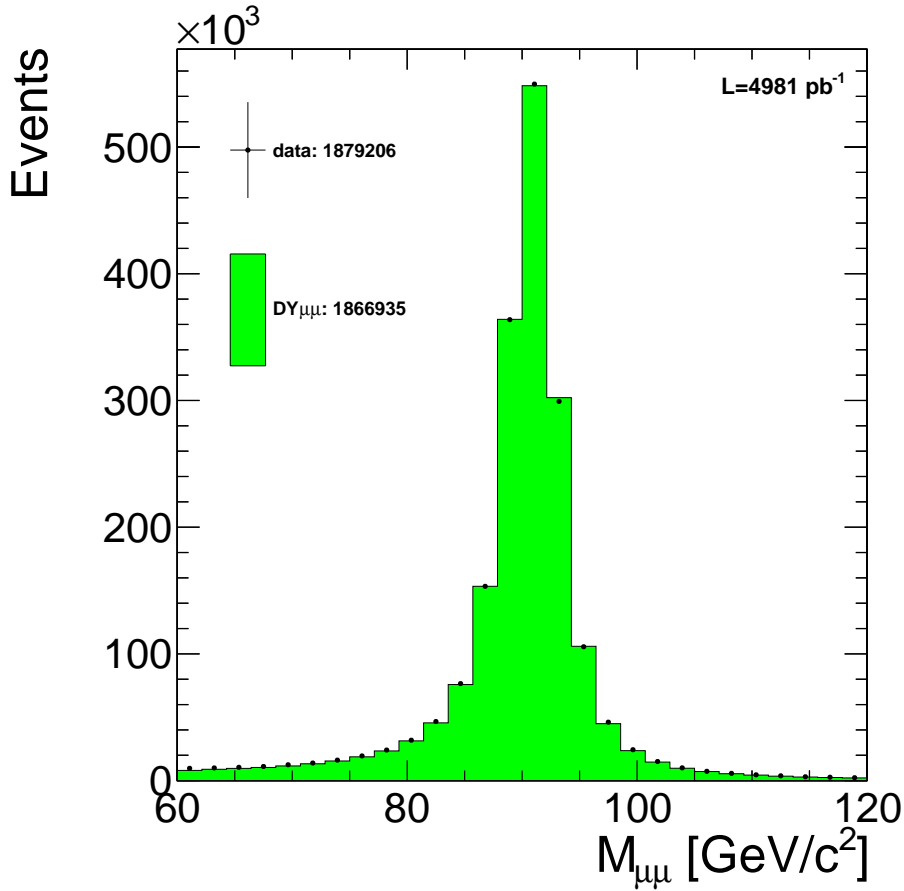


Figure 3.6.: Distribution of the invariant mass of muon pairs after muon momentum calibration. The background contribution is not visible on the plot.

The $p_T^{\text{lead}}, \eta^{\text{lead}}, p_T^{\text{sublead}}, \eta^{\text{sublead}}$ variables are transverse momenta and pseudorapidities of leading and subleading muons respectively. The eff^{lead} term describes the efficiency of the trigger requirement and the leading muon selection requirements (track quality, η and transverse momentum). Term $\text{eff}^{\text{sublead}}$ describes efficiency of selecting the subleading muon by applying the track quality, η and momentum requirements. This term is calculated with respect to all events that pass the trigger and leading muon selection. It is worth noting, that both efficiency terms do not contain isolation selection efficiency. As it was shown before this selection is looser than isolation requirements present in $H \rightarrow \tau\tau \rightarrow \mu\tau_{\text{had}}$ selection criteria.

Result of the closure test is shown on Figure 3.7. Event yield obtained with the embedding MC sample is 0.7% smaller than one obtained with the DY $\tau\tau$ simulated sample. As a conservative estimate double of this difference is added to the systematic uncertainty of DY $\tau\tau$ event yield estimated with the Particle Flow embedding method. Mass distribution obtained by the embedding method is shifted to the lower values when compared to one obtained from the DY $\tau\tau$ sample. Such shift is expected due to muon

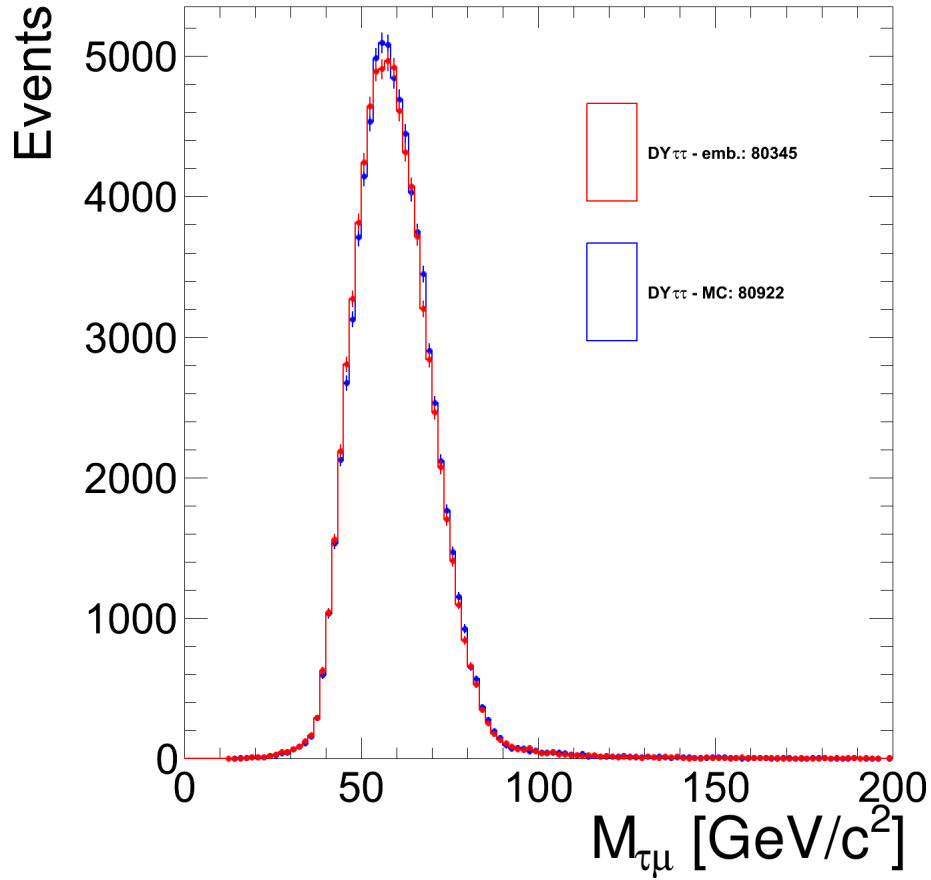


Figure 3.7.: Closure test of Particle Flow embedded method.

radiation in underlying DY $\mu\mu$ event and underlying muon momentum measurement (see Section 3.2.5). Shape uncertainty was evaluated by varying the momenta by 1.1% (0.6% due to muon radiation, 0.5% due to muon momentum measurement uncertainty; addition is done in conservative linear way) up and 0.5% down (here only uncertainty due to muon momentum measurement is considered, since radiation related effect is expected to lower the τ momenta) of τ_{had} and muons present in events passing $H \rightarrow \tau\tau \rightarrow \mu\tau_{\text{had}}$ analysis selection criteria. Obtained shape uncertainty for mass distribution is shown on Figure 3.8 (shapes normalization is the same as in the closure test). Similarly shapes are compared for other variables used in the analysis (Figures 3.9- refrys:val5). Compared shapes are consistent within obtained error bands and statistical uncertainties.

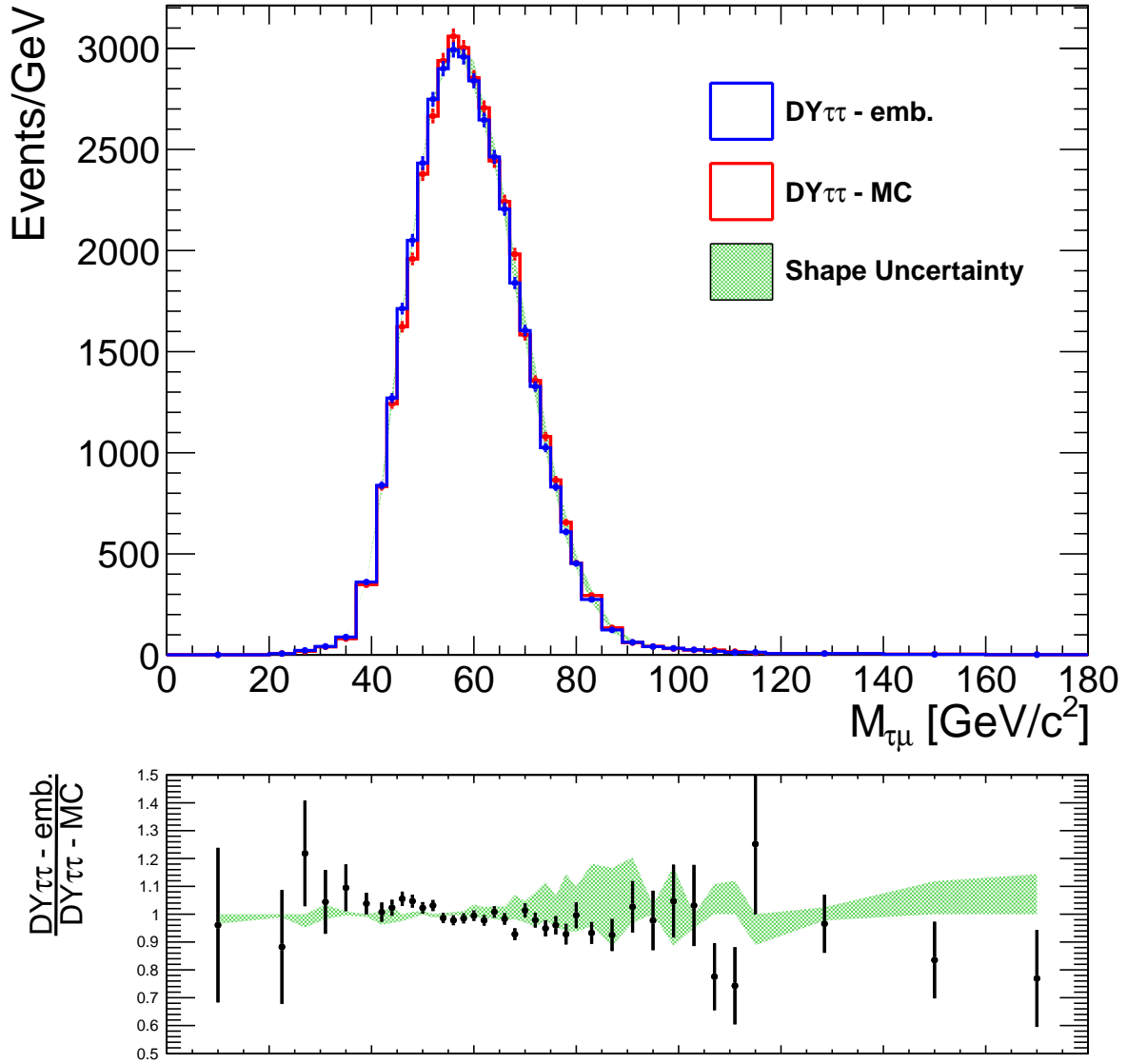


Figure 3.8.: A comparison of invariant mass distribution for embedded and real DY simulated samples. Error bars indicate statistical error. Green band indicate shape uncertainty obtained by varying muon and τ_{had} momenta by 1.1% up and 0.5% down.

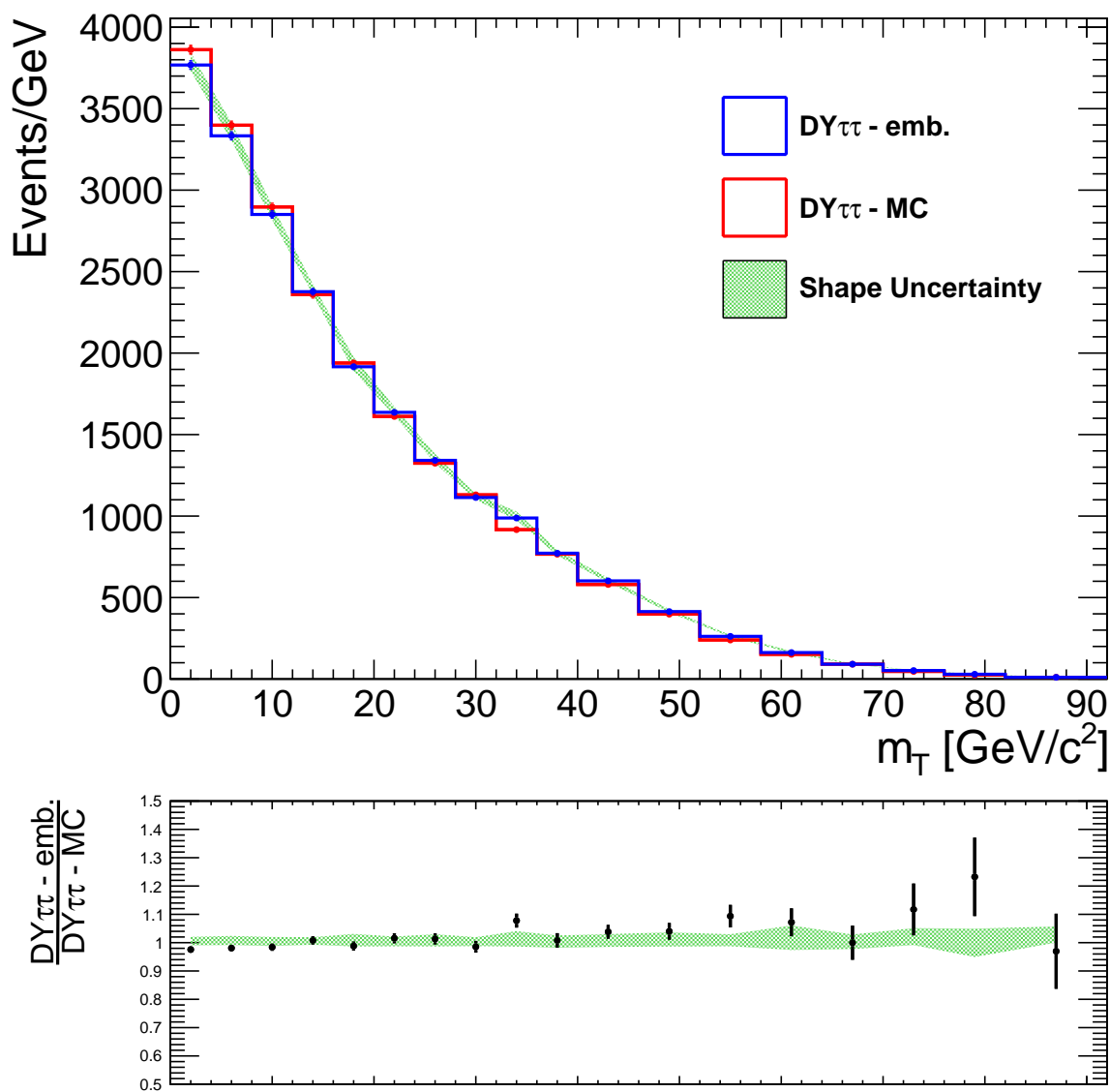


Figure 3.9.: A comparison of the transverse mass distribution obtained for embedded and real DY simulated samples (selection requirement on the transverse mass was omitted).

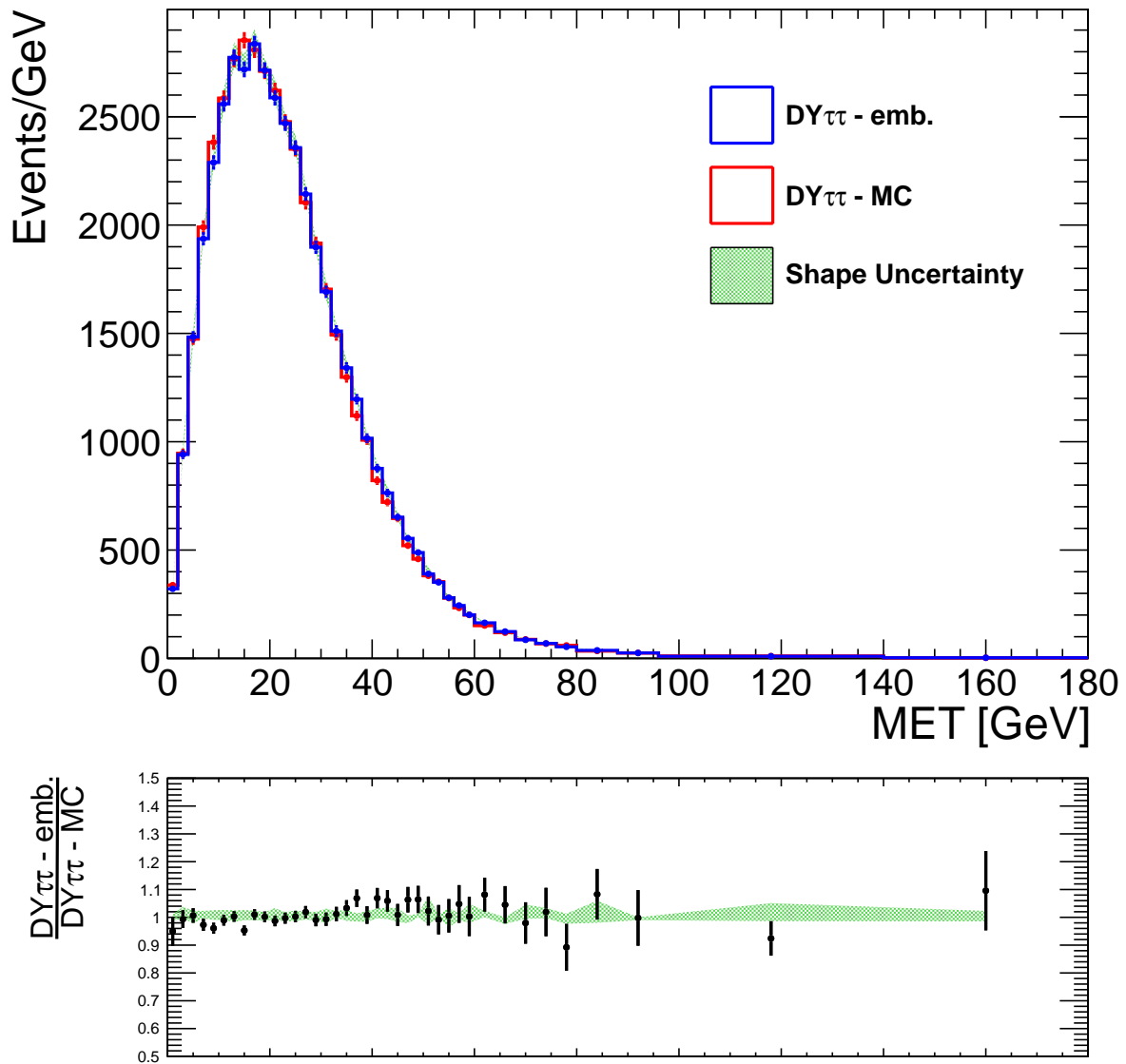


Figure 3.10.: A comparison of missing transverse energy distribution for embedded and real DY simulated samples (selection requirement on the transverse mass was omitted).

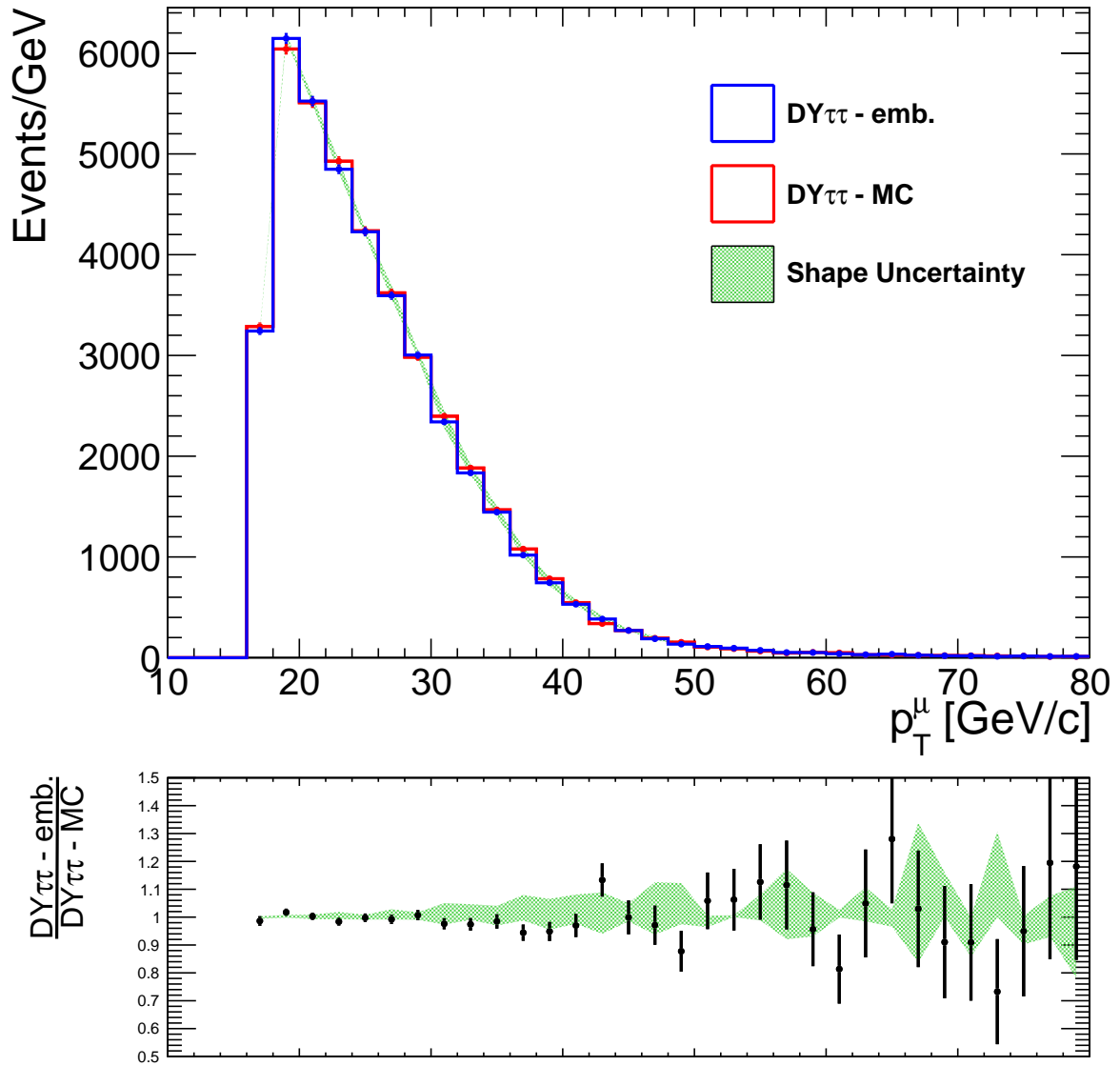


Figure 3.11.: A comparison of reconstructed muon transverse momenta distribution for embedded and real DY simulated samples.

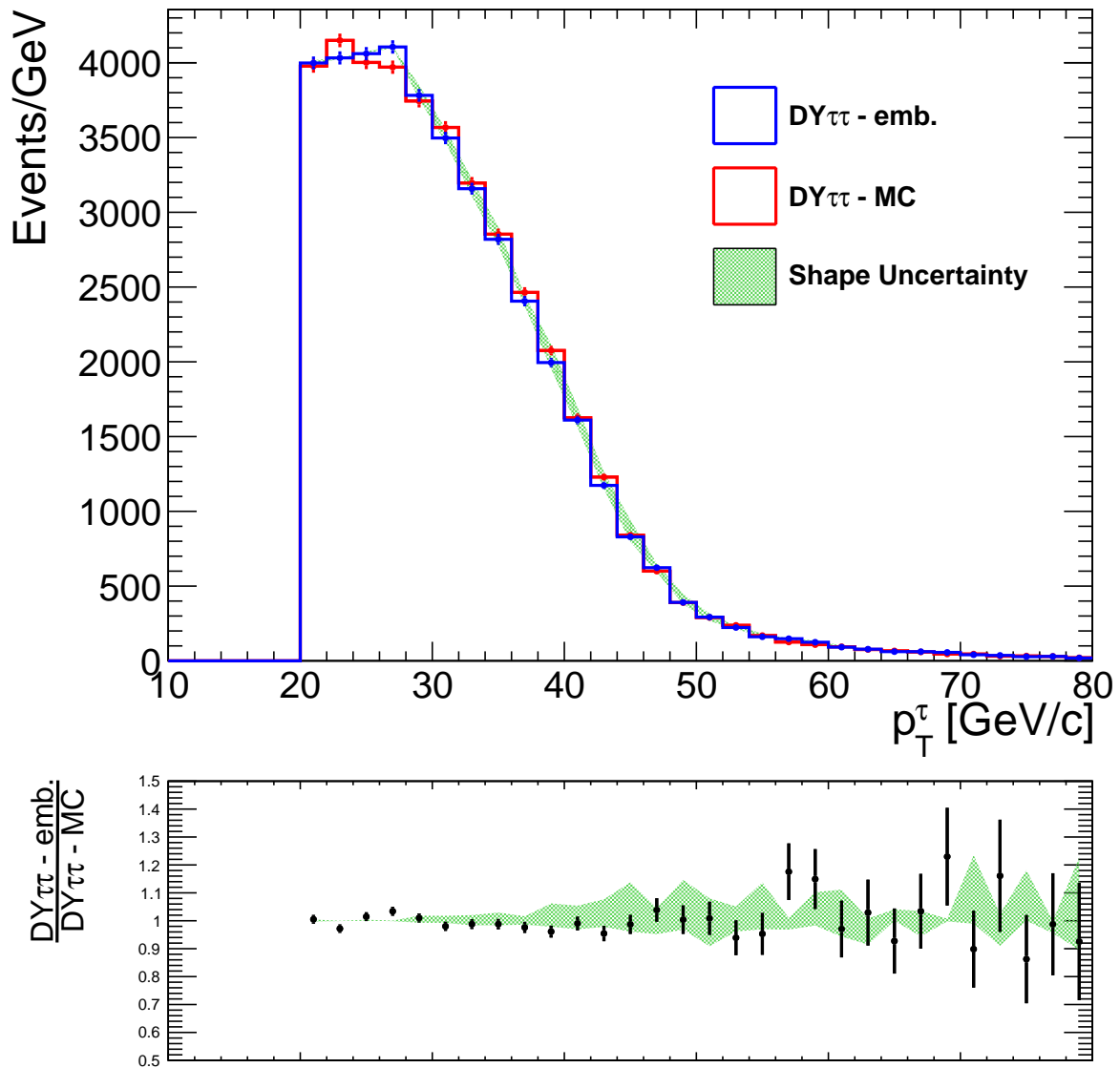


Figure 3.12.: A comparison of reconstructed τ_{had} transverse momenta distribution for embedded and real DY simulated samples.

Chapter 4.

$H \rightarrow \tau\tau \rightarrow \mu\tau_{\text{had}}$ search in the CMS experiment

In this chapter application of the embedding method in the search for the SM Higgs boson in the $\rightarrow \tau\tau \rightarrow \mu\tau_{\text{had}}$ final state is presented. Total recorded integrated luminosity¹ used in this analysis is 4981 pb^{-1} . Analysis presented here is a simplified version of the public CMS analysis presented in [56]. Differences between those two analyses are:

- In this analysis only $\mu\tau_{\text{had}}$ final state is considered.
- In this analysis visible mass of $\mu\tau_{\text{had}}$ pair is used. In the public CMS analysis full mass reconstruction algorithm (Secondary Vertex Fit algorithm; SVFit) of the di- τ system is used. Use of the SVFit algorithm leads to a better separation of the Higgs signal and the DY $\tau\tau$ background.
- Volume of data used for the public CMS analysis is slightly smaller, corresponds to 4.6 fb^{-1} .
- In this analysis events fulfilling the online and offline selection requirements are assigned to one of two categories - Vector Boson Fusion (VBF) like (with two high energetic jets separated in η present, not overlapping with the $\mu\tau_{\text{had}}$ pair) and non-VBF like. The CMS public analysis uses finer categorization.
- In the CMS public analysis embedded samples are used to obtain shapes of the DY $\tau\tau$ background. Normalization procedure depends on the luminosity and DY cross section measurements performed by the CMS experiment. In this analysis luminosity and cross section independent method is presented².

¹After applying official selection criteria of good data quality runs.

²In 2012 DY $\tau\tau$ normalization in the CMS public $H \rightarrow \tau\tau$ analysis was luminosity independent. In order to properly estimate number of DY $\tau\tau$ events a control region in DY $\mu\mu$ was defined.

Whenever it was possible results from the internal CMS note [55] (note supporting the CMS public analysis) were reused.

4.1. Event selection

4.1.1. Online selection

All events are required to fulfill an online (trigger) criteria. A presence of an isolated muon and reconstructed hadronic decay of τ lepton during the HLT reconstruction were demanded. Exact momentum thresholds on the transverse muon and τ_{had} momenta were changing with the growing LHC instantaneous luminosity. In the first runs recorded in 2011 thresholds were 12 GeV/c for muon and 10 GeV/c for reconstructed hadronic decay of tau lepton). In runs with the highest luminosity trigger thresholds were 15 GeV/c for muon and 20 GeV/c for the hadronic decay of tau lepton.

4.1.2. Offline selection

Every event fulfilling the trigger criteria must have a muon present along with reconstructed hadronic decay of the τ lepton as described in Section 2.7.7. All events are required to have a good reconstructed primary vertex present - vertex distance to the beamspot position must be smaller than 15 cm in z coordinate and 2 cm in the plane transverse to the beam. Number of degrees of freedom of the vertex fit is required to be greater than 3. For every event a vertex with the highest sum of squared transverse momenta is chosen.

Muon present in the event must fulfill following selection criteria:

- Muon must be reconstructed both by global and tracker muon reconstruction algorithms
- $p_{\text{T}}^{\mu} > 17$ GeV/c
- $|\eta^{\mu}| < 2.1$
- Impact parameter in the transverse plane $|d_0|$ should be smaller than 0.045 cm (calculated with respect to the selected vertex)
- Impact parameter in the longitudinal direction $|d_z|$ should be smaller than 0.2 cm (calculated with respect to the selected vertex)

- Muon must pass track quality criteria:
 - At least 11 valid tracker hits should be assigned to the track, with at least one coming from the pixel detector
 - Normalized χ^2 of the track fit should be smaller than 10
 - Number of good hits in the muon system should be greater than 0 for global muon
 - Number of matched hits in the muon system should be greater than 1 for tracker muon

Muon coming from τ decay is expected to be isolated. Isolation is calculated by summing transverse momenta of particles reconstructed by the Particle Flow algorithm present in a $\Delta R < 0.4$ isolation cone around the muon direction. Particles identified as photons or neutral hadrons are required to have a transverse energy greater than 0.5 GeV. Particles identified as charged hadrons are required to come from the same interaction vertex as muon. Additionally particles with the direction very close to the one of the muon are excluded from the sum ³.

In order to account for a presence of the neutral particles originated from different vertices than the selected one, so called $\Delta\beta$ correction is applied to the transverse momentum sum. Transverse momenta of all (coming from any interaction vertex) charged hadron candidates with direction within the isolation cone are summed. Following the CMS estimation this sum is corrected by a factor of 0.5 in order to estimate the amount of the energy coming from the neutral particles originating from other vertices.

In this analysis isolation relative to muon transverse momentum is used. Isolation variable is calculated using following formula:

$$I(\mu) = \frac{\sum p_{\text{T}}^{\text{charged}} + \max(\sum p_{\text{T}}^{\text{gamma}} + \sum p_{\text{T}}^{\text{neutral}} - \Delta\beta, 0)}{p_{\text{T}}^{\mu}}$$

Muons are required to have $I(\mu) < 0.1$.

Reconstructed hadronic τ decays (τ_{had} ; see Section 2.7.7) present in the event must fulfill following selection criteria:

- $p_{\text{T}}^{\tau_{\text{had}}} > 20 \text{ GeV}/c$

³ ΔR distance between muon and particle must be greater than 0.0001 for charged hadrons, and 0.01 for photon and neutral hadron candidates.

- $|\eta^{\tau_{\text{had}}}| < 2.3$
- Impact parameter of the leading track in the longitudinal direction $|d_z|$ should be smaller than 0.2 cm (calculated with respect to the selected vertex)
- τ_{had} is required to be isolated - sum of the transverse momenta of reconstructed charged and neutral PF candidates (corrected for momenta of τ_{had} constituents) is calculated in $\Delta R < 0.5$ cone. As in the muon case charged candidates are required to originate from the same interaction vertex as τ_{had} . Also similarly to the muon case a $\Delta\beta$ correction is applied to the transverse momentum sum. Calculated isolation value is required to be smaller than 2 GeV/c (absolute isolation value is used).
- In order to discriminate against cases in which a muon is misidentified as hadronic τ decay, leading τ_{had} track should not be reconstructed as muon or have a match to reconstructed tracks in the muon chambers. Additionally a (MIP)-veto is applied for all τ_{had} reconstructed as single prong decay - HCAL energy deposited by leading charged hadron relative to its momentum is required to be greater than a certain value.
- τ_{had} should not fail the anti electron discriminator (for details see Section 2.7.7)

To further suppress events coming from the background processes sum of muon and τ_{had} charges is required to be equal to zero. ΔR distance between muon and τ_{had} should be greater than 0.5.

In order to suppress events in which a muon is produced in a W boson decay and a jet misidentified as τ_{had} is present, a transverse mass calculated for the muon and MET momenta

$$m_T(\mu, \text{MET}) = \sqrt{2 \cdot p_T^\mu \cdot \text{MET} \cdot (1 - \cos(\Delta\Phi(\mu, \text{MET})))}$$

is required to be smaller than 40 GeV/c².

In order to enhance the sensitivity of this search events fulfilling above requirements are assigned to one of following categories:

VBF - events are required to have two tagging jets j_1, j_2 with transverse momenta higher than 30 GeV/c each. Tagging jets are required to be well separated from each other ($\Delta\eta(j_1, j_2) > 4$) and from selected muon or τ_{had} (with $\Delta R > 0.3$). No additional jets with $p_T > 30$ GeV/c are allowed in between the tagging jets. Invariant mass of the tagging jet system should be greater than 400 GeV/c²

Non-VBF - for all events that have not met VBF category requirements

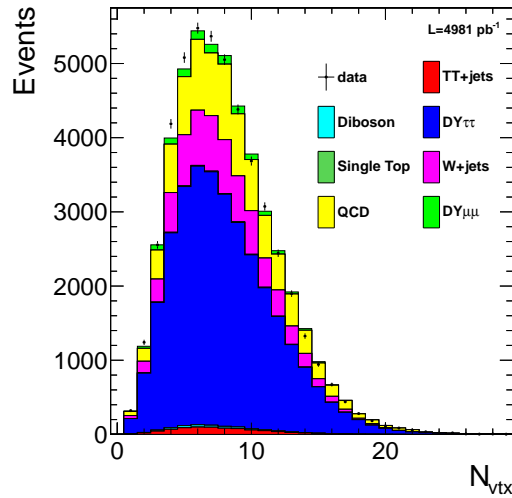


Figure 4.1.: Distribution of number of reconstructed primary vertices after reweighting is applied.

4.2. Event yield estimation

4.2.1. Summary of DATA to MC corrections

Distribution of number of pile-up events is different in recorded LHC events and in the simulated samples. Since this analysis is expected to be sensitive to pileup, simulated events were reweighted in order to obtain correct distribution of pile-up. Number of reconstructed primary vertices is expected to be directly related to the number of pile-up interactions present in the event, therefore is a natural test of reweighting procedure. Distribution of number of reconstructed primary vertices is shown in Figure 4.1.

The trigger efficiency was found to be different between simulated samples and the recorded data. Correction was applied (depending on p_T and η of muon and τ_{had}) in order to obtain correct efficiency and distribution shapes (efficiency curves from [55] were used). Similarly a correction for muon reconstruction efficiency is applied. Expected and observed distributions of main variables after applying all cuts used in this analysis are shown on Figures 4.2-4.4.

4.2.2. Estimation of DY $\tau\tau$ background

DY $\tau\tau$ process is the source of the main irreducible background for this search. To estimate contribution coming from this process the Particle Flow embedding technique is applied to all events recorded during LHC runs fulfilling DY $\mu\mu$ selection criteria (as described in

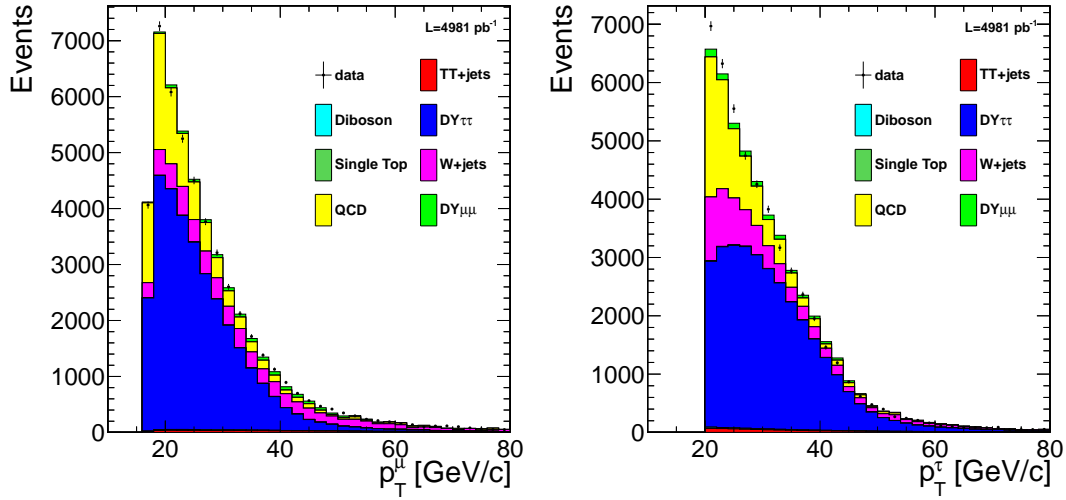


Figure 4.2.: Expected and observed distributions of reconstructed transverse momentum of muons (left) and τ_{had} (right) for non-VBF category.

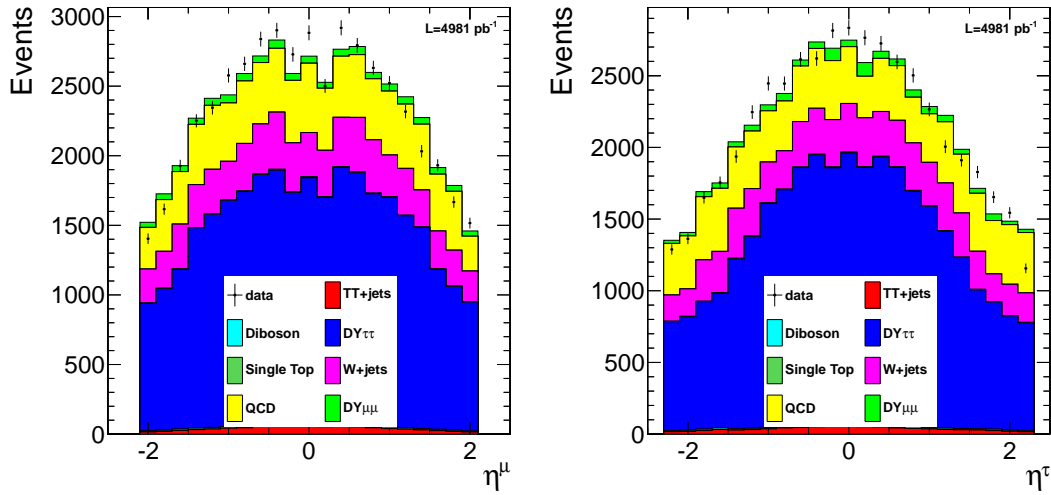


Figure 4.3.: Expected and observed distributions of reconstructed η muons (left) and τ_{had} (right) for non-VBF category.

Chapter 3). Three $\tau\tau$ decay modes are simulated - $\mu + \tau_{\text{had}}$, $\mu + e$ and $\mu + \mu$ (separately for every event). Other decay modes were found not to contribute to the background. Minimum visible p_T requirements (see Section 3.2.2) and branching ratios for simulated $\tau\tau$ decay modes are shown in Table 4.1.

To all events obtained with the embedding technique same series of cuts is applied as for the main analysis. The only exception is the trigger requirement, since the trigger decision is not available for the embedded events. For every event passing all of the cuts a weight is calculated, consisting of three factors:

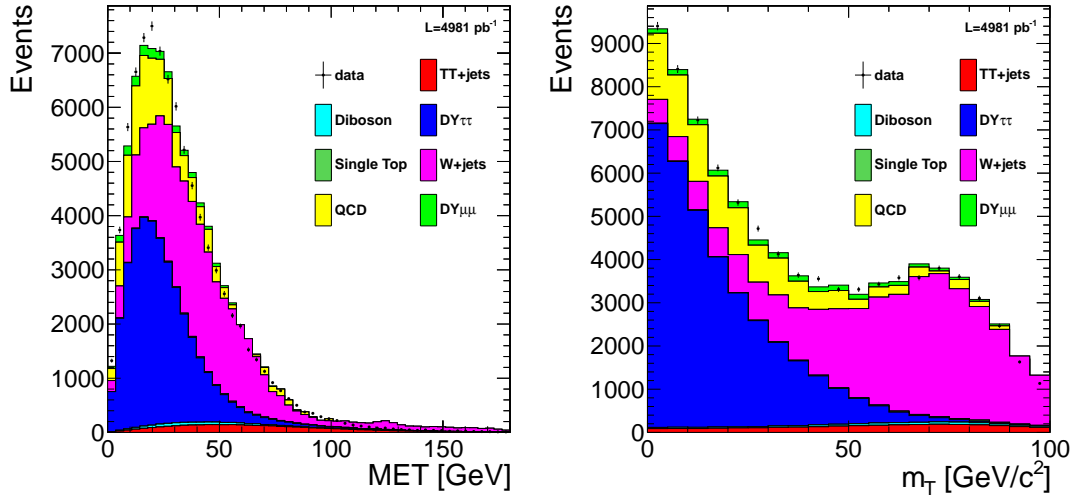


Figure 4.4.: Expected and observed distributions of missing transverse energy and transverse mass for non-VBF category (selection requirement on transverse mass was omitted).

Decay Mode	Minimum vis. p_T requirement (GeV/c)	Branching Ratio
$\mu + \tau_{\text{had}}$	$p_T^\mu > 13, p_T^{\tau_{\text{had}}} > 17$	0.2309
$\mu + e$	$p_T^{(1)} > 18, p_T^{(2)} > 8$	0.0621
$\mu + \mu$	$p_T^{\mu_1} > 18, p_T^{\mu_2} > 8$	0.0303

Table 4.1.: Minimum visible p_T requirements and branching ratios for samples obtained with the Particle Flow embedding technique for simulated $\tau\tau$ decay modes.

Weight due to minimum visible p_T requirement - embedded events are generated by requiring a visible p_T of τ decay products to be greater than a certain value (see Section 3.2.2). Therefore weighting is needed to obtain correct p_T spectrum both for reconstructed muons and τ_{had} .

Correction for the trigger efficiency - since the trigger requirement cannot be applied to the embedded event a weight is calculated depending on η and p_T of τ_{had} and muon pair. Trigger efficiency curves were obtained separately for τ_{had} and muon trigger constituents [55].

Correction for the DY $\mu\mu$ selection efficiency - correction is calculated using parametrization obtained using simulated DY $\mu\mu$ sample.

Last correction factor is determined in the same way as the $w_{\mu\mu}$ correction factor defined for the closure test described in Section 3.2.6. Data to MC corrections are applied in order to account for the observed differences in the trigger efficiency [57] and in muon reconstruction efficiencies [55].

Trigger modeling	6.3%
Data to MC corrections for trigger efficiency in DY $\mu\mu$ selection	2.1%
Closure test	1.4%
Muon efficiency corrections	1%
PDF uncertainty in DY $\mu\mu$ selection efficiency	0.9%
DY $\mu\mu$ background	0.6%
Total	7%

Table 4.2.: Summary of systematic uncertainties of the embedding method.

To estimate systematic error due to $\mu + \tau_{\text{had}}$ trigger efficiency modeling following procedure was applied. For every embedded event passing the selection criteria a ratio of expected trigger efficiency for recorded data and simulation was computed⁴. Difference between the average of obtained distribution and 1. was used as the systematic error measure. Obtained value was 6.3%.

Included data to MC corrections are considered as a systematic error of the event yield estimation method. Remaining uncertainty sources are due to PDF uncertainty in DY $\mu\mu$ selection efficiency estimation, difference observed in the closure test and expected DY $\mu\mu$ background (see Section 3.2.5). Systematic errors are summarized in Table 4.2.

4.2.3. Estimation of the QCD background

Second most dominant background source are QCD multijet events in which a muon is present and one of the jets is misidentified as the hadronic decay of τ lepton. This background is estimated by exploiting the fact, that in the QCD events the charge of muon and the charge reconstructed hadronic τ decay are expected to be not related, i.e. the ratio of number of same sign (SS) and opposite sign (OS) events should be close to one. Measured ratio in the LHC events [55] is

$$r^{\text{OS/SS}} = 1.11 \pm 0.02$$

In order to estimate QCD event yield all analysis selections are applied to LHC events with inverted requirement on sum of reconstructed μ and τ_{had} charges (sum of charges is required to be different from zero). From the obtained distribution contributions from DY

⁴Trigger efficiency curves (depending on η and transverse momenta of reconstructed muons and τ_{had}) from [55] were used.

$\tau\tau$, W+Jets and $\bar{t}t$ background processes are subtracted. Resulting distribution is scaled by the factor cited above.

4.2.4. Estimation of the W+Jets background

Events with a muon coming from the W boson decay and containing an additional jet misidentified as hadronic decay of τ . Estimation of this background is done by using a control region defined by $m_T > 60 \text{ GeV}/c^2$. Number of events from the control region is scaled by a factor

$$r^{(m_T < 40)/(m_T > 60)} = 0.297 \pm 0.019$$

after subtracting expected contributions from background $\bar{t}t$ and DY $\tau\tau$ processes. Event kinematics (e.g. shape of the visible mass distribution) are taken from MC simulation.

4.2.5. Estimation of other background sources

Remaining background sources include production of $\bar{t}t$ quark pair, single top quark and di-boson production. Their contribution is estimated using selection efficiency obtained from the simulated MC samples, along with measured (or predicted) cross section for $\sqrt{s} = 7 \text{ TeV}$ LHC energy and integrated luminosity measured by the CMS experiment [58].

The $\bar{t}t$ background is estimated by using a total inelastic cross section measurement by the CMS [59] ($165.8 \pm 13.3 \text{ pb}$).

In order to estimate the di-boson background a NLO cross sections determined by [60, 61] are used. Cross section values for WW, WZ and ZZ final states are 43.0 pb, 18.2 pb, 5.9 pb respectively. A 15% uncertainty is assigned to each of the values (which corresponds to the uncertainty of measured cross sections of these processes by the CMS experiment [62]).

The single top background is estimated by using production cross sections from [63], separately for s, t and tW production channels.

4.2.6. Signal estimation

Expected event yields corresponding to different Higgs boson masses (from 110 to 145 GeV/c^2 with mass points separated by 5 GeV/c^2) were obtained using simulated samples.

Two different samples were used corresponding to Gluon Fusion and Vector Boson Fusion production modes for every mass point. Another sample was used (also for each considered mass point) to obtain expected contribution for Associated Production with Heavy Quarks and Associated Production with Vector Bosons production modes. Cross-sections and branching ratios for Higgs boson were taken from [11] and [12].

4.3. Results

Obtained distributions of the reconstructed mass of the $\mu\tau_{\text{had}}$ pairs with all selection criteria applied are shown on Figures 4.5 and 4.6 respectively for the non-VBF and VBF categories. Mass is reconstructed using momenta of muon and τ_{had} . No correction is applied to account for neutrinos presence.

Uncertainty on the event yields and shapes due to scales uncertainties was evaluated. The event yield estimation procedure was repeated while varying variables used in the analysis (e.g. reconstructed muon momentum for simulated samples) up and down by their specific uncertainties. Official CMS scale uncertainty prescription was followed [64], with additional variation performed due to systematic uncertainties of the embedding method (see Section 3.2.5). Following variations are considered:

Mu - reconstructed muon momentum is varied by 0.2% up and down for every event for all simulated samples (including the embedded samples).

Tau - reconstructed τ_{had} momentum is varied by 3% up and down for every event. (including the embedded samples).

Jet - momenta of all jets with $p_{\text{T}} > 10 \text{ GeV}/c$ present in the event are varied by their momentum measurement uncertainty (depending on jet η and p_{T}).

SoftMET - unclustered deposits in calorimeters (deposits that aren't assigned to jets) and jets with transverse momentum smaller than $10 \text{ GeV}/c$ are added. The sum is varied by 10%.

Embedding - this variation is performed only for the embedded samples in order to account for the muon momentum scale uncertainties and higher radiation in underlying DY $\mu\mu$ events. Reconstructed momenta of τ_{had} and muons are additionally varied up by 1.1% and down by 0.5% (see Section 3.2.5). The later value includes only muon scale uncertainty. The former one includes additionally uncertainty due to the higher radiation.

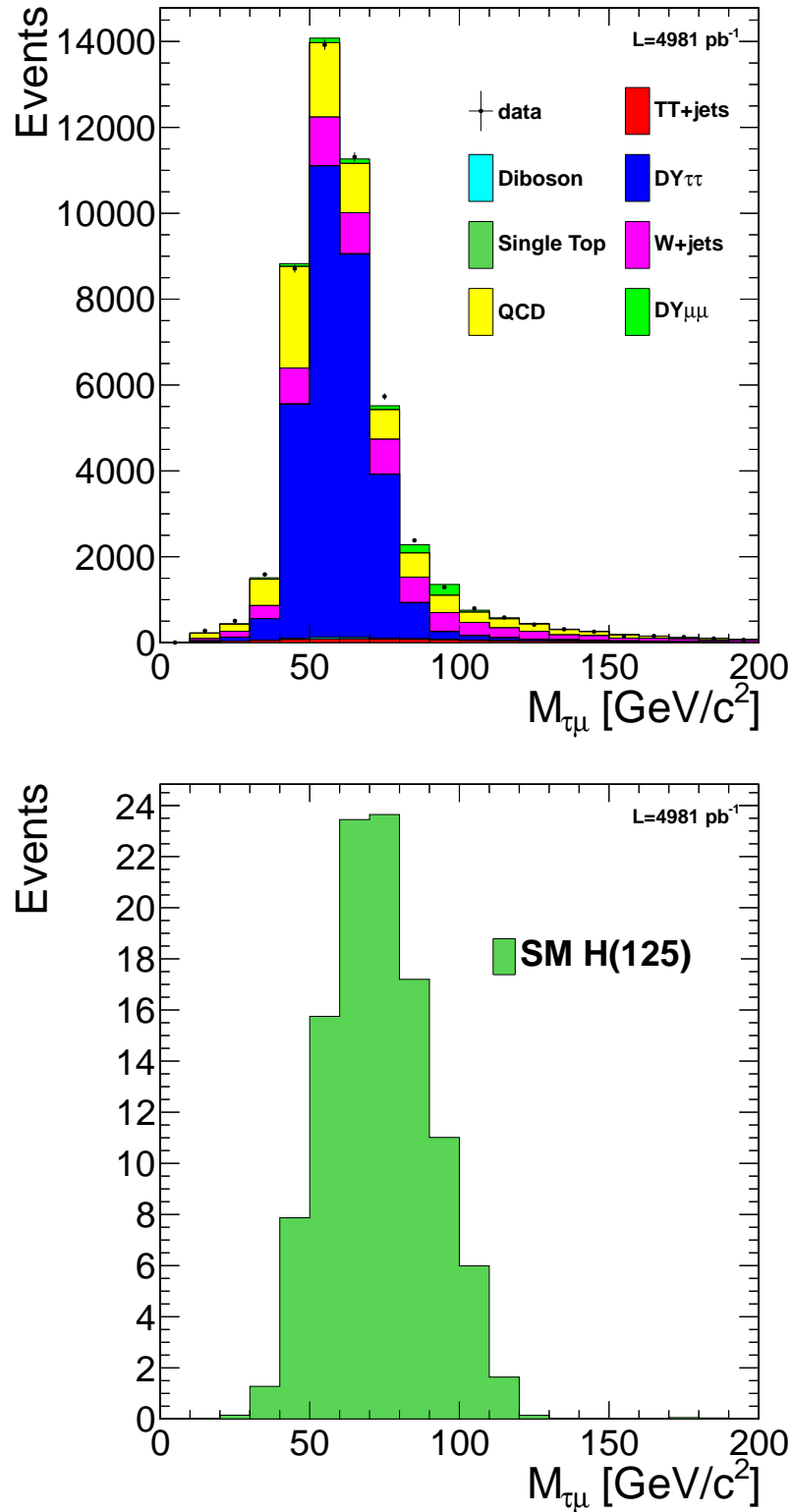


Figure 4.5.: Visible mass distributions of the $\mu - \tau_{\text{had}}$ pair for the non-VBF category. On top obtained distribution along with SM expectation (without signal). On bottom expected distribution for SM Higgs boson with 125 GeV/c^2 mass.

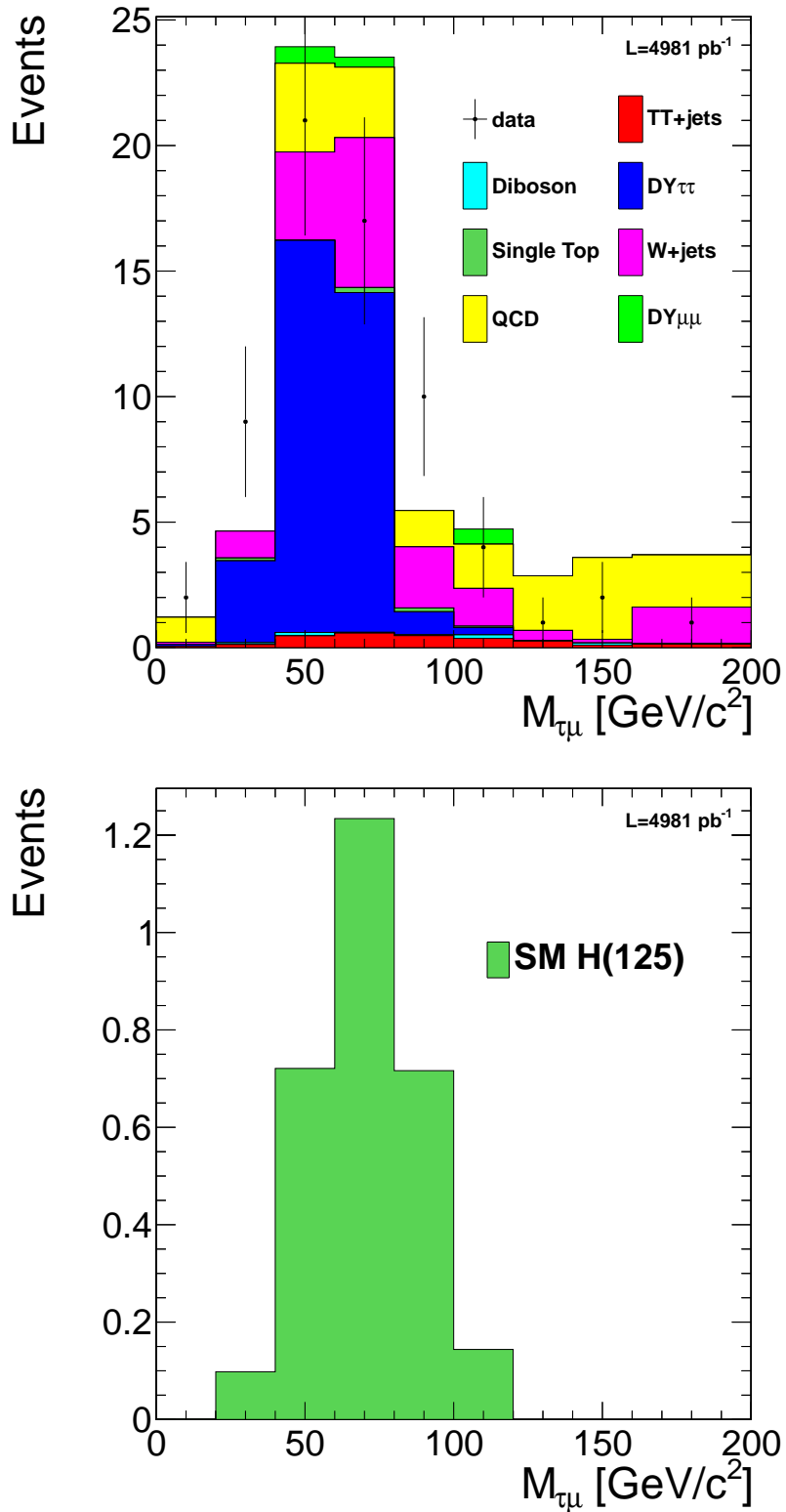


Figure 4.6.: Visible mass distributions of the $\mu - \tau_{\text{had}}$ pair for the VBF category. On top obtained distribution along with SM expectation (without signal). On bottom expected distribution for SM Higgs boson with $125 \text{ GeV}/c^2$ mass.

	Mu+	Mu-	Tau+	Tau-	softMET+	softMET-	Jet+	Jet-	Emb+	Emb-
DY $\tau\tau$	+0.27%	-0.29%	+1.40%	-1.95%	0.00%	0.00%	0.00%	0.00%	+2.12%	-1.00%
QCD	-0.04%	+0.05%	-0.37%	+0.47%	+0.06%	+0.06%	+0.14%	-0.01%	-0.12%	+0.07%
W + Jets	+0.01%	-0.00%	-0.65%	+0.69%	+0.02%	-0.04%	-0.03%	-0.02%	-0.12%	+0.06%
DY $\mu\mu$	+0.12%	-0.13%	+3.56%	-4.35%	-1.26%	-0.18%	-2.25%	+0.28%	0.00%	0.00%
TT + Jets	+0.14%	-0.16%	+2.07%	-2.48%	+0.98%	-0.99%	-0.65%	+0.58%	0.00%	0.00%
Diboson	+0.21%	-0.25%	+1.79%	-2.39%	+1.44%	-0.98%	+0.23%	+1.11%	0.00%	0.00%
SingleTop	+0.33%	-0.09%	+1.96%	-3.24%	+0.22%	-0.97%	-2.26%	+1.12%	0.00%	0.00%
SM ggH(125)	+0.03%	-0.22%	+1.14%	-1.28%	-0.57%	+0.36%	+0.19%	-0.85%	0.00%	0.00%
SM qqH(125)	+0.14%	-0.16%	+1.02%	-1.61%	-0.97%	+0.52%	-2.02%	+0.89%	0.00%	0.00%
SM VH(125)	+0.11%	-0.15%	+0.95%	-1.09%	+0.08%	-0.09%	+0.36%	-0.31%	0.00%	0.00%

Table 4.3.: Change in expected number of events after scale variations up (+) and down (-) for the non-VBF category.

After each variation transverse mass is recalculated for every event and all selection criteria are re-evaluated. Changes in obtained event yields (with respect to the central value) are shown in Table 4.3.

Obtained event yields in invariant mass bins along with their uncertainties are used to perform exclusion limit calculation on observed Higgs boson production cross section with respect to the one predicted by the Standard Model (referred to as signal strength modifier μ). The procedure described here is performed for every tested Higgs boson mass. A modified frequentist method (CLs) is used to calculate the limit [65]. A profile likelihood function used in the limit calculation is defined as

$$\mathcal{L}(\text{data}|\mu, \theta) = \text{Poisson}(\text{data}|\mu \cdot s(\theta) + b(\theta)) \cdot p(\theta|\tilde{\theta})$$

where θ represents a set of nuisance parameters (e.g. uncertainty on muon reconstruction efficiency), $s(\theta)$ and $b(\theta)$ are signal and background expectations, $p(\theta|\tilde{\theta})$ is a probability density function describing our knowledge on the nuisance parameters ($\tilde{\theta}$ is the average value).

The profile likelihood $\mathcal{L}(\text{data}|\mu, \theta)$ is used to find $\hat{\theta}_0^{obs}$ parameter. It describes the most probable nuisance parameters for the background only hypothesis ($\mu = 0$). A scan on the signal strength modifier μ is performed for every Higgs boson mass. For every tested value of the μ parameter a $\hat{\theta}_\mu^{obs}$ parameter is found using the same profile likelihood $\mathcal{L}(\text{data}|\mu, \theta)$. Parameter $\hat{\theta}_\mu^{obs}$ describes the best fit nuisance parameters for the signal+background hypothesis for given Higgs boson mass and for given μ parameter. A large number of a toy Monte Carlo experiments is generated separately for $\hat{\theta}_0^{obs}$ and $\hat{\theta}_\mu^{obs}$ parameters.

A test statistic \tilde{q}_μ is defined as the profile likelihood ratio:

$$\tilde{q}_\mu = -2\ln \frac{\mathcal{L}(\text{data}|\mu, \hat{\theta}_\mu)}{\mathcal{L}(\text{data}|\hat{\mu}, \hat{\theta})}$$

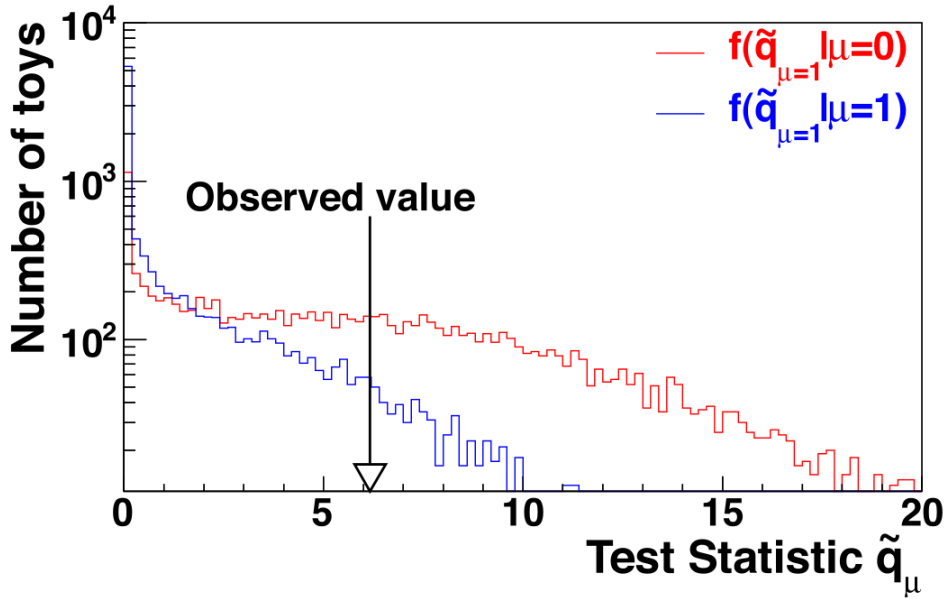


Figure 4.7.: Example test statistic distributions generated for the SM signal+background (with $\mu = 1$) and background-only hypotheses [65] for a particular Higgs boson mass.

where $\hat{\theta}_\mu$ is the best estimate of nuisance parameters for a given μ value, $\hat{\mu}$ and $\hat{\theta}$ values refer to global maximum of the likelihood and “data” can refer to actual experimental observation or to pseudo-data (toy Monte Carlo). Value of the $\hat{\mu}$ parameter is required to be greater than 0 and smaller than μ . With the above equation value $\tilde{q}_\mu^{\text{obs}}$ is calculated for obtained event yields.

For every toy Monte Carlo experiment value \tilde{q}_μ is calculated using the above equation. By this way probability density functions $f(\hat{q}_\mu|0, \hat{\theta}_0^{\text{obs}})$ and $f(\hat{q}_\mu|\mu, \hat{\theta}_\mu^{\text{obs}})$ are obtained for the background only hypothesis and for the SM signal+background hypothesis respectively.

As an example for the signal strength modifier $\mu = 1$ probability density functions $f(\hat{q}_{\mu=1}|0, \hat{\theta}_0^{\text{obs}})$ and $f(\hat{q}_{\mu=1}|1, \hat{\theta}_1^{\text{obs}})$ are shown on Figure 4.7.

For tested μ value a confidence level $\text{CL}_s(\mu)$ with which we exclude Higgs boson production with a cross section μ times higher than predicted by the Standard Model is defined as

$$\text{CL}_s(\mu) = \frac{\int_{\tilde{q}_\mu^{\text{obs}}}^{\infty} f(\hat{q}_\mu|\mu, \hat{\theta}_\mu^{\text{obs}}) d\hat{q}_\mu}{\int_{\tilde{q}_\mu^{\text{obs}}}^{\infty} f(\hat{q}_\mu|0, \hat{\theta}_0^{\text{obs}}) d\hat{q}_\mu}$$

In order to obtain 95% confidence level limit on μ value for given Higgs boson mass a scan is performed for different μ values until $\text{CL}_s(\mu) = 0.05$ condition is met.

Obtained and expected limits as a function of Higgs boson mass are shown in Figure 4.8. Obtained limit is consistent with the expected one.

Expected and obtained limits from the official CMS analysis [56] are shown in Figures 4.9 (separately for three different final states used) and 4.10 (combined limit for all considered final states). For Higgs boson masses up to $125 \text{ GeV}/c^2$ the expected limit obtained in this analysis is on a similar level when compared to the one obtained for the $\mu\tau_{\text{had}}$ final state in the official CMS analysis. This analysis has lower sensitivity when compared to the official CMS analysis, since same expected limit was obtained despite higher luminosity used (5 fb^{-1} vs 4.6 fb^{-1}). Analysis presented in this thesis is only a simplified version of the CMS analysis, performed in order to show application of the embedding method (see the outlined differences on the beginning of this chapter). A difference in the expected limit obtained in this analysis and the one from the official CMS analysis becomes visible for Higgs boson masses higher than $125 \text{ GeV}/c^2$. This is due to the use of the SVFit mass reconstruction algorithm in the official CMS analysis. The SVFit algorithm compensates for the lower number of the expected signal events by providing better signal separation from the DY $\tau\tau$ background.

In conclusion presented embedding method along with proposed normalization procedure (which is luminosity measurement independent) leads to a correct estimate of the DY $\tau\tau$ background in $H \rightarrow \tau\tau \rightarrow \mu\tau_{\text{had}}$ searches.

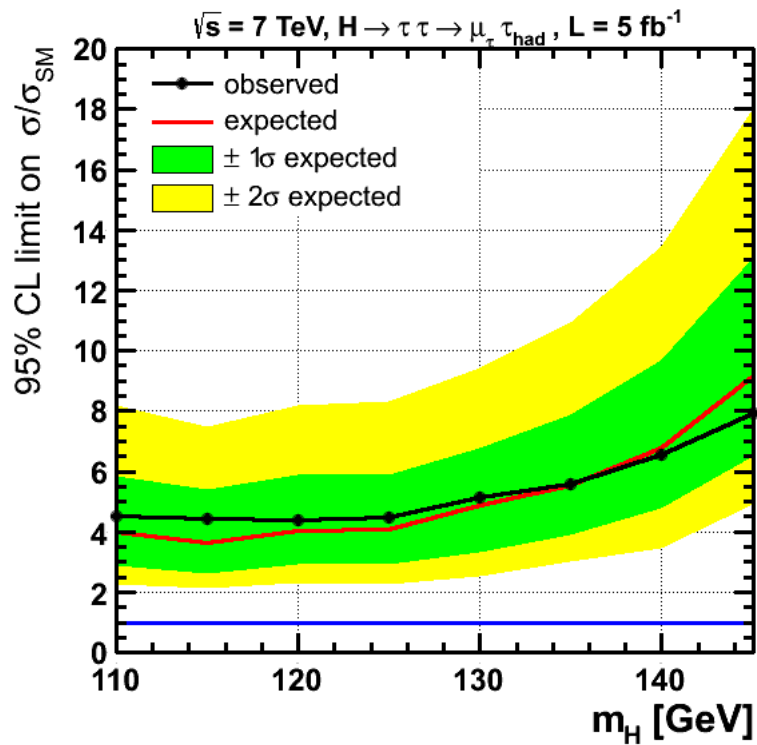


Figure 4.8.: This analysis - obtained 95% CL limit on the strength of an observed cross section over the expected cross section for a Standard Model Higgs boson as a function of its mass. Only $\mu\tau_{\text{had}}$ final state was considered. New method for DY $\tau\tau$ background estimation was used.

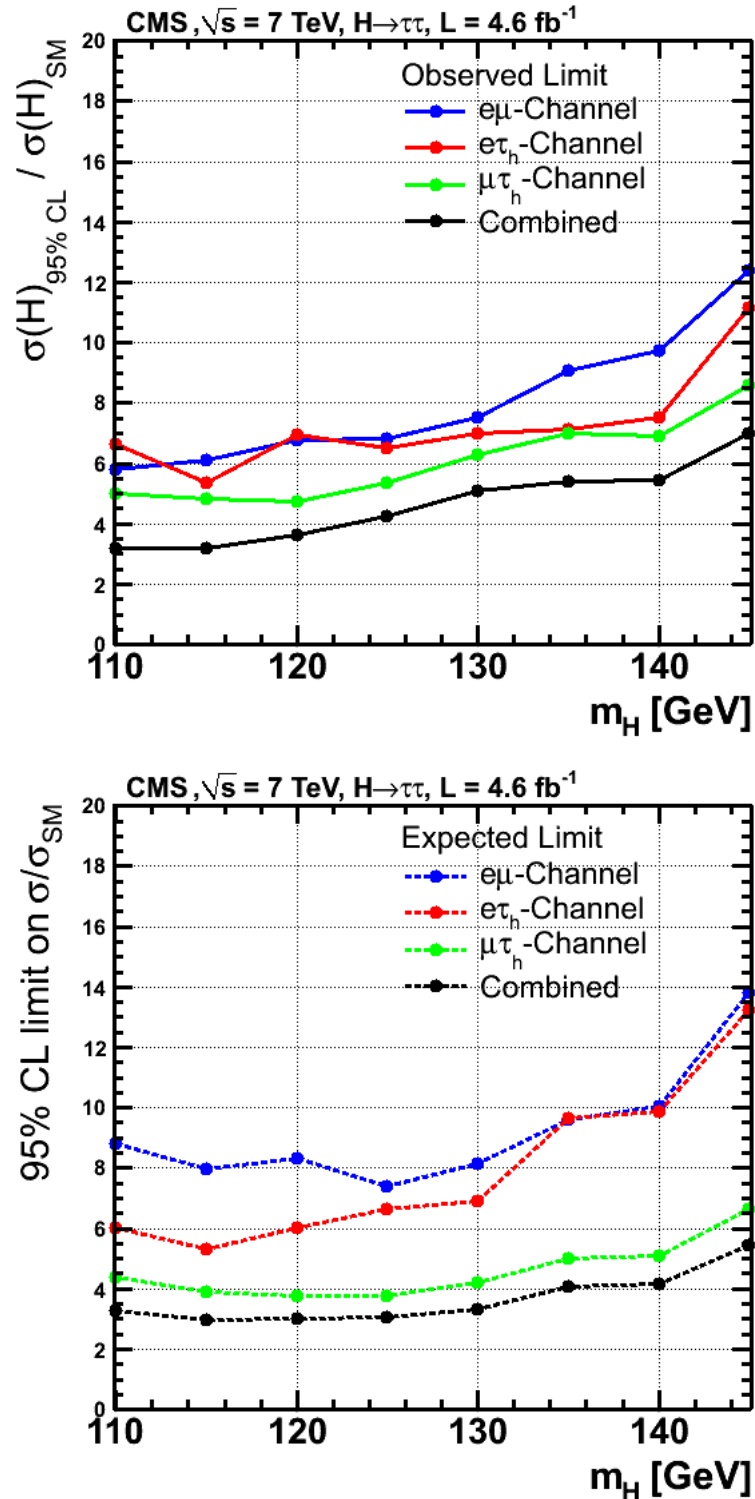


Figure 4.9.: The CMS public analysis [56] - observed and expected 95% CL limits on the strength of an observed cross section over the expected cross section for a Standard Model Higgs boson decaying to τ pairs as a function of its mass. Limits for all used final states are shown separately along with the combined limit.

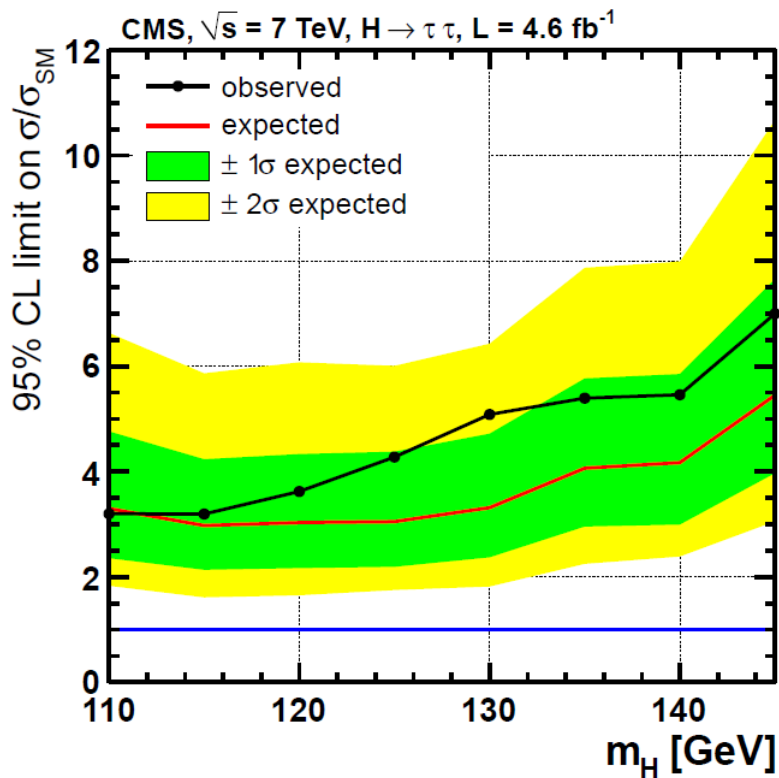


Figure 4.10.: The CMS public analysis [56] - 95% CL limit on the strength of an observed cross section over the expected cross section for a Standard Model Higgs boson decaying to τ pairs as a function of its mass. Combined limit along with one- and two-standard-deviations are shown.

Summary

The search for the Standard Model Higgs boson is performed in the $\tau\tau \rightarrow \mu + \tau_{jet}$ final state in the CMS experiment. Data corresponding to 5 fb^{-1} of integrated luminosity collected during 2011 was used for the search.

A new method of embedding of simulated τ decays in DY $\mu\mu$ events to estimate main irreducible background is proposed. In the method similarities between DY $\mu\mu$ and DY $\tau\tau$ processes are exploited in order to obtain a data driven estimate of DY $\tau\tau$ event yield. A detailed studies on method systematic uncertainties are presented along with event yield normalization procedure.

The Standard Model Higgs boson signal was not observed. For the amount of data used presented analysis is sensitive for cross sections from 4.5 to 8 times higher then the one predicted by the Standard Model. Therefore the Standard Model Higgs is not visible in this analysis.

Appendix A.

The Standard Model of particle physics

A.1. Quantum electrodynamics as an example of gauge theory

Lagrangian density for a free massive Dirac field Ψ is given by

$$\mathcal{L} = \bar{\Psi}(i\gamma^\mu\partial_\mu - m)\Psi$$

This density is invariant with respect to gauge transformation defined by

$$\Psi \rightarrow e^{-i\omega}\Psi$$

for any value of ω . A set of all numbers of a form $e^{-i\omega}$ (unitary matrices of dimension 1) is representation of group U(1).

In case of local (position dependent) transformation

$$\Psi \rightarrow e^{-i\omega(x)}\Psi$$

Lagrangian density is no longer invariant. After transformation Lagrangian changes by

$$\bar{\Psi}[\gamma^\mu(\partial_\mu\omega(x))]\Psi$$

Invariance with respect to local gauge transformations can be preserved, if field A_μ interacting with Dirac field is added to Lagrangian

$$\mathcal{L} = \bar{\Psi}(i\gamma^\mu (ieA_\mu + \partial_\mu) - m)\Psi - \frac{1}{4}F_{\mu\nu}F^{\mu\nu}$$

which transforms as

$$A_\mu \rightarrow A_\mu + \frac{1}{e}[\partial_\mu\omega(x)]$$

where e is electron charge and $F_{\mu\nu}$ is defined as

$$F_{\mu\nu} \equiv \partial_\mu A_\nu - \partial_\nu A_\mu$$

A_μ is so called gauge field.

A convenient way to write the above Lagrangian is to use covariant derivative, defined as

$$D_\mu = \partial_\mu + ieA_\mu$$

Lagrangian density can be written as

$$\mathcal{L} = \bar{\Psi}(i\gamma^\mu D_\mu - m)\Psi - \frac{1}{4}F_{\mu\nu}F^{\mu\nu}$$

It is worth noting, that requirement of local gauge invariance requires A_μ field being massless. Mass term $M_A^2 A_\mu A^\mu$ inside Lagrangian density leads to appearance of

$$\frac{2M_A^2}{e}A^\mu\partial_\mu\omega$$

term after transformation.

A.1.1. Gauge theories with massive interaction carriers

In Nature, apart from interaction with massless carriers (electromagnetic interaction, carried by photons), interactions exist with massive carriers (weak interaction, carried by massive bosons W and Z). Since Lagrangian density cannot include mass terms for gauge fields, a special mechanism is exploited to give gauge bosons a mass. This is so called Higgs mechanism.

Consider the Lagrangian density written before with a new complex scalar field added:

$$\mathcal{L} = \bar{\Psi}(i\gamma^\mu D_\mu - m)\Psi - \frac{1}{4}F_{\mu\nu}F^{\mu\nu} + (D_\mu\Phi)^\dagger(D^\mu\Phi) - V(\Phi)$$

where

$$V(\Phi) = -\mu^2\Phi^\dagger\Phi + \lambda|\Phi^\dagger\Phi|^2; \quad \mu^2 > 0, \lambda > 0$$

$$D_\mu\Phi = (\partial_\mu + igA_\mu)\Phi$$

Above Lagrangian is invariant with respect to local gauge transformation:

$$\Phi \rightarrow e^{i\omega(x)}\Phi$$

Potential V has a minimum for a continuum of values

$$\Phi_{min} = e^{i\Theta} \sqrt{\frac{\mu^2}{2\lambda}}; \quad \Theta \in [0, 2\pi]$$

After selecting one of minimum states

$$v = \sqrt{\frac{\mu^2}{\lambda}}$$

and promoting it to a role of a ground state, Φ field can be written as

$$\Phi = \frac{1}{\sqrt{2}}(v + H + i\phi)$$

Potential V takes the form

$$V = -\frac{\mu^4}{4\lambda} + \mu^2 H^2 + O(H^3)$$

The H field is a massive field (due to $\mu^2 H^2$ term). Terms $O(3)$ describe trilinear and quartic self interaction of H field.

Inserting the expression for Φ into term $(D_\mu\Phi)^\dagger(D^\mu\Phi)$ leads to

$$\begin{aligned} (D_\mu\Phi)^\dagger(D^\mu\Phi) &= \frac{1}{2}\partial_\mu H\partial^\mu H + \frac{1}{2}\partial_\mu\phi\partial^\mu\phi + \frac{1}{2}g^2v^2A_\mu A^\mu + \frac{1}{2}g^2A_\mu A^\mu(H^2 + \phi^2) \\ &\quad - gA_\mu(\phi\partial^\mu H - H\partial^\mu\phi) + gvA_\mu\partial^\mu\phi + g^2vA_\mu A^\mu H \end{aligned}$$

Field A has acquired mass ($M_A = gv$) due to term $\frac{1}{2}g^2v^2A_\mu A^\mu$.

In the above expression terms coupling fields A and H have appeared:

$$g^2A_\mu A^\mu H^2 = \frac{g}{v}M_A A_\mu A^\mu H^2$$

$$g^2vA_\mu A^\mu H = vM_A A_\mu A^\mu H$$

From above terms it can be seen, that interaction strength is proportional to the mass of field A .

Field A mixes with field ϕ ($M_A A_\mu \partial^\mu \phi$ term), which can be interpreted as longitudinal degree of freedom of field A , due to it's non-zero mass.

Method described above of giving gauge bosons a mass is called a Higgs mechanism. Since a new field H is introduced in the Lagrangian, a new particle, called Higgs boson appears in the particle spectrum. From ϕ field an unphysical boson appears, so called Goldstone boson (which becomes a longitudinal component of A field).

A.2. The Standard Model of electroweak interactions

Prescription described above for building a model with massive gauge bosons consists of following steps:

1. Selection of Lagrangian symmetry group
2. Replacement of a derivative ∂_μ with covariant derivative D_μ , in which interaction with vector fields is present.
3. Supplement the Lagrangian with kinetic terms of vector fields
4. Make selected vector fields massive using Higgs mechanism.

The underlying symmetry group of the Standard Model is

$$U_Y(1) \times SU_L(2) \times SU_C(3)$$

Described above prescription is complicated by a fact, that weak interactions appear only for a left handed fermions (which is emphasized by a "L" index). Mass term for a fermion field

$$m \bar{\Psi} \Psi = m(\bar{\Psi}_L \Psi_R + \bar{\Psi}_R \Psi_L)$$

"mixes" left and right handed states, such terms are forbidden in the Lagrangian, since they break gauge invariance ($SU_L(2)$ gauge transformation acts only on left handed component). Therefore fermion masses must also arise from the Higgs mechanism.

With $SU_L(2)$ group there are three fields $W_\mu^a, a = 1, 2, 3$ associated.

	ν_L	l_L	l_R	q_{UL}	q_{DL}	q_{UR}	q_{DR}
I_3	$\frac{1}{2}$	$-\frac{1}{2}$	0	$\frac{1}{2}$	$-\frac{1}{2}$	0	0
Y	-1	-1	-2	$\frac{1}{3}$	$\frac{1}{3}$	$\frac{4}{3}$	$-\frac{2}{3}$

Table A.1.: Isospin and hypercharge of the Standard Model particle content. l stands for any lepton, ν for any neutrino, q_U and q_D for any of upper and lower quarks.

With group $U_Y(1)$ field B_μ is associated. It is worth noting, that group $U_Y(1)$ is not the symmetry group of electromagnetism, since it couples to a hypercharge Y and not to the electromagnetic charge. Another important thing worth noting is that fields B_μ, W_μ^a are not “physical” fields - only its linear combination will lead to fields related to a photon and W^\pm, Z^0 bosons.

Group $SU_C(3)$ is related to a strong interactions. There are 8 interaction carriers associated with it, called gluons. For clarity reasons description of the Standard Model given below will be limited to electroweak interactions. Complete description, including also the strong interactions can be found in [1]. Therefore it will be shown, how $U_Y(1) \times SU_L(2)$ symmetry group is broken to $U_{em}(1)$ group (related to electromagnetic interaction), giving W and Z boson their mass.

Fermions included in Standard Model can be grouped into left handed doublets and right handed singlets with respect to $U_Y(1) \times SU_L(2)$ ¹:

$$\begin{pmatrix} \nu_e \\ e \end{pmatrix}_L \quad \begin{pmatrix} \nu_\mu \\ \mu \end{pmatrix}_L \quad \begin{pmatrix} \nu_\tau \\ \tau \end{pmatrix}_L \quad e_R \quad \mu_R \quad \tau_R$$

$$\begin{pmatrix} u \\ d \end{pmatrix}_L \quad \begin{pmatrix} c \\ s \end{pmatrix}_L \quad \begin{pmatrix} t \\ b \end{pmatrix}_L \quad u_R \quad d_R \quad c_R \quad s_R \quad t_R \quad b_R$$

Particle from above list can be characterized by a hypercharge Y and weak isospin Y_3 values (Table A.1), which are related to the electric charge by

$$Q = I_3 + \frac{Y}{2}$$

¹In fermion list right handed neutrinos are omitted, since not crucial for derivation.

Group $U_Y(1) \times SU_L(2)$ has 4 generators

$$T_a = I_a \quad (a = 1, 2, 3), \quad T_4 = Y$$

where I_a are isospin operators and Y is hypercharge operator. The above generators obey the relation

$$[I_a, I_b] = i\epsilon_{abc}I_c, \quad [I_a, Y] = 0$$

A lagrangian for the given fermion spectrum and $U_Y(1) \times SU_L(2)$ symmetry group can be written as:

$$\mathcal{L} = \mathcal{L}_{Gauge} + \mathcal{L}_{Higgs} + \mathcal{L}_{Fermions} + \mathcal{L}_{Yukawa}$$

Term \mathcal{L}_{Gauge} includes kinetic terms of gauge fields, defined using field strength tensors:

$$W_{\mu\nu}^a = \partial_\mu W_\nu^a - \partial_\nu W_\mu^a + g_2\epsilon_{abc}W_\mu^b W_\nu^c$$

$$B_{\mu\nu} = \partial_\mu B_\nu - \partial_\nu B_\mu$$

The coupling strengths of fields $B_{\mu\nu}$ and $W_{\mu\nu}^a$ to fermion fields is given by gauge coupling constants g_1 and g_2 . Since the lagrangian density for vector fields cannot include mass terms, lagrangian density \mathcal{L}_{Gauge} takes form

$$\mathcal{L}_{Gauge} = -\frac{1}{4}W_{\mu\nu}^a W^{a,\mu\nu} - \frac{1}{4}B_{\mu\nu}B^{\mu\nu}$$

Part \mathcal{L}_{Higgs} defines, how the Higgs field

$$\Phi = \begin{pmatrix} \phi^\dagger \\ \phi^0 \end{pmatrix}$$

(isospin doublet for complex scalar fields) couples to fields B and W^a :

$$\mathcal{L}_{Higgs} = (D_\mu\Phi)^\dagger(D^\mu\Phi) - V(\Phi)$$

where

$$V(\Phi) = -\mu^2\Phi^\dagger\Phi + \lambda(\Phi^\dagger\Phi)^2$$

and the covariant derivative is defined as

$$D_\mu = \partial_\mu - ig_2\frac{\sigma_a}{2}W_\mu^a + i\frac{g_1}{2}B_\mu$$

For $\mu^2, \lambda > 0$ potential V has a continuum of minima for $\Phi^\dagger\Phi = \frac{2\mu^2}{\lambda}$. It is worth noting, that one of the minima

$$\langle \Phi \rangle = \frac{1}{\sqrt{2}} \begin{pmatrix} 0 \\ v \end{pmatrix} \quad v = \frac{\mu}{\sqrt{\lambda}}$$

has a zero charge:

$$Q \langle \Phi \rangle = (I_3 + \frac{Y}{2}) \langle \Phi \rangle = \begin{pmatrix} 1 & 0 \\ 0 & 0 \end{pmatrix} \langle \Phi \rangle = 0$$

Around this value field Φ can be expanded:

$$\Phi = \begin{pmatrix} \phi^\dagger \\ (v + H + i\chi)/\sqrt{2} \end{pmatrix}$$

It is possible to choose a specific gauge in a such way, that fields ϕ^\dagger and χ disappear. In this gauge:

$$\Phi = \frac{1}{\sqrt{2}} \begin{pmatrix} 0 \\ v + H \end{pmatrix}$$

Which leads to

$$V(\Psi) = \mu^2 H^2 + \lambda v H^3 + \frac{\lambda}{4} H^4$$

From the above equation mass of a boson related to field H can be read:

$$M_H = \mu\sqrt{2}$$

Terms proportional to H^3 i H^4 describe trilinear and quadrilinear selfinteraction vertices of the Higgs field.

In kinetic part $((D_\mu\Phi)^\dagger(D^\mu\Phi))$ of Lagrangian density \mathcal{L}_{Higgs} one finds terms

$$\frac{1}{2}(\frac{g_2}{2}v)^2((W^1)^2 + (W^2)^2) + \frac{1}{2}(\frac{v}{2})^2 \begin{pmatrix} W_\mu^3 & B_\mu \end{pmatrix} \begin{pmatrix} g_2^2 & g_1 g_2 \\ g_1 g_2 & g_1^2 \end{pmatrix} \begin{pmatrix} W^{3,\mu} \\ B^\mu \end{pmatrix}$$

which can be rewritten using physical fields

$$W_\mu^\pm = \frac{1}{\sqrt{2}}(W_\mu^1 \mp iW_\mu^2)$$

$$\begin{pmatrix} Z_\mu \\ A_\mu \end{pmatrix} = \begin{pmatrix} \cos\theta_W & \sin\theta_W \\ -\sin\theta_W & \cos\theta_W \end{pmatrix} \begin{pmatrix} W_\mu^3 \\ B_\mu \end{pmatrix}, \quad \cos\theta_W = \frac{g_2}{\sqrt{g_1^2 + g_2^2}}$$

Above terms are interpreted as mass terms for new fields W^\pm , Z , while A field is massless:

$$M_W^2 W_\mu^\dagger W^{-\mu} + \frac{1}{2} \begin{pmatrix} A_\mu & Z_\mu \end{pmatrix} \begin{pmatrix} 0 & 0 \\ 0 & M_Z^2 \end{pmatrix} \begin{pmatrix} A^\mu \\ Z^\mu \end{pmatrix}$$

where

$$M_W = \frac{1}{2} g_2 v, \quad M_Z = \frac{1}{2} \sqrt{g_1^2 + g_2^2} v$$

Fields W^\pm , Z are related to W and Z bosons, field A to a photon field.

Lagrangian part $\mathcal{L}_{\text{Fermions}}$ contains kinetic terms for fermion fields. By defining

$$(\Psi_L^{\text{quark}})^j = \left(\begin{pmatrix} u \\ d \end{pmatrix}_L, \begin{pmatrix} c \\ s \end{pmatrix}_L, \begin{pmatrix} t \\ b \end{pmatrix}_L \right)^j$$

$$(\Psi_L^{\text{lepton}})^j = \left(\begin{pmatrix} \nu_e \\ e \end{pmatrix}_L, \begin{pmatrix} \nu_\mu \\ \mu \end{pmatrix}_L, \begin{pmatrix} \nu_\tau \\ \tau \end{pmatrix}_L \right)^j$$

$$(\Psi_{R,\text{up}}^{\text{quark}})^j = (u_R, c_R, t_R)^j, \quad (\Psi_{R,\text{down}}^{\text{quark}})^j = (d_R, s_R, b_R)^j$$

$$(\Psi_R^{\text{lepton}})^j = (e_R, \mu_R, \tau_R)^j$$

part $\mathcal{L}_{\text{Fermions}}$ can be written as

$$\begin{aligned} \mathcal{L}_{\text{Fermions}} &= \sum_j (\bar{\Psi}_L^{j,\text{quark}} i \not{D}^L \Psi_L^{j,\text{quark}} + \bar{\Psi}_L^{j,\text{lepton}} i \not{D}^L \Psi_L^{j,\text{lepton}}) \\ &+ \sum_{j,\sigma=\text{up,down}} (\bar{\Psi}_{R,\sigma}^{j,\text{quark}} i \not{D}^R \Psi_{R,\sigma}^{j,\text{quark}} + \bar{\Psi}_{R,\sigma}^{j,\text{lepton}} i \not{D}^R \Psi_{R,\sigma}^{j,\text{lepton}}) \end{aligned}$$

where covariant derivative is defined as

$$D_\mu^{L,R} = \partial_\mu - i g_2 I_a^{R,L} W_\mu^a + i g_1 \frac{Y}{2} B_\mu, \quad I_a^L = \frac{1}{2} \sigma_a, \quad I_a^R = 0$$

(σ_a are Pauli matrices).

As it was shown above, Lagrangian density cannot include mass terms for fermion fields, since they break gauge invariance. To give fermion masses the Higgs field is once again used. Part \mathcal{L}_{Yukawa} includes coupling of fermion fields to Higgs field via Yukawa interaction:

$$\begin{aligned} \mathcal{L}_{Yukawa} = & -\delta_{ij} G_{ij}^l \left(\overline{\Psi}_L^{lepton} \right)^i \Phi \left(\Psi_R^{lepton} \right)^j + \\ & - G_{ij}^d \left(\overline{\Psi}_L^{quark} \right)^i \Phi \left(\Psi_{R,down}^{quark} \right)^j - G_{ij}^u \left(\overline{\Psi}_L^{quark} \right)^i \Phi^c \left(\Psi_{R,up}^{quark} \right)^j + h.c. \end{aligned}$$

where Φ^c is charge-conjugate of field Φ , matrices G define coupling strengths.

The above equation can be rewritten in a following way:

$$\mathcal{L}_{Yukawa} = -\delta_{ij} G_{ij}^l (\overline{\nu}_L^i, \overline{l}_L^i) \Phi l_R^j - G_{ij}^d (\overline{u}_L^i, \overline{d}_L^i) \Phi d_R^j - G_{ij}^u (\overline{u}_L^i, \overline{d}_L^i) \Phi^c u_R^j + h.c.$$

Here u^i corresponds to different up-type quarks (u, c, t), d^i to down-type quarks (d, s, b), l^i and ν^i to different lepton and neutrino flavors. After substituting Φ with its expansion

$$\frac{1}{\sqrt{2}} \begin{pmatrix} 0 \\ v + H \end{pmatrix}$$

inside \mathcal{L}_{Yukawa} following terms for quarks can be found:

$$\mathcal{L}_{Yukawa}^{quarks} = -\frac{v}{\sqrt{2}} G_{ij}^d \overline{d}_L^i d_R^j - \frac{v}{\sqrt{2}} G_{ij}^u \overline{u}_L^i u_R^j + h.c. + \text{interaction terms}$$

Lagrangian part $\mathcal{L}_{Yukawa}^{quarks}$ can be diagonalized using unitary matrices $V_{L,R}^q$ ($q = u, d$):

$$\tilde{u}_{L,R}^i = (V_{L,R}^u)_{ik} u_{L,R}^k, \quad \tilde{d}_{L,R}^i = (V_{L,R}^d)_{ik} d_{L,R}^k$$

which along with coupling strength matrices G define quark masses:

$$M_{diag}^q = \frac{v}{\sqrt{2}} V_L^q G_q V_R^{q\dagger}, \quad q = u, d$$

Appendix B.

Estimation of hadronic τ tag efficiency using $Z \rightarrow \tau\tau \rightarrow \mu\tau_{had}$ to $Z \rightarrow \mu\mu$ events ratio

In this appendix a method used to estimate an efficiency of τ_{had} identification is described¹. The τ identification is defined as a product of tau decay mode reconstruction and isolation of the reconstructed decay mode (HPS loose isolation). The method explores ratio between number of observed $Z \rightarrow \mu\mu$ to $Z \rightarrow \tau\tau \rightarrow \tau_\mu\tau_{had}$ events. Number of measured $Z \rightarrow \mu\mu$ events ($N_{Z \rightarrow \mu\mu}$) can be expressed as follows:

$$N_{Z \rightarrow \mu\mu} = \sigma_Z \times BR(Z \rightarrow \mu\mu) \times \mathcal{L} \times \epsilon_{trig_{\mu\mu}} \times \epsilon_{off_{\mu\mu}} \times \epsilon_{acc_{\mu\mu}} = N_{\mu\mu}^{meas} - N_{\mu\mu}^{bkg}$$

where $\sigma_Z \times BR(Z \rightarrow \mu\mu)$ is the product of the Z production cross-section and $Z \rightarrow \mu\mu$ branching ratio, \mathcal{L} is an integrated luminosity, $\epsilon_{trig_{\mu\mu}}$ is a trigger efficiency, $\epsilon_{off_{\mu\mu}}$ is an efficiency of offline selection, $\epsilon_{acc_{\mu\mu}}$ is kinematic acceptance calculated on generator basis and $N_{\mu\mu}^{meas} - N_{\mu\mu}^{bkg}$ number of measured $\mu\mu$ events minus expected background.

Similarly, number of $Z \rightarrow \tau\tau \rightarrow \tau_\mu\tau_{had}$ events ($N_{Z \rightarrow \tau_\mu\tau_{had}}$) can be expressed as:

$$N_{Z \rightarrow \tau_\mu\tau_{had}} = \sigma_Z \times BR(Z \rightarrow \tau\tau \rightarrow \tau_\mu\tau_{had}) \times \mathcal{L} \times \epsilon_{M_T} \times \epsilon_{other} \times \epsilon_{\tau-Id} \times \epsilon_{trig_{\mu\tau}} = N_{\mu\tau}^{meas} - N_{\mu\tau}^{bkg}$$

¹This study was a part of [67]. A naming convention from the cited note is followed. The $Z \rightarrow \mu\mu$ and $Z \rightarrow \tau\tau$ processes stand for the Drell-Yan process.

where $\epsilon_{\tau-Id}$ stands for an efficiency of τ identification, ϵ_{M_T} is efficiency on transverse mass cut and ϵ_{other} is a product of kinematic acceptance and an efficiency of offline selection excluding τ -Id and transverse mass cut. $\epsilon_{trig_{\mu\tau}}$ is trigger efficiency calculated with respect to all other cuts.

Finally, by combining two above expressions one can write the following formula for the τ identification efficiency:

$$\epsilon_{\tau-Id} = \frac{N_{\mu\tau}^{meas} - N_{\mu\tau}^{bkg}}{N_{\mu\mu}^{meas} - N_{\mu\mu}^{bkg}} \times \frac{BR(Z \rightarrow \mu\mu)}{BR(Z \rightarrow \tau\tau \rightarrow \tau_{\mu}\tau_{had})} \times \frac{\epsilon_{trig_{\mu\mu}}}{\epsilon_{trig_{\mu\tau}}} \times \frac{\epsilon_{off_{\mu\mu}} \times \epsilon_{acc_{\mu\mu}}}{\epsilon_{M_T} \times \epsilon_{other}}$$

Numerical results corresponding to the $Z \rightarrow \mu\mu$ selection are taken from the Z boson production study with 36.2 pb^{-1} ([68]). In the above analysis the trigger and offline selection efficiency and their uncertainties are obtained simultaneously by fit of signal+background mass templates to data. The result of the fit procedure is quoted here as one number $N_{Z \rightarrow \mu\mu}^{yield}$ which stands for the $Z \rightarrow \mu\mu$ event yield corrected for trigger and offline selection efficiencies:

$$N_{Z \rightarrow \mu\mu}^{yield} = (N_{\mu\mu}^{meas} - N_{\mu\mu}^{bkg}) \times \frac{1}{\epsilon_{trig_{\mu\mu}}} \times \frac{1}{\epsilon_{off_{\mu\mu}}}$$

Cross section measurement done in ([68]) is performed for invariant mass of two muons in range from 60 to 120 GeV/c^2 . Since there is no compatible selection requirement present in $Z \rightarrow \tau\tau \rightarrow \tau_{\mu}\tau_{had}$ analysis, generator level kinematic acceptance $\epsilon_{acc_{\mu\mu}}$ was recalculated while applying only muon p_T and η requirements, while requiring invariant mass of two muons to be greater than 20 GeV/c^2 . The invariant mass requirement matches generator level requirement present in DY $\tau\tau$ Monte Carlo simulation used for selection efficiency estimation.

The measurement of $Z \rightarrow \tau\tau \rightarrow \tau_{\mu}\tau_{had}$ number of events as well as data-driven background estimate and trigger efficiency for the $Z \rightarrow \tau\tau \rightarrow \tau_{\mu}\tau_{had}$ is the same as described in [66]. Selection efficiency of the $Z \rightarrow \tau\tau \rightarrow \tau_{\mu}\tau_{had}$ offline m_T kinematic cut is estimated using the tau-embedded sample, while selection efficiency ϵ_{other} is estimated from the Monte Carlo simulation. Numerical values of all terms are summarized in Table B.1.

The relative uncertainty of the evaluation of $\epsilon_{\tau-Id}$ can be expressed in terms of relative uncertainties on the extracted number of $Z \rightarrow \mu\mu$ events (statistical and systematic),

$N_{Z \rightarrow \mu\mu}^{yield}$	13724
$\epsilon_{acc\mu\mu}$	0.2162
$N_{\mu\tau}^{meas} - N_{\mu\tau}^{bkg}$	306
$\epsilon_{trig\mu\tau}$	0.924
ϵ_{M_T}	0.9473
ϵ_{other}	0.0510
$\frac{BR(Z \rightarrow \mu\mu)}{BR(Z \rightarrow \tau\tau \rightarrow \mu\tau)}$	$\frac{1}{0.22495}$
$\epsilon_{\tau-Id}$	0.476

Table B.1.: Values of terms in expression used to evaluate τ identification efficiency.

number of events passing the $Z \rightarrow \tau\tau \rightarrow \tau_\mu\tau_{had}$ selections, estimated number of background events, and finally trigger and offline selection efficiencies in following way:

$$\begin{aligned}
 \frac{\Delta\epsilon_{\tau-Id}}{\epsilon_{\tau-Id}} = & \underbrace{\frac{\Delta N_{Z \rightarrow \mu\mu}^{yield, stat}}{N_{Z \rightarrow \mu\mu}^{yield}}}_{\mu\mu \text{ stat.}} \oplus \underbrace{\frac{\Delta N_{Z \rightarrow \mu\mu}^{yield, sys}}{N_{Z \rightarrow \mu\mu}^{yield}}}_{\mu\mu \text{ sys.}} \oplus \underbrace{\frac{\Delta(N_{\mu\tau}^{meas} - N_{\mu\tau}^{bkg})}{N_{\mu\tau}^{meas} - N_{\mu\tau}^{bkg}}}_{\mu\tau \text{ stat.}} \oplus \\
 & \underbrace{\frac{\Delta\epsilon_{trig\mu\tau}}{\epsilon_{trig\mu\tau}}}_{\epsilon_{trig\mu\tau} \text{ sys.}} \oplus \underbrace{\frac{\Delta\epsilon_{M_T}}{\epsilon_{M_T}}}_{\epsilon_{M_T} \text{ sys.}} \oplus \underbrace{\frac{\Delta\epsilon_{other}}{\epsilon_{other}}}_{\epsilon_{other} \text{ sys.}}
 \end{aligned}$$

The ratio of of branching fractions $BR(Z \rightarrow \mu\mu)/BR(Z \rightarrow \tau\tau \rightarrow \tau_\mu\tau_{had})$ has small uncertainty of $\mathcal{O}(10^{-3})$ which is negligible compared with other uncertainties, thus neglected.

As an estimate of systematic error of trigger efficiency ($\Delta\epsilon_{trig\mu\tau}$) value $|1 - X_{corr}^{trg}|$ is taken, where X_{corr}^{trg} is data to Monte Carlo correction factor for trigger efficiency.

Systematic error estimate for $N_{Z \rightarrow \mu\mu}^{yield, sys}$ measurement was recalculated excluding a PDF uncertainty. The PDF uncertainty is small and can be neglected, when ratio of acceptances for $Z \rightarrow \mu\mu$ and $Z \rightarrow \tau\tau \rightarrow \tau_\mu\tau_{had}$ is considered. To check it, acceptances of $Z \rightarrow \mu\mu$ ($A_{Z \rightarrow \mu\mu}$), $Z \rightarrow \tau\tau \rightarrow \tau_\mu\tau_{had}$ ($A_{Z \rightarrow \tau\mu\tau_{had}}$) and their ratio ($\frac{A_{Z \rightarrow \mu\mu}}{A_{Z \rightarrow \tau\mu\tau_{had}}}$) was calculated separately for each of 41 PDF sets (central value set and 40 error sets) provided in the CTEQ66 library. Half of difference between the smallest and the biggest of calculated values was taken as a PDF uncertainty estimate separately for $A_{Z \rightarrow \mu\mu}$, $A_{Z \rightarrow \tau\mu\tau_{had}}$ and $\frac{A_{Z \rightarrow \mu\mu}}{A_{Z \rightarrow \tau\mu\tau_{had}}}$. Relative error on the above values is 0.9%, 0.8% and 0.09%, respectively.

As an estimate of systematic error of transverse mass cut a difference between cut efficiency for embedded sample and DY $\tau\tau$ Monte Carlo simulation was taken. An

uncertainty due to muon and tau-jet energy scale was also considered. Transverse mass was recalculated while varying up and down muon and tau-jet transverse momentum by 1% and 3%, respectively and then transverse mass cut efficiency was reevaluated using the new value of M_T . The biggest difference between the central value and varied values was taken as uncertainty. Muon and tau-jet scale uncertainty is also the main source of the ϵ_{other} uncertainty. Therefore, it is given together for both the ϵ_{other} and the ϵ_{M_T} cuts.

Uncertainty values of components of $\epsilon_{\tau-Id}$ are summarized in Table B.2.

$\frac{\Delta N_{Z \rightarrow \mu\mu}^{yield, stat}}{N_{Z \rightarrow \mu\mu}^{yield}}$	0.9%
$\frac{\Delta N_{Z \rightarrow \mu\mu}^{yield, sys}}{N_{Z \rightarrow \mu\mu}^{yield}}$	1.8%
$\frac{\Delta(N_{\mu\tau}^{meas})}{N_{\mu\tau}^{meas} - N_{\mu\tau}^{bkg}}$	8.2%
$\frac{\Delta\epsilon_{trig\mu\tau}}{\epsilon_{trig\mu\tau}}$	3.1%
$\frac{\Delta\epsilon_{M_T} \oplus \Delta\epsilon_{other}}{\epsilon_{M_T} \oplus \epsilon_{other}}$	5.2%
$\frac{\Delta\epsilon_{\tau-Id}}{\epsilon_{\tau-Id}}$	10.4%

Table B.2.: Components of uncertainty of τ identification efficiency.

The value of τ identification efficiency evaluated with this method is $\epsilon_{\tau-Id} = 0.476$ with relative error $\Delta\epsilon_{\tau-Id}/\epsilon_{\tau-Id}=10.4\%$. This value is consistent with the τ -Id efficiency obtained using Monte Carlo simulation $\epsilon_{\tau-Id}^{MC} = 0.477$.

Appendix C.

RPC trigger of the CMS experiment

This appendix emphasizes author's involvement in the RPC trigger of the CMS experiment, which lasted for the whole period of his Ph.D. studies.. Author took active part in Resistive Plate Chamber (RPC) trigger construction and commissioning. He has participated in data taking runs (both cosmic and LHC), during which he was responsible for proper operation of RPC trigger and for the data analysis. Author was also responsible for RPC trigger related offline software (trigger emulator; data quality monitoring code), RPC trigger patterns lists development and RPC trigger firmware building. His contribution also includes study of possible RPC trigger upgrade using Gas Electron Multiplier (GEM) Detectors, which is was published in [69].

The Resistive Plate Chamber (RPC) trigger is one of the Level-1 (L1) muon subtriggers used in the CMS experiment. The goal of the L1 RPC trigger is to identify high p_T muons produced near the interaction point, determine the bunch crossing they originate from, estimate their transverse momenta, and provide information on how good this momentum determination by calculating a so called muon candidate quality. Muon candidates found by the RPC trigger are sent to the Global Muon Trigger (GMT), which matches candidates sent by RPC, CSC, and DT triggers (see Chapter 2). The L1 RPC Trigger is often referred as Pattern Comparator Trigger (PACT). The Warsaw CMS Group took a leading role in designing and construction of the L1 RPC trigger.

C.1. RPC trigger - principle of operation

In order to identify muons present in each event RPC trigger uses signals from RPC chambers, which are installed in endcaps and barrel region (up to $|\eta| < 1.6$). RPC are gaseous detectors dedicated for triggering. Due to relatively poor spatial resolution they

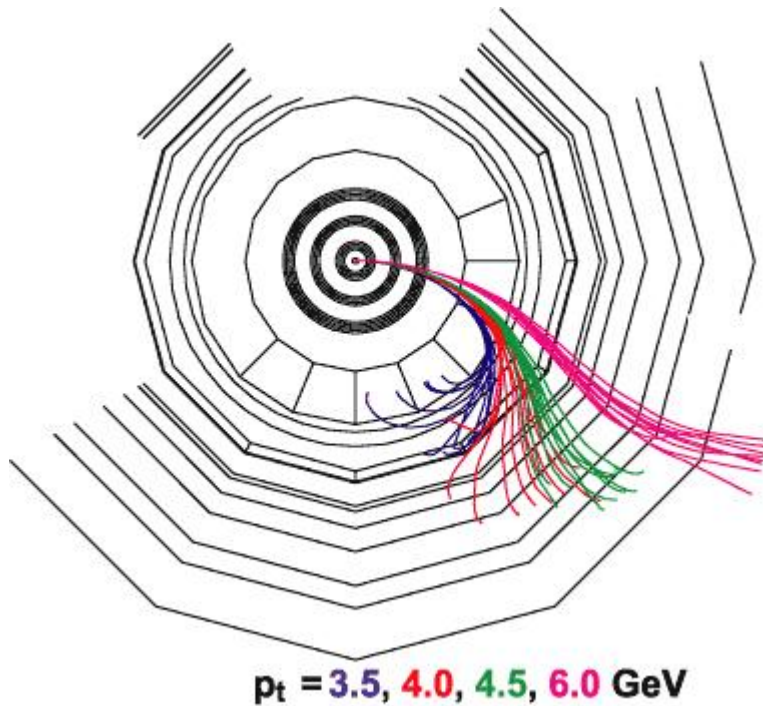


Figure C.1.: Muon passage through the detector in presence of the magnetic field. Tracks curvature depends on muon momentum, which allows track momentum determination.

are less useful for muon reconstruction - CSC and DT chambers suit better for this purpose. More information about RPC chambers can be found in Chapter 2.

Muon tracks produced in collision are bent in the magnetic field of the solenoid. Example trajectories of muons with transverse momenta of 3.5, 4, 4.5 and 6 GeV/c are shown in Figure C.1. Muon track curvature depends on its transverse momentum, while the direction of bending depends on its charge. This makes muon charge and transverse momentum measurement possible.

One possible approach to perform muon identification is to find so called seeds (e.g. two or three hits in the inner stations of the muon system) and iteratively add matching muon hits from further chambers, while updating the muon candidate's trajectory. Muon identification in the RPC trigger is done in a different, very elegant, way. A list of predefined configurations (patterns) of fired strips is searched for a pattern that matches best to the configuration of fired RPC strips actually present in given bunch crossing. A best matching pattern is called a muon candidate. Every pattern has two numbers assigned - a p_T code (which is a function of muon transverse momentum, see Table C.1) and a sign corresponding to the muon charge. List of patterns is obtained earlier from Monte

Code	p_T [GeV/c]	Code	p_T [GeV/c]	Code	p_T [GeV/c]	Code	p_T [GeV/c]
1	0.0	9	5.0	17	18.0	25	60.0
2	1.5	10	6.0	18	20.0	26	70.0
3	2.0	11	7.0	19	25.0	27	80.0
4	2.5	12	8.0	20	30.0	28	90.0
5	3.0	13	10.0	21	35.0	29	100.0
6	3.5	14	12.0	22	40.0	30	120.0
7	4.0	15	14.0	23	45.0	31	140.0
8	4.5	16	16.0	24	50.0		

Table C.1.: Lower edges of p_T codes ranges.

Carlo simulation. Detailed description and studies on the pattern generation procedure can be found in [70].

C.2. RPC trigger segmentation

RPC trigger design η segmentation is shown in Figure C.2 (with η coverage up to 2.1). Due to financial and technical reasons RPC chambers were installed up to $|\eta| < 1.6$ with only 3 layers present in the endcaps region. Increase of coverage in η is considered during one of forthcoming long breaks in LHC operation.

Pseudorapidity range currently covered by the RPC trigger (up to $|\eta| < 1.6$) is divided into 25 so called trigger towers. Every trigger tower is divided in the $r\phi$ plane into 144 logic segments (each one corresponds to about 2.5° in ϕ). Twelve consecutive logic segments form a logic sector (covering about 30° in ϕ , numbered from 0 to 11). Logic segment numeration starts with 0 for a segment covering ϕ range of $5 \dots 7.5^\circ$. Logic sectors are shifted with respect to chamber sectors (Figures C.3 and C.4).

Schematic view of the RPC trigger system is shown on Figure C.5. Signals from the RPC chambers are read by Front End Board (FEB). Most chambers have 6 FEBs connected in the barrel region and 3 FEBs in the endcaps region. FEBs send the signals to Link Boards (LB), whose task is to perform lossless data compression and send the data for further processing [71]. The data is sent only for chambers with at least one strip fired.

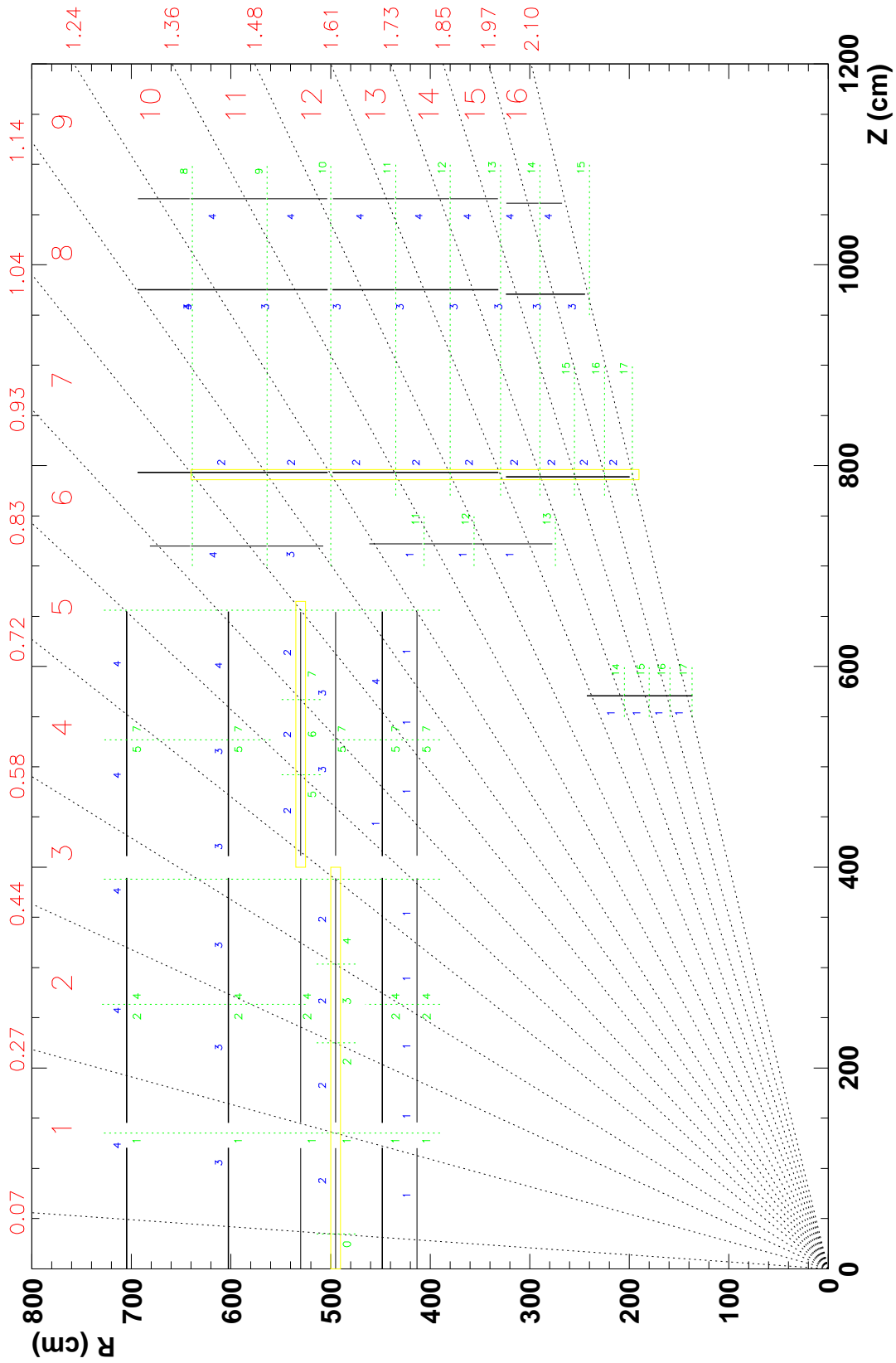


Figure C.2.: RPC trigger η segmentation with tower ranges. Reference planes marked in yellow. Figure shows the design segmentation with η up to 2.1. Due to financial and technical reasons RPC chambers were installed up to $|\eta| < 1.6$ with only 3 layers present in the endcaps region.

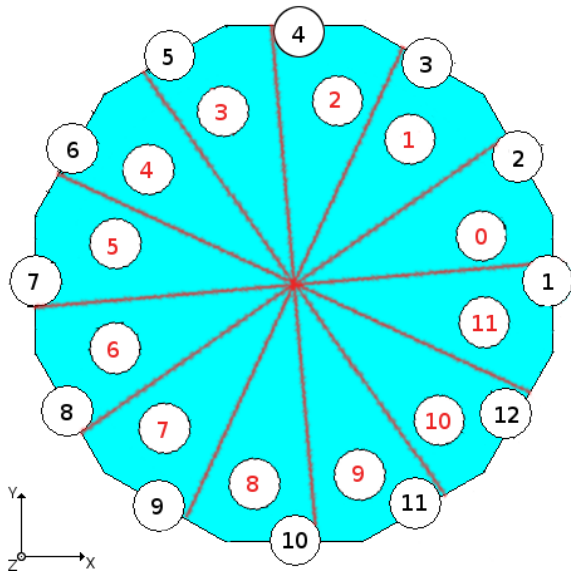


Figure C.3.: Chamber sector numeration (1...12, in black) along with logic sector numeration (0...11, in red). Note that logic sectors are shifted with respect to chamber sectors.

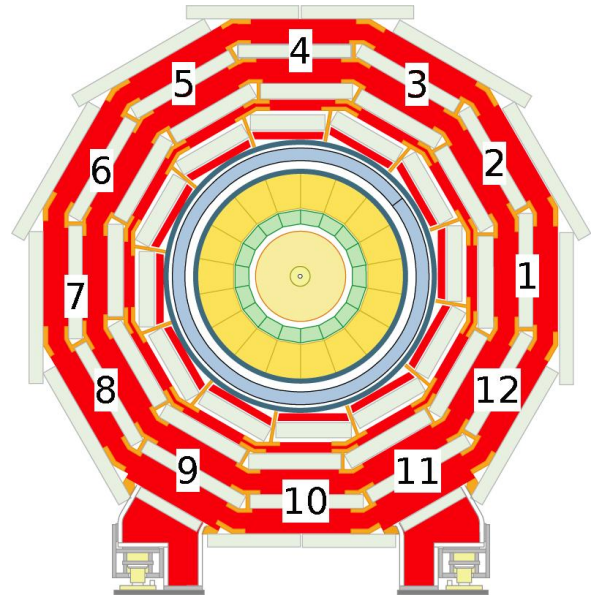


Figure C.4.: $r\phi$ view of CMS detector barrel with chamber sector numbering.

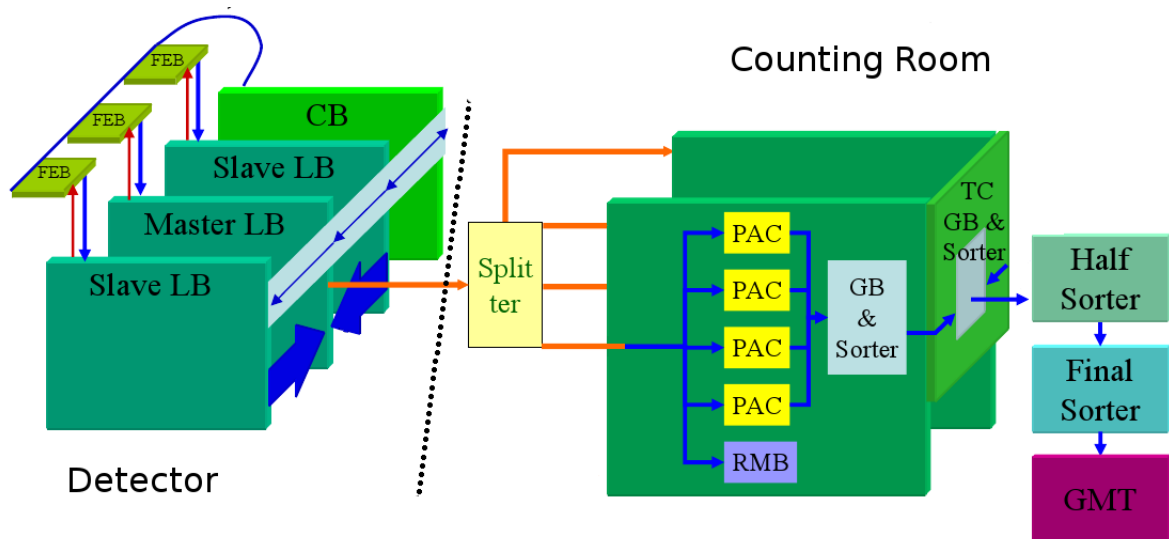


Figure C.5.: Schematic view of the RPC trigger system.

There are two types of LB - Slave and Master. Slave LB transmit the data to corresponding Master LB, which then sends the data to the counting room via optic fiber. A single Master LB distributes signals from not more than two Slave LB.

LBs and FEBs are controlled by Control Boards (CB). CB allow one to transmit data into LBs and FEBs, such as configuration (e.g. FEB thresholds) or load the firmware into LBs.

FEBs are mounted directly on the RPC chambers, while CBs and LBs are installed in the vicinity of the detector. Therefore it is crucial for these devices to be radiation hard.

The remaining part of the RPC trigger system is placed in a counting room, separated from the detector by thick concrete wall, therefore it is not required to be radiation hard.

Signals sent by LB are distributed by the splitters to the Trigger Boards (TB). On every TB a Readout Mother Board (RMB) is mounted (RMB is a mezzanine board). The role of the RMB is to concentrate the chamber data and to send it (via one of three Data Concentrator Cards - DCC) to the Data Acquisition (DAQ) system of the CMS experiment [72].

On the TB signals are also routed to Pattern Comparator processors (PAC) implemented in FPGA technology. Every TB contains from 3 to 4 PAC processors. Every PAC processor contains 12 PAC comparators. Every PAC comparator groups signals (information which strips were fired) into a logic cone, consisting of several (from 3 to 6, depending on trigger tower) logic planes. Every logic plane is made of logic strips. A logic strip corresponds to one or two physical strips with the same ϕ coordinate, but with different η .

Each PAC comparator performs a muon search in a single logic cone (therefore a single PAC processor performs a muon search in a single logic sector of a single tower). Majority of the RPC strips is assigned to two or more logical strips. This not applies to strips from a reference plane (marked in yellow in Figure C.2), which are assigned to exactly one logical cone.

Every TB performs the muon search inside a single logic sector inside 3 or 4 neighboring trigger towers. TB are placed in Trigger Crates (TC). Every TC contains 9 TB and performs the muon search in same logic sector of all towers. RPC trigger consists of 12 TC, which covers full ϕ range.

On every TB a Trigger Board Sorter is placed, which chooses 4 best candidates among those found in its TB. Selected muon candidates are sent then from TB to the Trigger Crate Sorter. Among them again four best are chosen.

Muon candidates are sent to Half Sorters (HS). Each of two HS chooses 4 best muon candidates for barrel and 4 for endcaps region. Selected candidates are sent to the Final Sorter, which chooses final 8 candidates - not more than 4 for barrel and 4 for endcaps region. Selected candidates are then sent to the Global Muon Trigger.

C.3. PAC algorithms

Two implementations of PAC comparator algorithm exist - baseline and economic. Each algorithm processes data grouped into a single logic cone.

C.3.1. Baseline algorithm

In this algorithm each pattern is compared separately with the configuration of fired (logical) strips. Pattern is considered as a muon candidate if one of following criteria is met:

- Pattern matches in at least 4 out of 6 planes (for high p_T patterns)
- Pattern matches in at least 3 out of 6 planes (for high p_T patterns) and matches are in three different muon stations
- Pattern matches in 3 out of 4 inner logic planes in barrel region (for low p_T patterns)
- Pattern matches in 3 out of 3 planes in endcap region (not depending on p_T)

For every muon candidate a quality is assigned (number from 0 to 3) depending of number of matching planes (0 for 3 planes matching, 3 for 6 planes matching). The final response of the PAC comparator is the p_T code of the best matching pattern (with the best quality). If there are several patterns with the same quality number, the one with highest p_T code is chosen.

The principle of operation of the baseline algorithm is shown in Figure C.6. Information about the fired RPC strips is grouped into a logic cone (on left). A pattern with the highest number of matching planes is assigned to this logic cone. When the quality criterion is not conclusive (patterns 2. and 3. match equally good), pattern with higher p_T code is chosen (2.).

C.3.2. Economic algorithm

In order to allow use of smaller FPGA devices in economic algorithm patterns with the same sign, p_T code and quality definition ¹ are grouped together. Patterns grouping is shown in Figure C.7.

¹Both algorithms allow to define quality on pattern basis (each pattern can have a different quality definition) as a function of configuration of matching planes

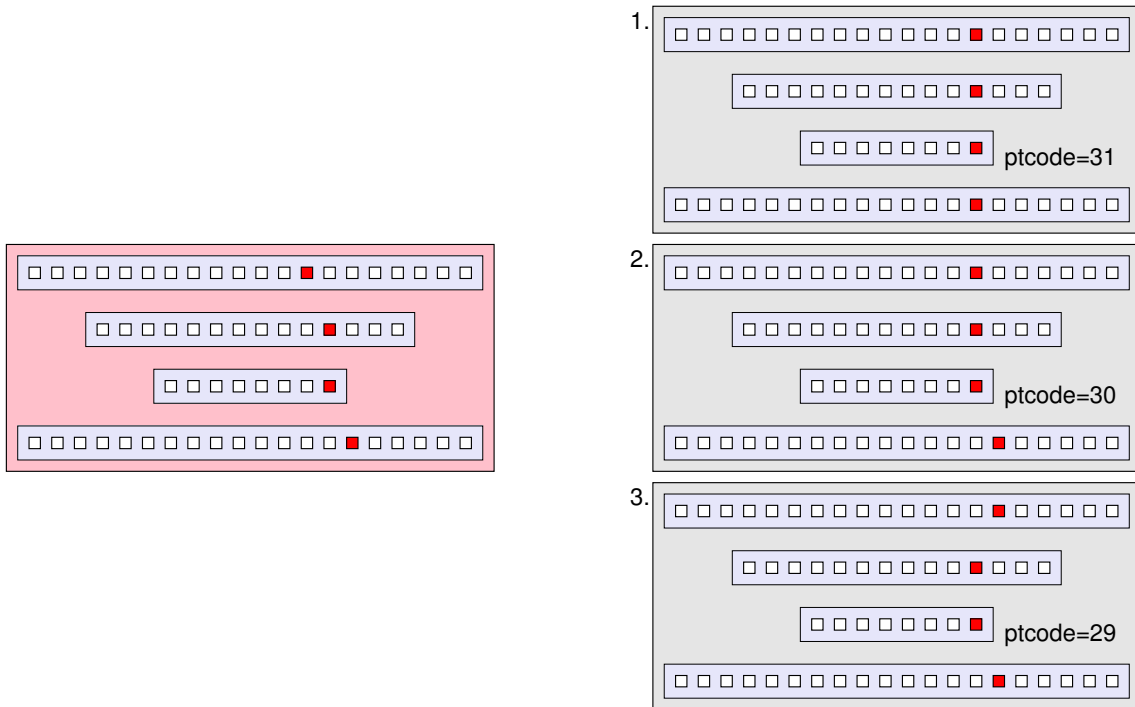


Figure C.6.: Baseline algorithm - principle of operation. The second pattern is chosen from the predefined pattern set (right) since it matches the best to the fired strip configuration (left).

As a result of grouping a mask is obtained, used to calculate the quality value within given group (in baseline algorithm quality is calculated for every pattern separately). In next step of the algorithm the mask is used to find planes in which no strip was fired. Strips in such planes are then treated by PAC comparator as fired (Figure C.8).

Usage of mask allows to use a single AND6 operation in order to check if fired strips configuration matches given pattern. For the baseline algorithm (for 6 planes case) a single AND6 operation is needed, 5 AND5 operations (one missing plane) and 15 AND4 operations (2 missing planes). Therefore the economic algorithm allows significant decrease of the FPGA chip logic utilization.

The only drawback of the economic algorithm is higher sensitivity to the detector noise. Economic algorithm will fail to find muon, when the passing muon won't fire a strip in a given plane and at the same time a different strip (in the same plane) will be fired due to the noise (such plane will be not considered as missing).

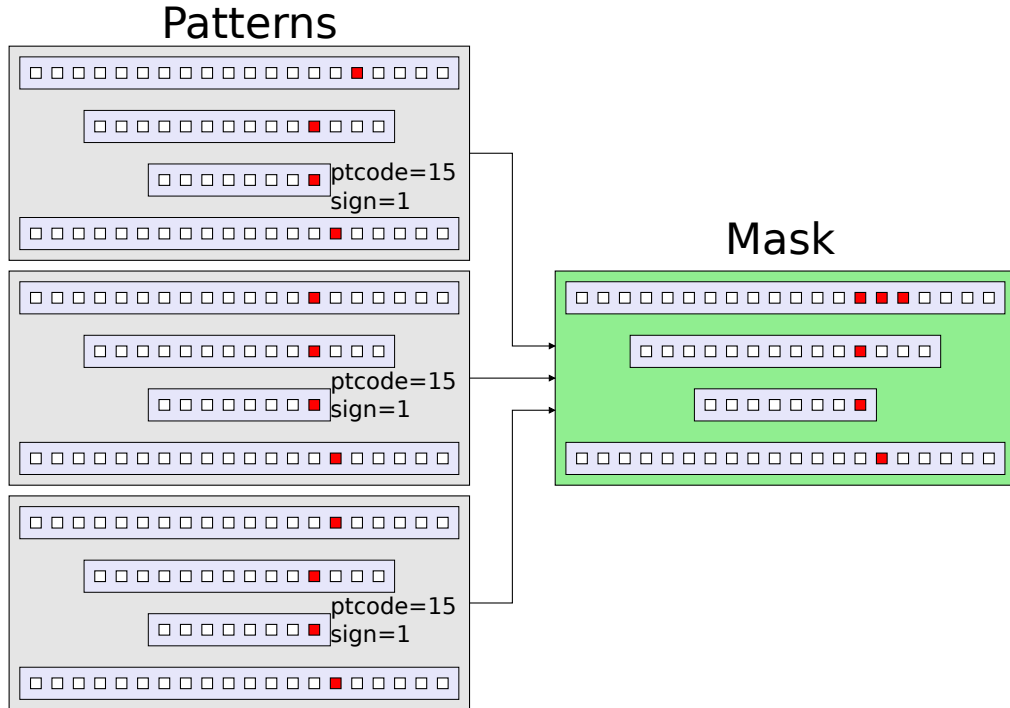


Figure C.7.: Patterns grouping in economic algorithm. As a result a mask is obtained (on right), used for quality calculation.

C.4. Ghostbusting

A single RPC strip can contribute to several logic cones. Therefore a single muon can be independently found by several neighboring PAC comparators, leading to more than one muon candidates. Such extra muon candidates are called ghosts. Appearance of ghosts is adverse, since leads to increase in L1 trigger rate (requirement on muon p_T is much lower in cases, where two muons are present) and often leads to an overestimate of the muon p_T . Therefore there an efficient algorithm of ghost removal is needed. Such procedure is called ghostbusting.

Principle of ghostbusting algorithm is shown in Figure C.9. Each filled cell corresponds to a muon candidate of given tower (η coordinate) and logic segment number (ϕ coordinate). A muon candidate will be considered as a ghost if there is a neighboring muon candidate with a higher quality present. In cases when both muon candidates have the same quality the one with higher p_T code is chosen. In rare cases ghostbusting algorithm fails, leading to the appearance of two muon candidates when a single muon was present. Example of such case is shown in Figure C.10. One of PAC comparators in tower 14 failed to find

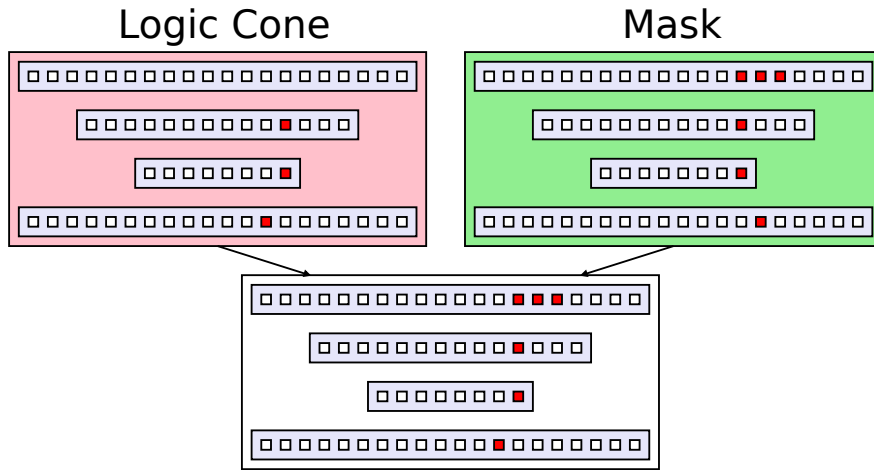


Figure C.8.: Finding of planes with no hits in economic algorithm. Mask obtained by patterns grouping (on right) is used to fill logic planes with no hits.

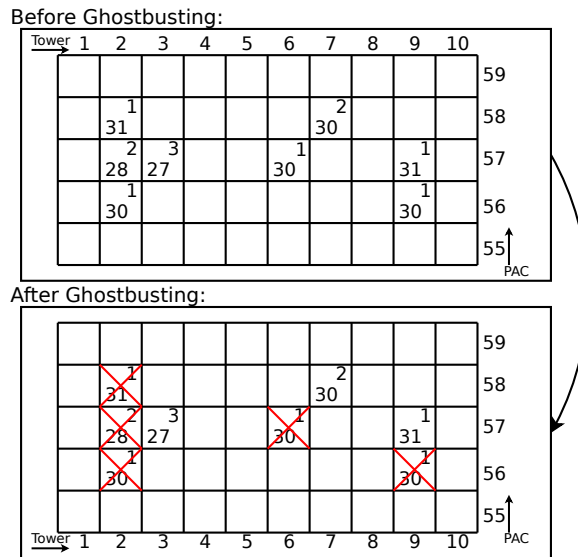


Figure C.9.: Principle of RPC trigger ghostbusting algorithm. In the bottom left corner of each cell the p_T code of the muon candidate is shown, in the top right the quality value.

a muon candidate, therefore conditions of the ghostbusting algorithm were not met. As a result two muon candidates were sent to GMT.

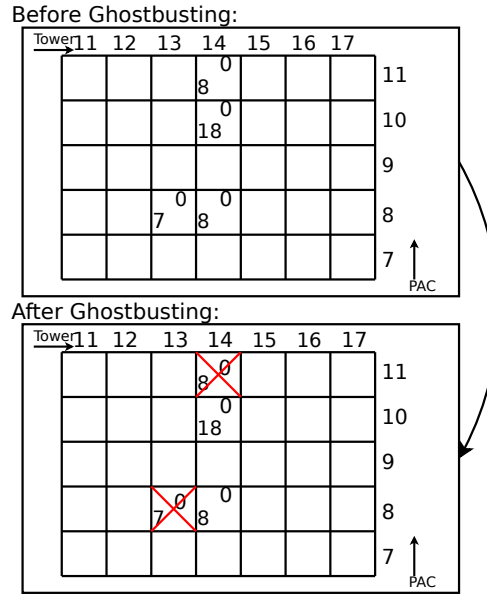


Figure C.10.: Example event in which ghostbusting algorithm fails to remove a ghost.

Ghostbusting algorithm is realized on sever different stages of the RPC trigger pipeline:

1. **Trigger Board** - ghostbusting is performed in two stages. In the first stage ghosts are marked as ghosts separately inside a given tower along the ϕ direction (since single PAC chip performs muon finding with a single tower). Since each TB performs muon finding in a single logic sector (30° in ϕ), ghostbusting is done only inside it. In the second stage ghostbusting is performed in the η direction for all towers in which the muons search is performed in given TB. From all muon candidates, that were not marked as ghosts, four best are chosen (depending on quality and p_T) and sent to the TC sorter. Muon candidates that were marked as ghost and were found near to the edge of sector or tower range of given TB are also sent to TC sorter.
2. **Trigger Crate** - ghostbusting is done inside TC sorter for all towers and given logic sector. From muon candidates that were not marked as ghosts up to 8 best are chosen - 4 for endcaps region and 4 for barrel region and sent to the Half Sorter. Muon candidates close to the logic sector boundary that were marked as ghosts an are also sent to Half Sorter.
3. **Half and Final Sorter** - performs final ghostbusting and sorting. As a results up to 8 best muon candidates (up to 4 for endcap and 4 for barrel) are sent to GMT.

C.5. Muon triggering with GEM detectors in the high- η region

The RPC system was designed to have coverage up to $|\eta| < 2.1$. Due to financial and technical reasons RPC chambers were installed up to $|\eta| < 1.6$ with only 3 planes present in the endcaps region. Increase of the coverage in η is considered during one of forthcoming long breaks in the LHC operation. One of the considered upgrade scenarios is to use GEM (Gas Electron Multiplier) type detector instead of RPC chambers. This section contains a study on triggering with GEM detectors using RPC trigger algorithms. Study was originally published in [69].

One of the main objectives of the proposed GEM detector system is to provide an additional muon trigger source redundant with the CSC trigger to ensure robust triggering on forward muons at the high luminosity LHC and beyond. In this section, we give a brief overview of the existing RPC trigger system followed by initial results from an GEM trigger emulation study, which is derived from the existing CMS RPC trigger emulation.

C.5.1. Trigger emulation

GEM chambers are characterized by very fine readout granularity. For this first simulation, we make the assumption that the trigger is to be derived by the same or a very similar trigger hardware system based on PAC chips as the current RPC trigger. Since the PAC chips have limited pattern capacity, the RPC trigger would then have to receive signals from GEM chambers that are logical OR's of several neighboring GEM strips. Possibility of triggering with the current L1 RPC trigger electronics design with use of ORed GEM signals is presented.

In addition to the basic analysis presented below, two or more layers of GEM-like chambers in one muon station may provide an independent precise measurement of a local track bending angle. Benefitting from full GEM chamber resolution locally available to a GEM-based trigger, such a measurement may be used at the end of the trigger logic to further constrain the momentum of reconstructed track candidates. This kind of improvement applies mainly to station GE1/1, but it can be also used in other parts of the muon system where the muon trigger has difficulties. A substantial gain in momentum resolution at the trigger level may be obtained by replacing the RPCs in RE1/2 and RE1/3 with GEMs. In addition, an extra layer of GEM-like chambers in the pseudorapidity range $1 < |\eta| < 1.6$ placed just in front of or behind the CMS coil may substantially improve

CMS muon triggering capabilities. However, these more advanced potential extensions of GEM usage in the trigger are not included in the initial studies described below.

In order to fully benefit from the bending power of the magnetic field between the two innermost stations (GE1/1 and GE2/1), the muon quality definition was optimized. Muon candidates built from patterns matching in all four muon stations are preferred, with the quality value set to 2. If the pattern matches in the first two layers GE1/1 and GE2/1 and in either one of the two outermost layers (3/1 or 4/1), the muon candidate receives a lower value of quality (1). In all other cases, when the pattern matches in three planes, the muon candidate receives the lowest value of quality (0). If the pattern matches in fewer than three planes, no muon candidate is found.

Patterns used in this study were generated using the standard procedure, i.e. the same as used for pattern generation for data taking, independently for all tested geometry variations. In order to avoid negative effects due to reconstruction of low p_T with low quality with high assigned transverse momentum, a “wide” pattern was inserted to all pattern sets (for all tested geometry variations). As a result, all muons that left hits in all four planes and that do not have any pattern matching in all four planes, will be assigned the lowest transverse momentum possible. Extensive information on pattern generation can be found in [70].

C.5.2. GEM geometry

The RPC trigger emulation in the standard CMS experiment software framework (CMSSW, [25]) was used without major changes. During trigger emulation, the RPC trigger logic was enabled only in trigger towers 13-16, which is the region where the RPC geometry was changed to a GEM-like geometry. A modified version of the baseline TDR CMS detector geometry [73] was used, with four fully instrumented chamber planes present in the endcap regions with $|\eta|$ coverage up to 2.1.

Fig. C.11 shows the RPC trigger tower segmentation in a longitudinal view of one quadrant of the CMS detector as given in the original Muon TDR. The geometry description of chambers RE1/1 and RE2/1 marked by green rectangles was modified by increasing the number of strips in these layers to emulate the higher granularity of GE1/1 and GE2/1 GEM chambers. For this study, the number of strips in the RPC chambers in the third and fourth endcap layer (RE 3/x and 4/x) was not changed since the bending power of the magnetic field is small in this region when compared to the region where RE1/1 and RE2/1 are located.

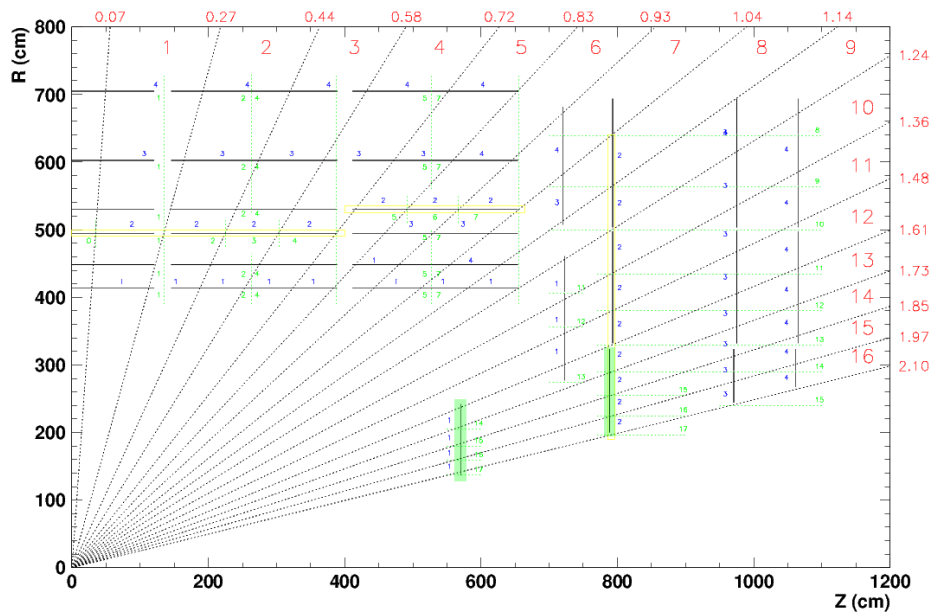


Figure C.11.: Longitudinal view of the current RPC trigger towers in one quadrant of the CMS detector. Chambers in areas marked with green (RE1/1, RE2/1) were modified to have increased number of strips to simulate the use of GE1/1 and GE2/1 GEM stations in those locations.

In total 4 different strip readout geometries were tested:

- **base** - baseline RPC design geometry as outlined in the Muon TDR ([73])
- **2×** - geometry with two times higher number of strips in RE1/1 and RE2/1
- **4×** - geometry with four times higher number of strips in RE1/1 and RE2/1
- **8×** - geometry with eight times higher number of strips in RE1/1 and RE2/1

C.5.3. Simulated chamber properties

The trigger studies were done in two stages. In the first stage, the impact of changes in geometry was tested while assuming perfect chamber operation, both for GEM and RPC chambers, i.e. no noise, no clusters (charged particle always fires exactly one strip), and 100% chamber efficiency, i.e. the “ideal” chamber model. In the second stage, chamber effects were included in a “realistic” chamber model. Here the simulated chamber efficiency was set to 95%, an average cluster size of two was used for RPC chambers while for the GEM chambers the clustering remained disabled. The latter choice was motivated by the assumption that the RPC trigger will not use the full GEM chamber granularity. In this

model, the simulation of noise still remained disabled for both types of chambers since it is hard to estimate expected noise in the GEM chambers at this point.

C.5.4. Results

Fig. C.12 and C.13 show the dependence of GEM+RPC L1 trigger output rates on the p_T threshold for all simulated geometries. The shape of the single-muon input rate as function of p_T is generated based on the shape in Ref. [74] and normalized to $10^{34} \text{ cm}^{-2}\text{s}^{-1}$ luminosity. Results sum trigger rates for trigger towers -16 to -13 and 13 to 16. The overall rate is dominated by muon candidates with lowest quality 0. This effect is visible for all geometries; it is higher for the realistic chamber model when compared to the ideal one. This is not surprising since due to the definition of “quality” the muon candidates with quality 0 use only one muon trigger station for momentum measurement and do not benefit from increased spatial resolution. Consequently, only contributions from muon candidates with qualities 1 and 2 will be considered further in our discussion.

The most important result observed in these plots is that the rate for muon candidates with higher qualities 1 and 2 flattens out above $p_T = 26 \text{ GeV}/c$ for the RPC-only “base” geometry. By contrast, in the $2\times$, $4\times$, and $8\times$ scenarios that make use of GEM chambers, the rate continues to decrease with increasing p_T threshold. This indicates that a L1 trigger upgraded with information from GEM chambers allows continued use of the p_T trigger threshold as a powerful tool to control muon trigger rates.

We also find that the higher the strip readout granularity, the lower the muon trigger rates for a given p_T threshold. Fig. C.14 shows the total L1 GEM+RPC trigger output rate as a function of different geometries for different p_T thresholds and for both chamber simulation models. The contribution from muon candidates with low quality 0 is not included here. The biggest relative improvement occurs when going from the base geometry to the $2\times$ geometry. A further increase in the number of strips lowers the rate further, but the relative improvement is smaller due to a non-linear dependence. The number of trigger patterns grows with the number of strips used. Since the existing PAC chips have limited capacity, a full upgrade of the PAC system, in the future, could match the GEM installation schedule in such a way that it exploits the capabilities of the combined system.

Fig. C.15-C.18 show the simulated trigger turn-on curves for trigger tower 13², i.e. the L1 trigger efficiencies for all geometry variations and for three different p_T thresholds (16, 50, and 140 GeV/c) as a function of the true muon transverse momentum. The

²Results for trigger towers 14-16 can be found in [69]

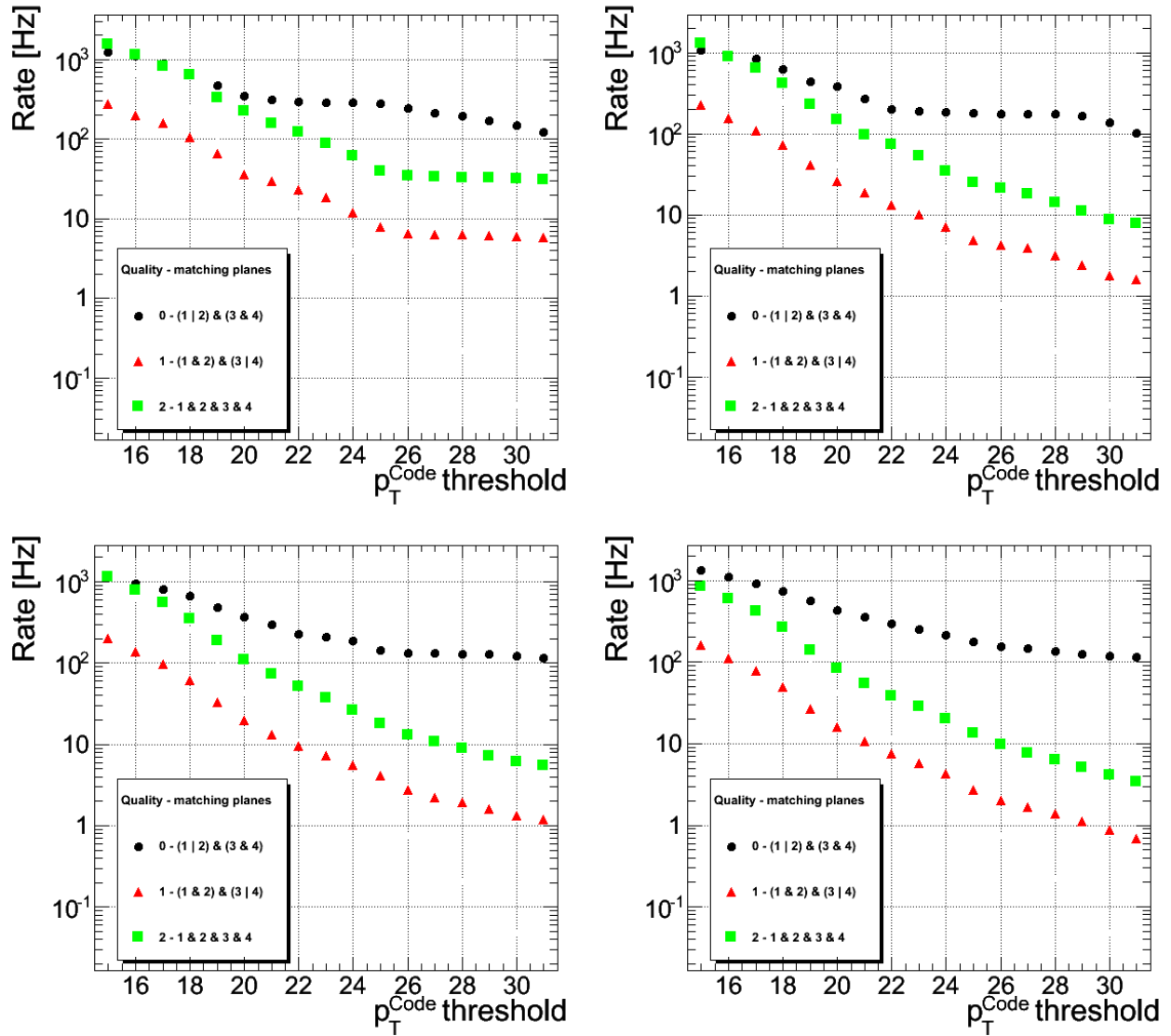


Figure C.12.: Simulated L1 GEM+RPC trigger output rates summed over trigger towers -16 to -13 and 13 to 16 vs. p_T cut for ideal chamber model (top left: base, top right: 2 \times , bottom left: 4 \times , bottom right: 8 \times strip granularity).

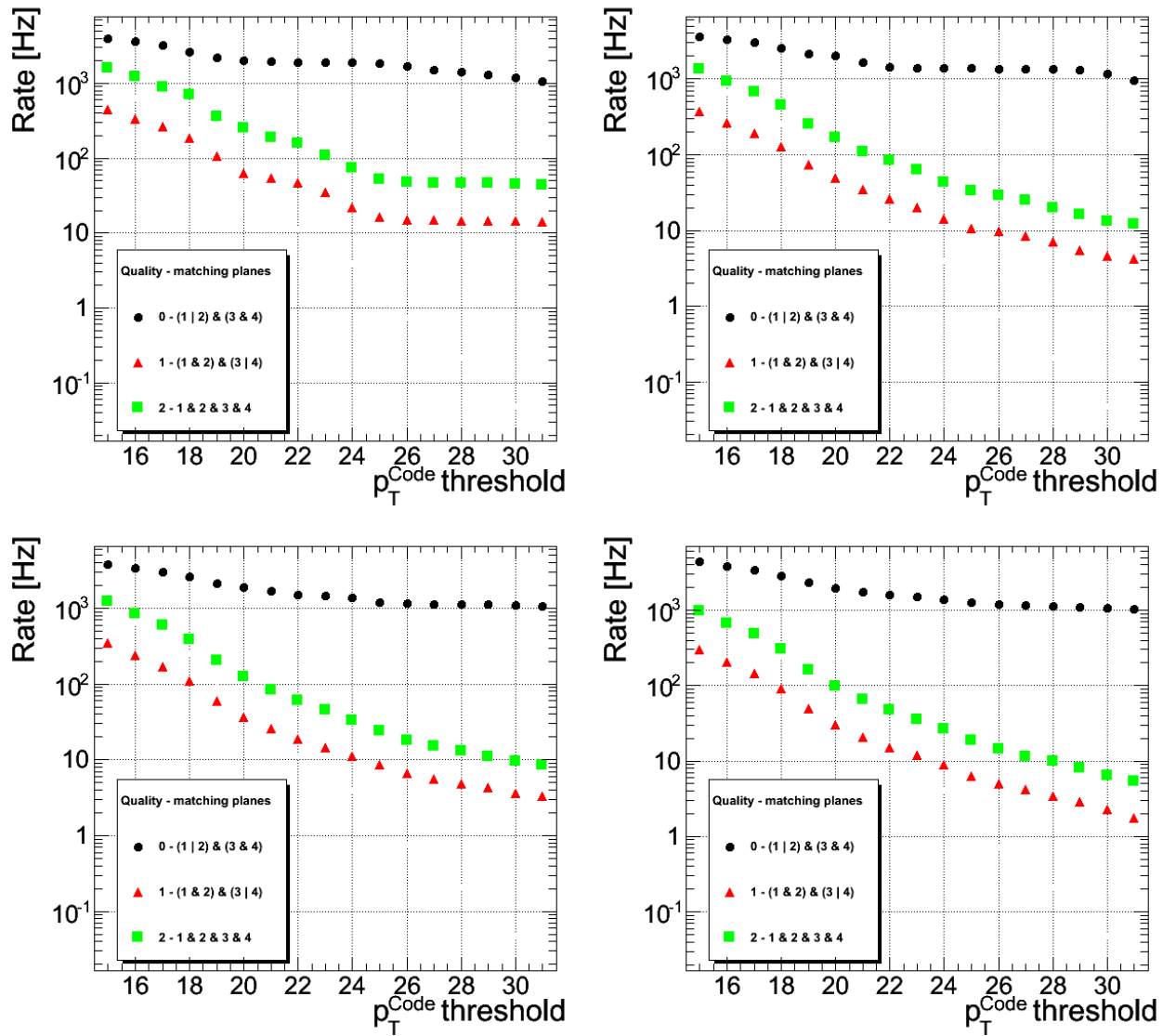


Figure C.13.: Simulated L1 GEM+RPC trigger output rates summed over trigger towers -16 to -13 and 13 to 16 vs. p_T cut for realistic chamber model (top left: base, top right: $2\times$, bottom left: $4\times$, bottom right: $8\times$ strip granularity).

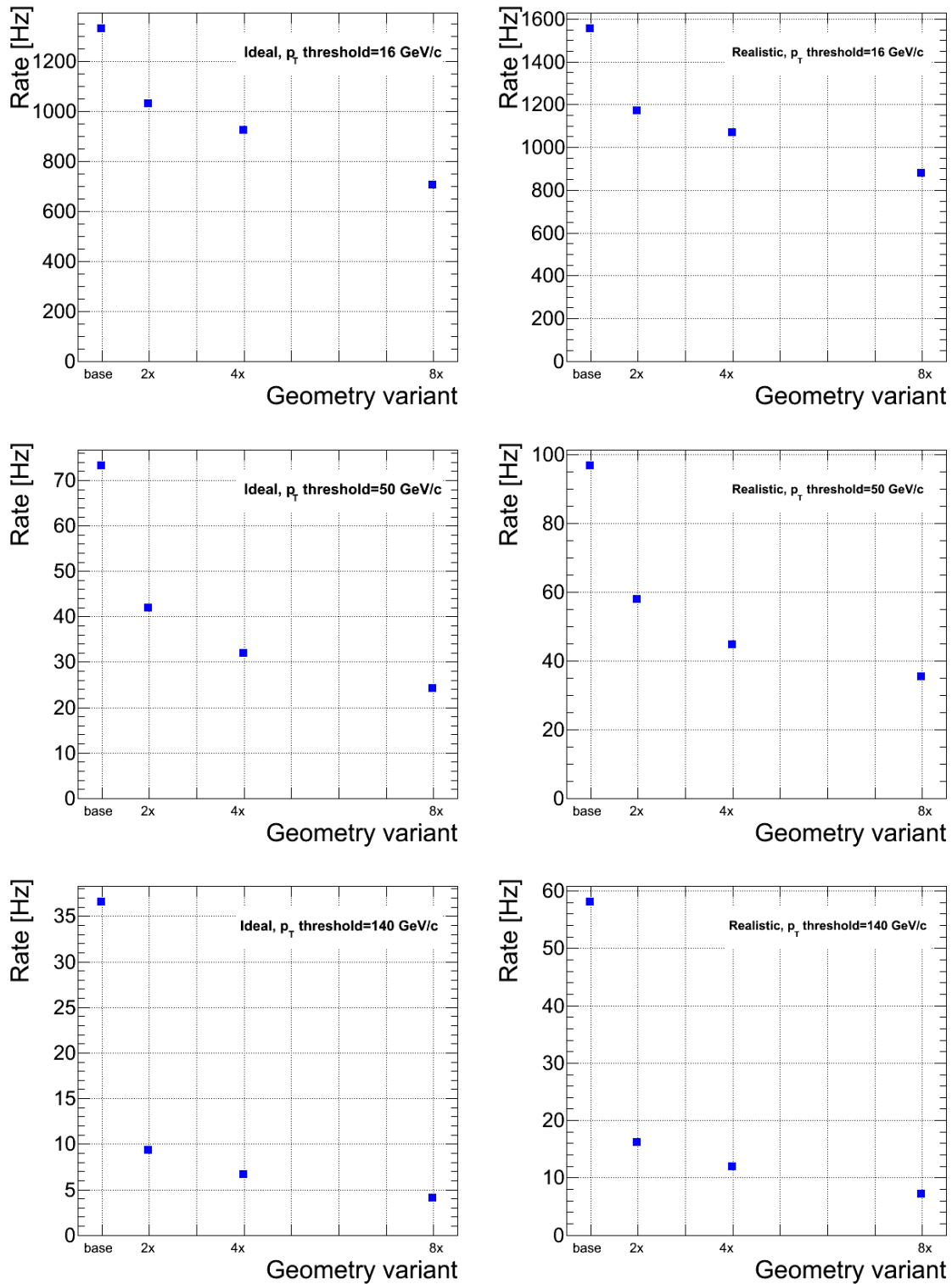


Figure C.14.: Simulated total L1 GEM+RPC trigger output rates as function of different geometries for ideal (left) and realistic (right) chamber models. Rows correspond to three different p_T thresholds of 16, 50, and 140 GeV/c. Only the contribution from muon candidates of quality 1 or 2 is shown.

efficiency curves get worse in general for higher tower numbers due to the decreasing bending power of the magnetic field. The turn-on curves become much sharper as the GEM strip granularity increases. The higher the p_T threshold, the more dramatic the effect. For instance, with a 140 GeV/c threshold, the current “base” RPC trigger accepts typically over 80% of all muons with a momentum of just 60 GeV/c or higher, i.e. the RPC trigger rejection with this high threshold is actually very ineffective. This is because the current RPC pattern trigger has difficulties distinguishing the momenta of very straight tracks from each other due to its coarse granularity. For the $8\times$ GEM+RPC geometry, this 80% point with a 140 GeV/c threshold moves up to 120-140 GeV/c making the L1 trigger rejection much more effective.

From these first simulation studies we conclude that the GEM detector stations would significantly improve the L1 muon trigger performance over that of the originally planned RPC-only system in the forward direction $|\eta| > 1.6$.

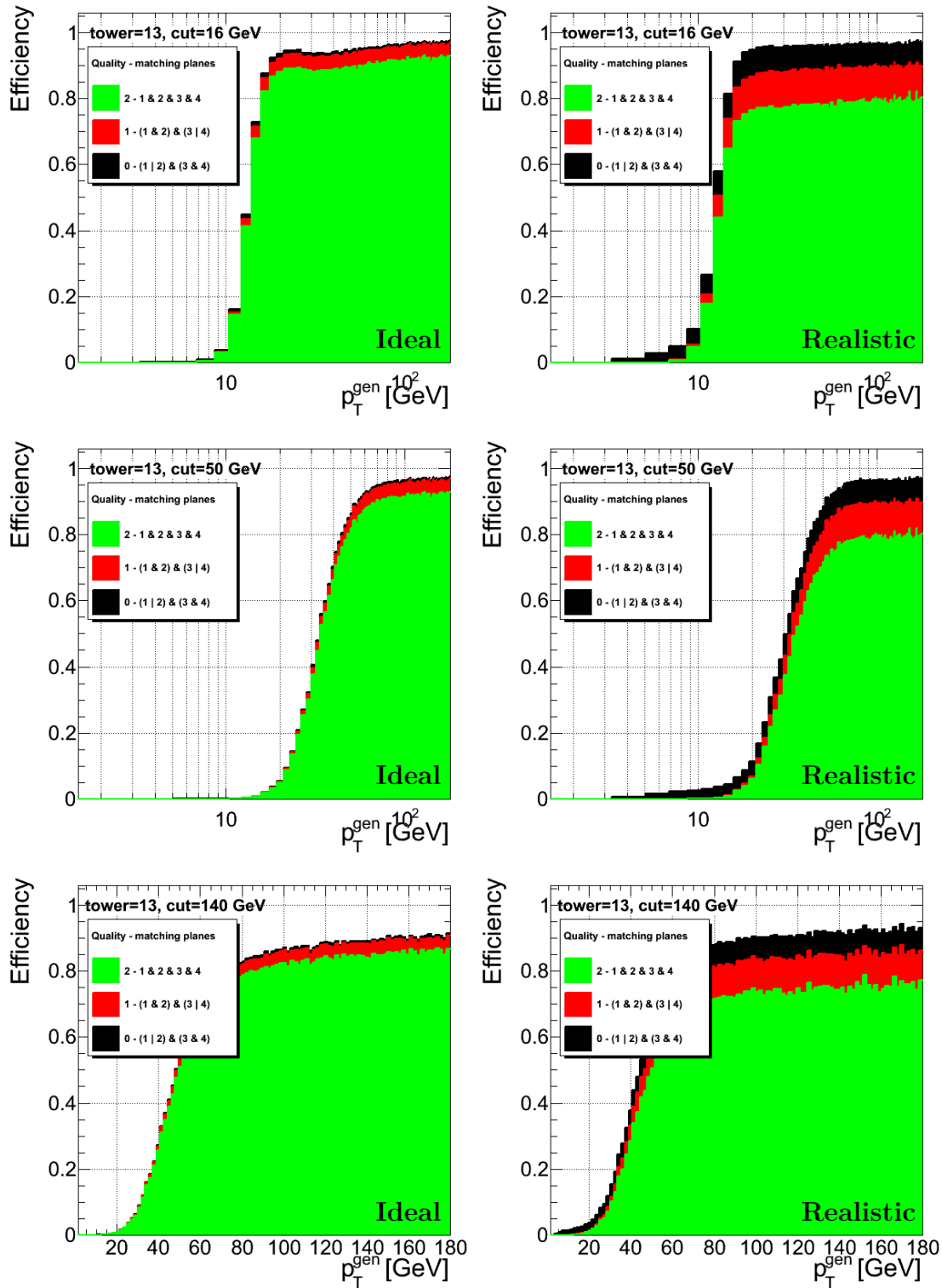


Figure C.15.: L1 GEM+RPC trigger efficiency curves in trigger tower 13 for base geometry. Rows correspond to 3 different p_T thresholds of 16, 50, and 140 GeV/c, respectively. Left column shows results for ideal chamber model, right for realistic chamber model.

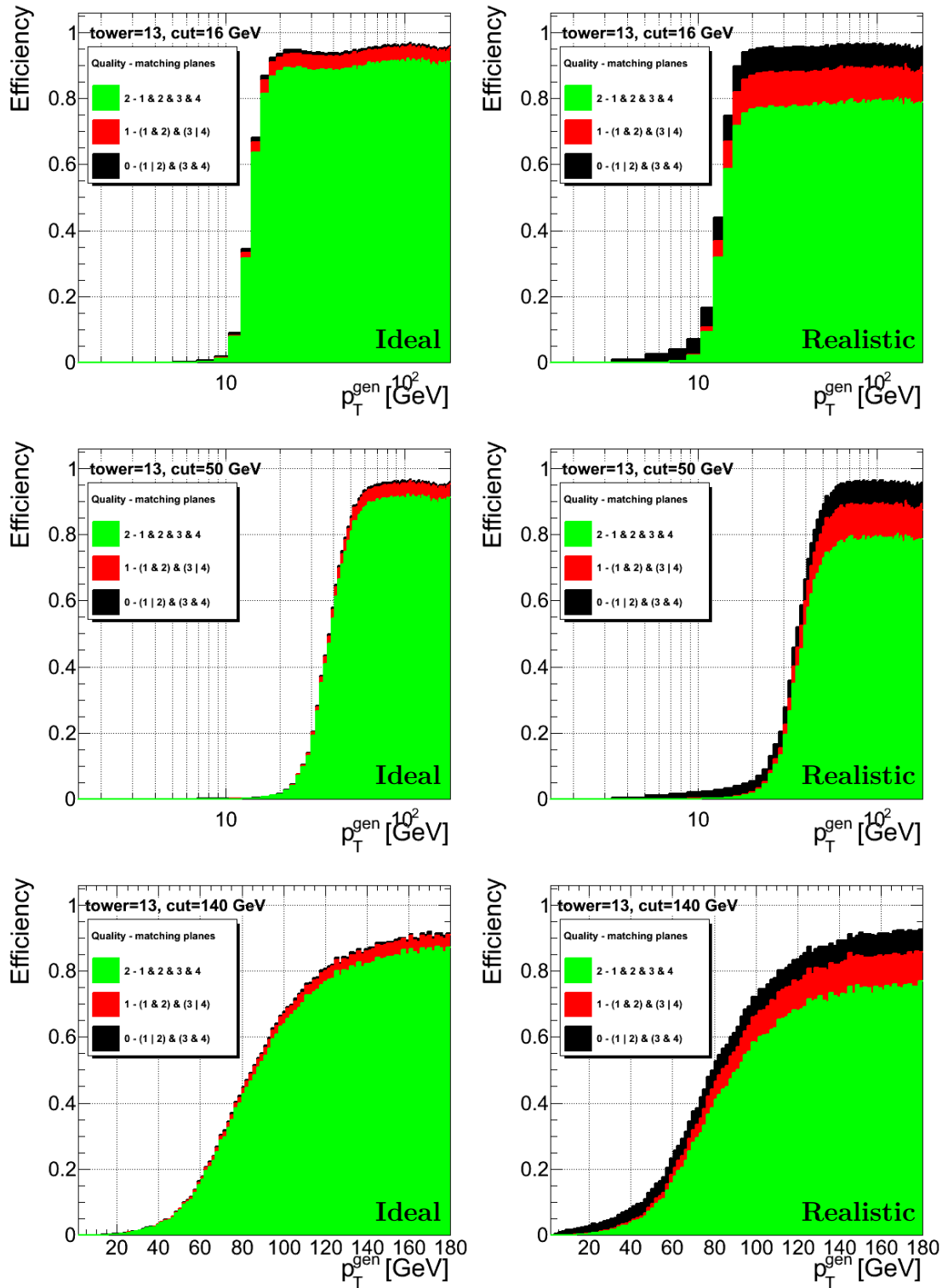


Figure C.16.: L1 GEM+RPC trigger efficiency curves in trigger tower 13 for $2\times$ geometry. Rows correspond to 3 different p_T thresholds of 16, 50, and 140 GeV/c, respectively. Left column shows results for ideal chamber model, right for realistic chamber model.

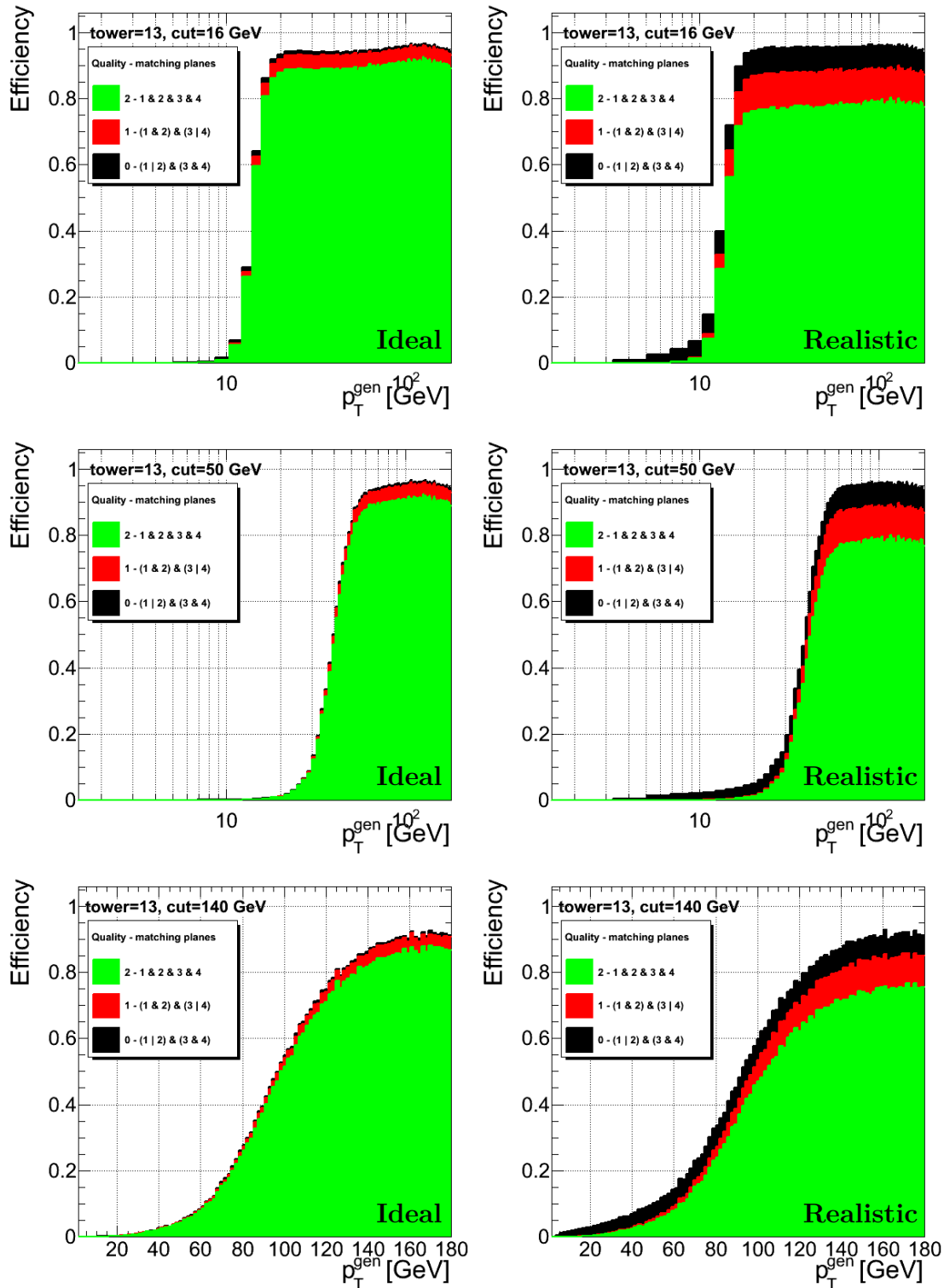


Figure C.17.: L1 GEM+RPC trigger efficiency curves in trigger tower 13 for $4 \times$ geometry. Rows correspond to 3 different p_T thresholds of 16, 50, and 140 GeV/c, respectively. Left column shows results for ideal chamber model, right for realistic chamber model.

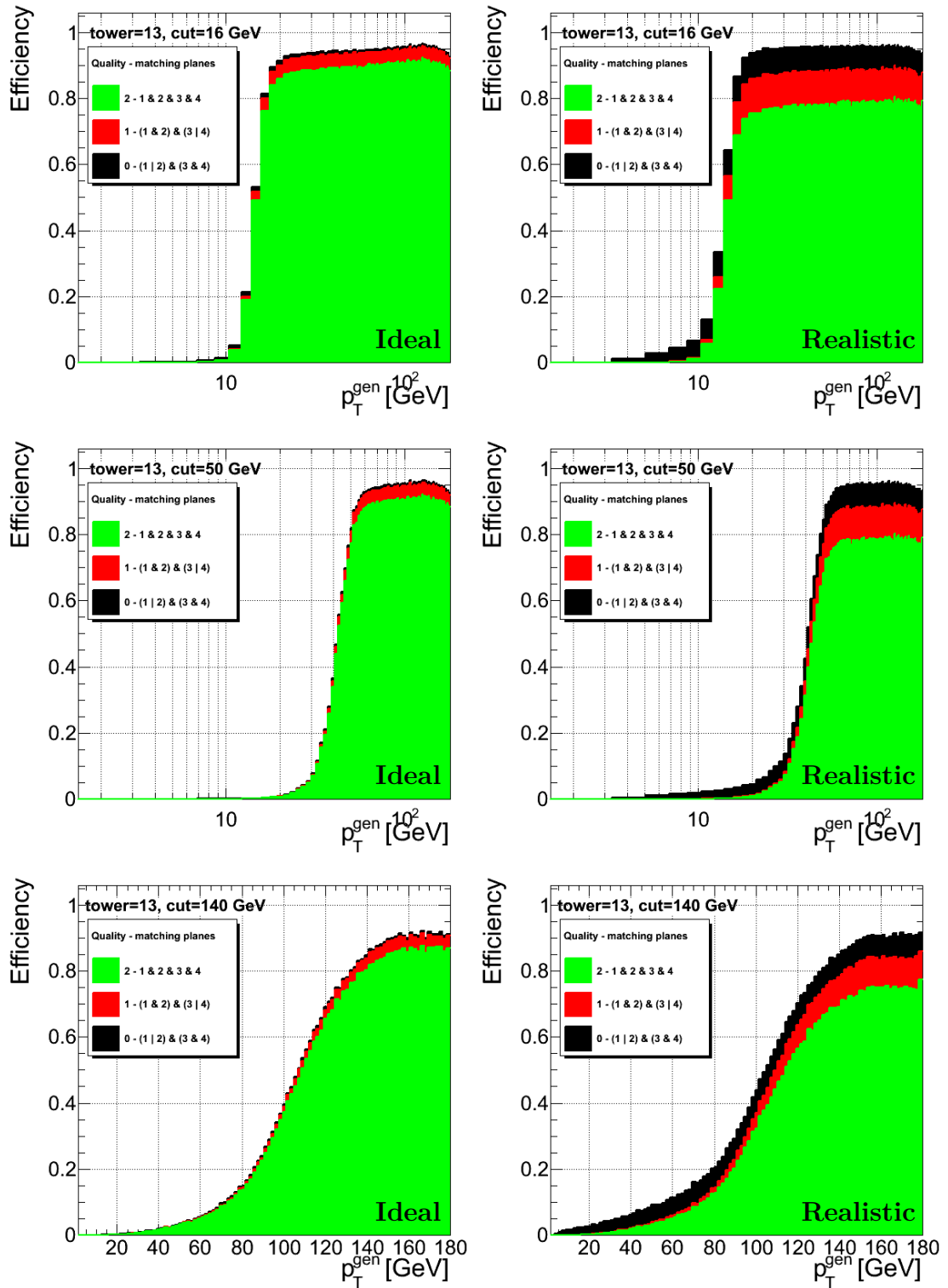


Figure C.18.: L1 GEM+RPC trigger efficiency curves in trigger tower 13 for $8 \times$ geometry. Rows correspond to 3 different p_T thresholds of 16, 50, and 140 GeV/c, respectively. Left column shows results for ideal chamber model, right for realistic chamber model.

Bibliography

- [1] The Standard Model was described in numerous publications. A comprehensive description can be found in a book by C. Burgess, G. Moore, *The Standard Model: A Primer*, Cambridge University Press, 2006
- [2] A. Salam, *Weak and electromagnetic interactions*, in Elementary particle physics: relativistic groups and analyticity, N. Svartholm, ed., p. 367. Almqvist & Wiskell, 1968. Proceedings of the eighth Nobel symposium
- [3] S. Glashow, *Partial-symmetries of weak interactions*, Nuclear Physics 22 (4): 579-588
- [4] S. Weinberg, *A Model of Leptons*, Physical Review Letters 19 (21): 1264-1266
- [5] P. Higgs, *Spontaneous symmetry breakdown without massless bosons*, Phys. Rev. 145 (1966) 1156
- [6] The Super-Kamiokande Collaboration, *Evidence for oscillation of atmospheric neutrinos*, Physical Review Letters 81 (8): 1562-1567
- [7] G. Hinshaw (WMAP Collaboration) et al, *Five-Year Wilkinson Microwave Anisotropy Probe Observations: Data Processing, Sky Maps, and Basic Results*, The Astrophysical Journal Supplement 180 (2): 225-245, arXiv:astro-ph/0803.0732, 2009
- [8] ALEPH, DELPHI, L3 and OPAL Collaborations, The LEP working group for Higgs boson searches, *Search for the Standard Model Higgs Boson at LEP*, CERN-EP/2003-011, 2003
- [9] The ALEPH, CDF, D0, DELPHI, L3, OPAL, SLD Collaborations, the LEP Electroweak Working Group, the Tevatron Electroweak Working Group, the SLD electroweak and heavy flavour groups, *Precision Electroweak Measurements and Constraints on the Standard Model*, CERN-PH-EP-2010-095, 2010
- [10] L. Randall, R. Sundrum, *Large Mass Hierarchy from a Small Extra Dimension*, Physical Review Letters 83 (17): 3370-3373, arXiv:hep-ph/9905221
- [11] S. Dittmaier et al., *Handbook of LHC Higgs Cross Sections: 2. Differential Distributions*, arXiv:1201.3084v1
- [12] S. Dittmaier et al., *Handbook of LHC Higgs Cross Sections: 1. Inclusive Observables*, arXiv:1101.0593
- [13] *The Compact Muon Solenoid Technical Proposal*, CERN/LHCC 94-38, 1994
- [14] T. Christiansen, *The CMS magnet test and cosmic challenge*, arXiv:0805.1882v1

- [15] R. Mankel, *Measurement of the Transverse Beam Line Width Using Impact Parameter Correlations*, CMS AN-2010/196
- [16] The CMS Collaboration, *CMS tracking performance results from early LHC operation*, Eur. Phys. J. C (2010) 70: 1165-1192
- [17] <https://twiki.cern.ch/twiki/bin/view/CMSPublic/DPGResultsTRK>
- [18] The CMS Collaboration, *Measurement of Momentum Scale and Resolution of the CMS Detector using Low-mass Resonances and Cosmic Ray Muons*, CMS-PAS-TRK-10-004
- [19] CMS Collaboration, *The CMS muon project: Technical Design Report*, CERN-LHCC-97-032
- [20] CMS Collaboration, *Performance of the CMS Cathode Strip Chambers with Cosmic Rays*, arXiv:0911.4992
- [21] CMS Collaboration, *Performance of the CMS Resistive Plate Chambers (RPC) in 2011*, CMS-DP-2012-001
- [22] *CMS computing: Technical Design Report*, CERN-LHCC-2005-023
- [23] *Technical Design Report, Volume 1: The Trigger Systems*, CERN/LHCC 2000-38
- [24] G. Bauer et al., *The CMS High Level Trigger System: Experience and Future Development*, CERN-CMS-CR-2012-147
- [25] *CMSSW Application Framework*, twiki.cern.ch/twiki/bin/view/CMSPublic/WorkBookCMSSWFramework
- [26] D. Hufnagel, *The architecture and operation of the CMS Tier-0*, 2011 J. Phys.: Conf. Ser. 331 032017
- [27] The CMS Collaboration, *Description and performance of the CMS track and primary vertex reconstruction*, TRK-11-001
- [28] W. Erdmann *Offline Primary Vertex Reconstruction with Deterministic Annealing Clustering*, CMS IN-2011/014
- [29] The CMS Collaboration, *Performance of CMS muon reconstruction in pp collision events at $\sqrt{s} = 7$ TeV*, CMS-MUO-10-004
- [30] The CMS Collaboration, *CMS Physics TDR, Volume I: Detector Performance and Software*, CERN-LHCC-2006-001,
- [31] The CMS Collaboration, *Electron reconstruction and identification at $\sqrt{s} = 7$ TeV*, CMS PAS EGM-10-004
- [32] M. Pioppi. *Electron Pre-identification in the Particle Flow framework*, CMS AN-2008/032
- [33] W. Adam, R. Fruhwirth, A. Strandlie, T. Todorov, *Reconstruction of Electrons with the Gaussian-Sum Filter in the CMS Tracker at the LHC* J. Phys. G: Nucl. Part. Phys. 31 (2005) N9-N20.

- [34] The CMS Collaboration, *ECAL Detector Performance, 2011 Data*, CMS DP-2012/007
- [35] The CMS Collaboration, *Photon reconstruction and identification at $\sqrt{s} = 7$ TeV*, CMS PAS EGM-10-005
- [36] The CMS Collaboration, *Particle-Flow Event Reconstruction in CMS and Performance for Jets, Taus, and E_T^{miss}* , CMS PAS PFT-09-001
- [37] The CMS Collaboration, *MET performance in CMS*, JME-07-001
- [38] The CMS Collaboration, *Performance of Track-Corrected Missing E_T in CMS*, JME-09-010
- [39] The CMS Collaboration, *Missing transverse energy performance of the CMS detector*, JME-10-009
- [40] G. Soyez, G. Salam, *A practical Seedless Infrared-Safe Cone jet algorithm*, JHEP 05 (2007) 086
- [41] S. Catani et al., *Longitudinally invariant K_t clustering algorithms for hadron hadron collisions*, Nucl.Phys. B406 (1993) 187-224
- [42] M. Cacciari et al., *The anti- k_t jet clustering algorithm*, JHEP 0804:063,2008
- [43] The CMS Collaboration, *Jet Performance in pp Collisions at 7 TeV*, CMS PAS-JME-10-003
- [44] The CMS Collaboration, *Search For Neutral MSSM Higgs Boson Production via Decays to Tau Pairs in pp Collisions at $\sqrt{s} = 7$ TeV*, CMS-PAS-HIGG-10-002
- [45] J. Beringer et al. (Particle Data Group), Phys. Rev. D86, 010001 (2012)
- [46] B. P. Roe et al., *Boosted Decision Trees as an Alternative to Artificial Neural Networks for Particle Identification*, arXiv:physics/0408124v2
- [47] S. Agostinelli, J. Allison, K. Amako et al., *Geant4 a simulation toolkit*, Nuclear Instruments and Methods in Physics Research Section A: Accelerators, Spectrometers, Detectors and Associated Equipment 506 (2003), no. 3, 250-303.
- [48] M. Bluj, A. Burgmeier, T. Fruboes, G.Quast, M. Zeise, *“Particle flow based τ embedding”*, CMS AN-2011/020
- [49] *HepMC a C++ Event Record for Monte Carlo Generators*, <http://lcgapp.cern.ch/project/simu/HepMC/>
- [50] Z.Was, *TAUOLA the library for tau lepton decay, and KKMC/KORALB/KORALZ/... status report*, Nucl. Phys. Proc. Suppl. 98 (2001) 96-102, arXiv:hep-ph/0011305
- [51] Tomasz Fruboes et al, *Progress with rehit based embedding*, <https://indico.cern.ch/getFile.py/access?contribId=26&sessionId=1&resId=0&materialId=slides&confId=180813>
- [52] <https://twiki.cern.ch/twiki/bin/view/CMSPublic/SidraFit>

- [53] Ivan Mikulec, private communication
- [54] https://twiki.cern.ch/twiki/bin/view/CMS/MuonReferenceResolution#General_recommendations_for_muon
- [55] Higgs to Tau Tau group, *Search for Higgs Bosons Decaying to Tau Pairs in pp Collisions at $\sqrt{s} = 7$ TeV*, CMS AN-2011/390
- [56] The CMS Collaboration, *Search for neutral Higgs bosons decaying to tau pairs in pp collisions at $\sqrt{s} = 7$ TeV*, arXiv:1202.4083, Phys. Lett. B 713 (2012) 68
- [57] *Muon HLT*, <https://twiki.cern.ch/twiki/bin/viewauth/CMS/MuonHLT#2011>
- [58] The CMS Collaboration, *Measurement of CMS Luminosity*, CMS PAS EWK-10-004
- [59] The CMS Collaboration, *Combination of top pair production cross section measurements*, CMS-PAS-TOP-11-024.
- [60] K. Melnikov, F. Petriello, *Electroweak gauge boson production at hadron colliders through $O(\alpha_s^2)$* , arXiv:hep-ph/0609070
- [61] K. Melnikov, F. Petriello, *The W boson production cross section at the LHC through $O(\alpha_s^2)$* , arXiv:hep-ph/0603182
- [62] The CMS Collaboration, *Measurement of the WW, WZ and ZZ cross sections at CMS*, CMS-PAS-EWK-11-010
- [63] *Standard Model Cross Sections for CMS at 7 TeV*, <https://twiki.cern.ch/twiki/bin/viewauth/CMS/StandardModelCrossSections>
- [64] *Official Prescription for calculating uncertainties on Missing Transverse Energy (MET)*, <https://twiki.cern.ch/twiki/bin/viewauth/CMS/MissingETUncertaintyPrescription>
- [65] The ATLAS Collaboration, The CMS Collaboration, The LHC Higgs Combination Group, *Procedure for the LHC Higgs boson search combination in Summer 2011*, CMS NOTE-2011/005
- [66] The CMS Collaboration, *Performance of tau reconstruction algorithms in 2010 data collected with CMS*, TAU-11-001
- [67] M. Bachtis et al “*Performance of tau reconstruction algorithms with 2010 data in CMS*”, CMS AN-2011/045
- [68] The CMS Collaboration, *Study of W and Z Boson Production at 7 TeV*, CMS-PAS-EWK-10-005
- [69] GEM Collaboration, *A GEM Detector System for an Upgrade of the CMS Muon Endcaps - Technical Proposal*, CMS IN 2012/002
- [70] T. Früboes, *The RPC based trigger for the CMS experiment - emulation of an algorithm and patterns optimalization*, http://hep.fuw.edu.pl/cms/docs/theses/MSc_fru.pdf.

-
- [71] K. Banzuzi et al *Link System and Crate Layout of the RPC Pattern Comparator Trigger for the CMS detector*, CMS IN 2002/065
- [72] W. Zabolotny et al *Implementation of the data acquisition system for the Resistive Plate Chamber pattern comparator muon trigger in the CMS experiment*, 2007 Meas. Sci. Technol. 18 2456-2464
- [73] CMS Collaboration, The Muon Project, CMS Technical Design Report, CERN/LHCC 97-32; CMS-TDR-003
- [74] CMS Collaboration, Physics TDR Vol I. Detector Performance and Software, CERN/LHCC 2006-001.